Lagrangian Feature Extraction in Two-dimensional Unsteady Flows

– Concepts and Algorithms –

Inauguraldissertation

zur Erlangung des akademischen Grades
des Doktors der Naturwissenschaften (Dr. rer. nat.)

eingereicht am Fachbereich Mathematik und Informatik
der Freien Universität Berlin

vorgelegt von

Jens Kasten
Zuse-Institut Berlin (ZIB)

Berlin, 2012

Erstgutachterin: Dr. Ingrid Hotz, Zuse Institut Berlin
Zweitgutachter: Prof. Dr. Ronald Peikert, ETH Zürich
Drittgutachter: Prof. Dr. Bernd Noack, Institut P', Poitiers, France

Tag der Disputation: 15.06.2012

Abstract

This thesis is an interdisciplinary work in the field of scientific visualization as part of computer science and the field of fluid mechanics. It is focussed on the analysis of time-dependent, two-dimensional flow fields. In this setting, the search for relevant structures – often called features – is one of the main topics. In my thesis, I am concerned with the extraction of Lagrangian coherent structures (LCSs). While this concept is one of the most discussed in the literature, there exists no commonly accepted definition. For instance, some researchers associate LCSs with vortices and others with distinguished manifolds of particle divergence and convergence. Due to the vague notion of LCSs, their extraction is split into different domain-specific and algorithmic challenges: What quantities are useful for identifying these features? How can these structures be robustly extracted? How can they be tracked efficiently over time? What are appropriate measures that enable a spatiotemporal filtering of the extracted features? I contribute to the above-mentioned questions by investigating the finite-time Lyapunov exponent (FTLE) and the acceleration.

The FLTE measures the separation and convergence of particles. Structures visible in the FTLE field are a popular realization of LCSs. In this thesis, an alternative algorithm for computing the FTLE field is given based on the Jacobian of the flow field. In addition, a critical review of the FTLE approach shows problems regarding the applicability to complex flow configurations.

Using the acceleration, I begin with transferring the concept of critical points of velocity field topology to time-dependent flow fields. This concept does only reveal significant structures for stationary flow fields. I show that features defined as minima of the acceleration magnitude serve as time-dependent counterparts of these points. These minima are introduced in this thesis as Lagrangian equilibrium points (LEPs). Similar to the centers of standard velocity field topology, a subset of the LEPs represents vortices. Within the concept of LEPs, I present three major contributions. At first, I introduce a hierarchy that is based on a spatiotemporal importance measure. It consists of the lifetime of the features and will be later on combined with homological persistence. The second contribution is the robust extraction of the LEPs and their evolution. I present an approach to extract a vortex merge graph. An existing tracking approach is adapted to the underlying physics while staying compatible with homological persistence, which enables a noise resilient extraction. Last, I present an approach to robustly extract vortex regions and their evolution. Employing the same robust combinatorial tools as for the vortex merge graph, I show how vortex regions can also be based on the acceleration magnitude. I also investigate the resulting vortex merge graph and the associated vortex regions based on the acceleration magnitude and compare the acceleration to other vortex related quantities.

Zusammenfassung

Diese Dissertation stellt eine interdisziplinäre Arbeit in den Bereichen der wissenschaftlichen Visualisierung als Teil der Informatik und der Strömungsmechanik mit dem Fokus der Analyse von zeitabhängigen zweidimensionalen Strömungsfeldern dar. Dabei spielt die Extraktion relevanter Strukturen – *features* genannt – eine wichtige Rolle. In dieser Arbeit geht es vorrangig um die Extraktion von *Lagrangian coherent structures* (LCSs). Für diese Strukturen gibt es keine allgemein akzeptierte Definition, obwohl sie zu den meistdiskutierten in der Fachliteratur gehören. Sie werden teilweise mit Wirbeln aber auch mit Partikeldivergenz assoziiert. Aufgrund der vagen Vorstellung von LCSs sind bei der Extraktion sowohl anwendungsspezifische als auch algorithmische Fragestellungen zu bearbeiten: Was sind vernünftige Größen zur Identifizierung dieser Strukturen? Wie kann man diese robust extrahieren? Wie kann man sie effizient über die Zeit verfolgen? Was sind geeignete Maße, die eine Hierarchie der extrahierten Strukturen bilden? Ich trage zur Beantwortung dieser Fragen bei, indem ich den *finite-time Lyapunov exponent* (FTLE) und die Beschleunigung eines Strömungsfeldes analysiere.

FTLE misst die Separation und Konvergenz von Partikeln. Strukturen, die im FTLE-Feld sichtbar werden, sind eine vielgenutzte Realisierung von LCSs. In dieser Arbeit wird eine alternative Berechnungsmethode für FTLE vorgestellt, die auf der Jacobi-Matrix basiert. Im Anschluss wird FTLE im Hinblick auf komplexe Strömungsdaten kritisch hinterfragt.

Unter Nutzung der Beschleunigung, übertrage ich das Konzept kritischer Punkte der Strömungsfeldtopologie auf zeitabhängige Felder. Dieses zeigt nur für stationäre Felder signifikante Strukturen. Ich zeige, dass Minima der Beschleunigungsmagnitude als zeitabhängige Gegenstücke dieser Punkte dienen. Sie werden in dieser Arbeit als *Lagrangian equilibrium points* (LEPs) eingeführt. Ähnlich wie die Rotationszentren in der Strömungstopologie, entspricht eine Untermenge der LEPs Wirbelzentren. Innerhalb dieses Konzepts enthält diese Arbeit drei Hauptresultate. Als Erstes stelle ich eine Hierarchie der LEPs vor, welche aus der Lebensdauer der Strukturen besteht und später um ein räumliches Wichtigkeitsmaß ergänzt wird. Der zweite Beitrag ist die robuste Extraktion der LEPs und ihrer zeitlichen Entwicklung. Ich präsentiere einen Ansatz um einen *vortex merge graph* zu extrahieren. Dabei wird ein bereits bestehender Ansatz auf die zugrundeliegende Physik angepasst, wobei die Methode weiterhin kompatibel zu homologischer Persistenz bleibt. Dies ermöglicht eine Extraktion trotz topologischem Rauschen. Als letzten Beitrag zeige ich, wie man Wirbelregionen basierend auf der Beschleunigung extrahieren kann. Ihre zeitliche Verfolgung wird ebenfalls ermöglicht. Dabei werden dieselben robusten Werkzeuge benutzt, die auch bei der Extraktion der LEPs Anwendung finden. Abschliessend werden sowohl der resultierende *vortex merge graph* als auch die Wirbelregionen analysiert. Beschleunigung wird dabei auch mit anderen Größen verglichen, die Wirbelaktivität markieren.

Acknowledgements

First of all, I want to thank my two advisors at the Zuse Institute Berlin, Ingrid Hotz and Hans-Christian Hege. While many PhD students are glad if they have one advisor who has time for their research once a week, I was lucky to have two supporting persons. They gave me the opportunity to work on such a great research topic and discussed problems with me at any time. Christian, you brought many great researchers to the institute. Thanks for letting me work at the ZIB. Ingrid, I hope you will be such an encouraging advisor to other students as you were it for me. Thank you so much.

In the field of visual data analysis, it is always helpful to have an expert in the field of the application who can contribute his expertise. With Bernd Noack, I had one of the best. You contributed not only ideas, but your delight when seeing new results encouraged me to do research.

Ronald Peikert reviewed this thesis and I am grateful for his comments. Thank you for the fruitful discussions.

Jan Reininghaus and David Günther helped a lot with the algorithms and ideas contained in this work. You are not just colleagues, but you are real friends. I hope that we will realize a lot of ideas together in the future.

I want to thank all people at the ZIB, especially, Alexander, Andrea, Andre, Britta, Christoph, Conny, Dagmar, Daniel, Hans, Heiko, Kai, Marco, Martin, Morgan, Norbert, Olaf, Stefan, Steffen, Uli, Vincent, and Valentin for being friends and colleagues. I think such a great group of researchers is hard to find anywhere else. I will miss all of you.

Of course, there are many people who helped me a lot by just being friends. Andre, Andreas, Antje, Christian, Doris, Fabian, Hilke, Jan M., Jan P., Johanna, Johannes, Jörn, Julia, Maja, Marion, Martin B., Martin E., Martin P., Matthias, Nicole, Sonja, Steffi S., Steffi W., Stephan O., Stephan W., Thomas, and many more. Thanks to all of you.

My family, Joachim and Maria Kasten, Sven Kasten and Sarah Schulz, encouraged me a lot. Thank you for your support – not only during the time of my PhD work, but at any time.

Finally, I want to thank my partner Dustin Lange. With only a smile, you can turn a bad day into a good one. You made the last four years the best years in my life – every single day. I love you.

– Jens Kasten –

Contents

Chapter 1

Introduction

Visual data analysis provides tools that support researchers in understanding complex data with the goal of solving questions in various scientific areas. The topic of this thesis belongs to the field of data analysis in fluid mechanics. There, the scientific interests involve a wide range of questions, such as analysis, optimization, and control of flows. Fluid flow researchers try to solve these problems by designing appropriate experiments or simulating different flow configurations (CFD). Due to sophisticated experiments, recording, and increasing computational power, the complexity of the resulting data sets is growing. Here, tools are needed that make the large amount of data manageable by focussing on the aspects of the flow the researchers are interested in. This includes conceptual and algorithmic challenges, which are investigated by researchers in data visualization as part of computer science in cooperation with the domain experts of fluid mechanics.

One possibility is to provide appropriate direct visualizations to give insight to the intricate flow structures that occur in these data sets. Many visualization techniques for different kinds of flow fields have been proposed in the recent years, cf. Section 3.1. Examples of these flow visualization techniques are line integral convolution (LIC), stream line computation and visualization, or image based methods such as GPU-LIC. Unfortunately, the increasing complexity of the data sets complicates an analysis using only flow visualization.

Besides such a direct visualization, the reduction of the raw flow data to an essential set of inherent structures is a promising approach. Thereby, the researchers can focus on the aspects of the flow field they are interested in. The structures are characterized as well-defined geometric objects, i.e., a point, line, surface, or volume, which are also called *features*. They can be extracted in several ways, e.g., as extremal structures or as iso contours of a given scalar field. An appropriate visualization of the extracted structures improves the interpretation of the flow fields. For instance, Schlichting's book '*Boundary layer theory*' [Sch79] and the Journal of Fluid Mechanics contain many masterpieces of hand-crafted principle flow sketches that reveal the main flow characteris-

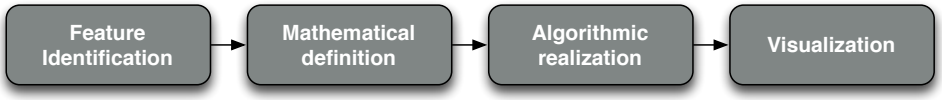

Figure 1.1 A feature-based analysis of flow fields consists of four steps: (i) identification the feature of interest, (ii) an appropriate and precise mathematical definition, (iii) an efficient and robust algorithmic realization, and (iv) a sensible visualization of the features in context of the flow field

tics in a single picture. Examples of interesting features are stagnation points, vortex cores, or vortex regions.

The extraction of features consists of four steps, see Figure 1.1. At first, the structures that are of interest have to be identified. This includes questions such as which structures reveal properties of the flow behavior the researchers want to investigate. Therefore, this step can only be done in cooperation with the domain experts. After the identification, a precise mathematical definition has to be found in the second step. Here, it has to be decided which quantity is used to extract the features. Sometimes, it is also necessary to investigate new measures derived from the flow field. In addition, it has to be chosen which of the inherent structures of the feature identifier field represent the feature, e.g., minimal points. In the third step, the analytical concept has to be realized as an algorithm. The complexity of the data sets often demand efficient and robust realizations, i.e., the algorithms are fast enough to analyze the data in short time and can handle inaccuracies in the data that naturally occur due to measurement or numerical problems. Often, an unsupervised automatic extraction of the features is another request to the algorithm. In the last step, an appropriate visualization has to be found. The extracted features have to be brought into a context with the flow configurations.

In this thesis, the focus lies on the feature-based analysis of time-dependent, two-dimensional flows. While many practical applications already involve three-dimensional fields, two-dimensional flows are still an active research area [Tab02, BM10, CKL10]. This especially includes important basic research questions. For these problems, the results of the two-dimensional case, which is often easier to understand and interpret, can be transferred to the higher-dimensional problems. An example is turbulence, for which the two-dimensional case is a basis for investigating the three-dimensional questions.

We base our feature extraction on the concept of Lagrangian coherent structures (LCSs). Over the past decades, this concept is one of the most discussed in the literature in the field of fluid mechanics – especially in basic research. Despite many efforts to characterize them, there is still no commonly accepted definition. Typically, two features are related to this concept: vortices and distinguished manifolds of particle divergence and convergence. Due to the vague notion of LCSs, different domain-specific and algorithmic challenges are

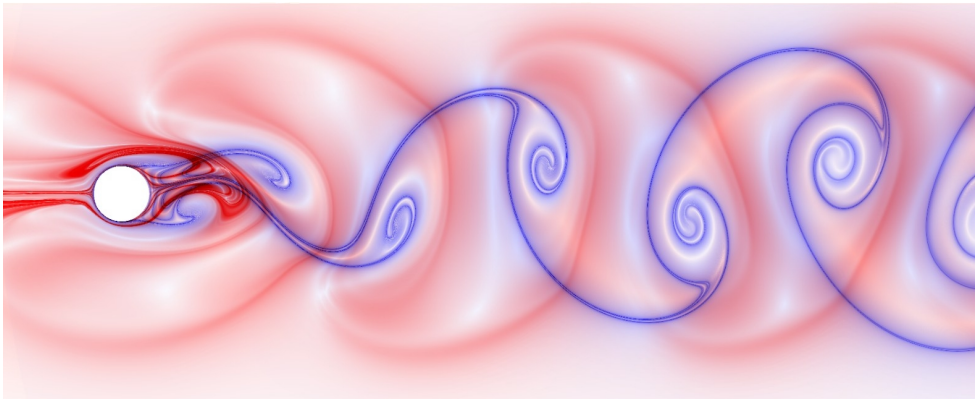

Figure 1.2 Simultaneous visualization of convergence (blue) and separation (red) of particles. The computation is done with the localized FTLE method that is introduced in Section 4.2.

investigated:

- **Which quantity is a good identifier for time-dependent features?** – For time-dependent flow fields, the flow behavior is determined by particles that live in the spatiotemporal domain. It is therefore important that the temporal dependence of the features is explicitly considered in the feature definition.

- **How can the features be extracted robustly?** – In the case of simulated and measured data, it is necessary to deal with inaccuracies in the data values. In the case of derivatives, which are the basis of many feature identifiers, this *noise* is even amplified. Therefore, robust methods are required to extract structures from these fields.

- **How can the features be tracked efficiently?** – Another interesting aspect in time-dependent data sets is the evolution of the features. An appropriate tracking algorithm has to be found. As for the feature extraction, the tracking method has to deal with noisy data sets, too.

- **What are appropriate measures enabling a spatiotemporal filtering of the features?** – Large and complex data sets typically contain a vast amount of structures. A hierarchy enables a distillation of important features. Thereby, it has to be defined what *important* means.

The concepts and algorithms presented in this thesis contribute to these questions. The focus therefore lies on the first three steps of the pipeline shown in Figure 1.1. New tools for an appropriate visualization of the extracted features are subsidiary elements of this thesis.

We investigate LCSs using the finite-time Lyapunov exponent (FTLE). The FTLE measures the convergence and separation of infinitesimally close particles over a given finite time period. Typically, ridges of the FTLE field are used to characterize the LCSs. We present the history of LCSs and their connection to FTLE. A critical review of the FTLE approach shows the problems regarding the applicability to complex flow configurations.

The standard algorithm [Hal01a] for the computation of the FTLE field is based on the flow map, which maps end points of path lines to their starting positions. The maximal separation of close particles is then measured by the spectral norm of the gradient of this field. This assumes that the flow map's dependence on the variation of start positions can roughly be approximated by a linear mapping. This assumption is only reasonable for small values of advection times and a very high sampling density. We introduce an alternative algorithm for computing the FTLE field. It is shown how the FTLE can be based on the Jacobian of the flow field, which measures the local separation. The method is therefore called localized FTLE. We compare the new method to the existing approach with respect to visual differences, robustness against noise, and efficiency. In addition to the new approach, a fast implementation is presented.

In an analysis of the FTLE, we will see that there are limitations using this approach to extract LCSs. Another structure that is often connected to LCSs are vortices. These play a fundamental role for the understanding and analysis of complex fluid flows. Researchers are interested in the location, size, and strength of vortices as well as their temporal development and interaction. This interest is driven by questions such as: What causes new vortices to arise or dissolve, to grow or shrink, to merge or split? In this thesis, different tools are developed to extract and analyze vortices and their region of influence.

While many approaches to extract vortices start with a physical consideration of the flow, we approach this topic from the perspective of vector field topology. There, vortex cores can be defined as centers in the velocity field. This approach is successful for steady fields. Unfortunately, the concept of fixed points does not reveal significant structures in time-dependent flow fields and we therefore introduce a time-dependent counterpart. It is based on carefully selected requirements such as choosing a Lagrangian viewpoint or a Galilean invariant feature identifier. We show that the acceleration magnitude fulfills these requirements. The features are defined as minima of the acceleration magnitude field and are called Lagrangian equilibrium points (LEPs). Similar to the centers in the steady velocity field, a subset of the LEPs represents vortices – the remaining LEPs represent saddles. They can be distinguished using the Jacobian of the flow field.

Our new concept of critical points is then extended by the following contributions

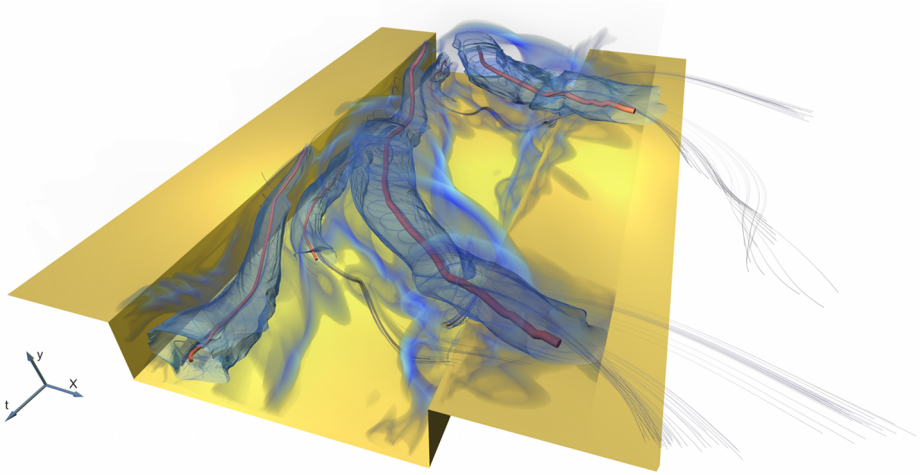

Figure 1.3 Using the acceleration magnitude, the methods that are introduced in Chapter 5 are able to extract the vortex core lines and their regions of influence. The image shows the extraction exemplary for a data set of a cavity.

- **Concept for long-living LEPs** – We emphasize the Lagrangian viewpoint by averaging the acceleration magnitude along path lines. The length of the integration is determined by the time the particle fulfills a minimality condition in the acceleration magnitude field. This introduces the concept of lifetime of features. The minima of the resulting field are weighted by this lifetime measure, which leads to the distillation of long-living features.

- **Extraction of a vortex merge graph** – In the next step, the analytical concept is realized using an extraction method that is resilient against noise. While the features are linked to path lines for the analytical concept, this restriction is dropped and the LEPs are extracted directly. Using analytical examples, it is shown that a subset of the LEPs represents vortex cores. Robust combinatorial tools are employed that are compatible with homological persistence simplification to extract the minima. This enables the analysis of complex data sets containing noise. The evolution of the structures is given by a combinatorial tracking approach, which we adapt to the underlying physics. Applying this algorithm, a 'vortex merge graph' results. The lifetime criterion is enhanced by a spatial importance measure, i.e., homological persistence. Thus, our algorithms can handle feature-rich flow fields by filtering out spatiotemporally important structures.

- **Extraction of associated vortex regions** – Investigating the topology of the acceleration magnitude, we observe that the minima depicting

vortex cores are surrounded by a particularly pronounced ridge. While the location of the vortex cores in a data set is defined by a subset of the LEPs, their regions of influence is therefore defined as the associated basin. We present an efficient algorithm to extract and track these basins. This is based on the same combinatorial tools for scalar field topology as the extraction of the vortex core lines. We therefore present a unified extraction framework for vortex cores and regions using the acceleration. A result of this framework for the data set of a cavity is shown in Figure 1.3.

Finally, the vortex merge graph and the associated vortex regions based on the acceleration magnitude are investigated. Different other flow quantities are statistically analyzed along the graph and the regions. This validates the extracted structures and reveals interesting results such as the dependence of the exact temporal positions of merge events on the type of feature identifier.

The remainder of this thesis is structured as follows. The mathematical, algorithmic, and physical foundation is given in Chapter 2. We begin with the notation and a brief explanation of the mathematical concepts that are needed to understand our approaches. Afterwards, basic algorithms for combinatorial topology extraction are explained, since the extraction of the LEPs, the tracking of the vortex cores, and the extraction of the vortex regions are based on scalar field topology. Then, basic physical concepts are explained that help to interpret the physical meaning of FTLE and acceleration. In Chapter 3, an overview of the related work of this thesis is given. We present approaches to visualize flow fields, to extract features in these, and to compute trajectories of critical points. The contributions of this thesis are then presented in Chapter 4 and Chapter 5. We begin with the FTLE and present the ideas mentioned above. Next, the concept of LEPs is introduced and the algorithms for the extraction of the vortex core lines and vortex regions are presented. This thesis is concluded with Chapter 6, where we discuss known limitations of the presented approaches. Potential remedies and future work are presented.

The work presented in this thesis has been previously published in peer-reviewed international conference proceedings, journals, and books [KPH+09, KHNH11, KWP+10, KPH+10, HKH11, KRHH11, KHH11, KHNH12].

Chapter 2

Foundation

In this chapter, the mathematical, algorithmic, and physical foundation is given that is needed in Chapter 4 and 5. In Section 2.1, the notation and definitions for scalar, vector and tensor fields are introduced. In addition, the associated topology is explained. In this thesis, extensive use of scalar field topology and critical points tracking is made. The basic algorithms are given in Section 2.2. To understand the physical meaning of the feature definitions that are discussed, elementary terms of fluid mechanics are presented in Section 2.3.

2.1 Basic mathematical definitions and notations

In this section, the mathematical notation used in this thesis is briefly introduced. We assume that the reader is familiar with vector calculus [MT03] and therefore recall only the basic terms.

In this thesis, we will refer to scalars and scalar-valued functions with non-bold symbols, e.g., x and $s(\mathbf{x})$, and to vectors and vector-valued functions with bold symbols, e.g., $\mathbf{x}$ and $\mathbf{v}(\mathbf{x})$. A tensor is always written as an upper-case symbol, e.g., $\mathbf{T}(\mathbf{x})$. The spatial coordinates in two or three dimensions are given by $\mathbf{x} = (x, y) = (x_1, x_2)$ or $\mathbf{x} = (x, y, z) = (x_1, x_2, x_3)$, respectively. The temporal parameter is referred to as t.

2.1.1 Scalar fields

A map that assigns a scalar value to each point in a space is called a *scalar field*. The values can be real- or complex-valued. In the following, a scalar field $s(\mathbf{x})$ given on a d-dimensional domain $D \subseteq \mathbb{R}^d$, is a real-valued function $s : D \to \mathbb{R}$. Temporally changing fields $s(\mathbf{x}, t)$ are given by $s : D \times I \to \mathbb{R}$, $I \subseteq \mathbb{R}$. In this thesis, we will mainly deal with two-dimensional scalar fields ($d = 2$) and the temporal interval will be finite.

For a smooth scalar field s, the first order spatial derivative is the *gradient*. It denotes the direction and amount of the steepest ascent in the field. It is given

by $\nabla s = (\frac{\partial s}{\partial x_1}, \cdots, \frac{\partial s}{\partial x_d})$, where $\frac{\partial}{\partial x_i}$ denotes the partial derivative by the i-th component. We sometimes refer to the partial derivatives by an abbreviated form, e.g., for a two-dimensional field, the gradient is denoted by $\nabla s = (s_x, s_y)$. The *Hessian* $\mathbf{H}_s = \left(\frac{\partial^2 s}{\partial x_i \partial x_j}\right)_{i,j}$ is the second order spatial derivate.

2.1.2 Vector fields

On a given d-dimensional domain $D \subseteq \mathbb{R}^d$, a map that assigns each point in a space a vector is called a *vector field* $\mathbf{v} : D \to \mathbb{R}^d$. For a d-dimensional image space, $\mathbf{v}$ consists of d scalar functions that determine the value of each component $\mathbf{v} = (v_1, \cdots, v_d)$. For fields with two- or three-dimensional image spaces, the components are typically referred to as $\mathbf{v} = (u, v)$ or $\mathbf{v} = (u, v, w)$, respectively. Similar to the definition of scalar fields, temporally changing vector fields $\mathbf{v}(\mathbf{x}, t)$ are given by $\mathbf{v} : D \times I \to \mathbb{R}^d$, $I \subseteq \mathbb{R}$.

The first order derivate of a vector field $v : D \subseteq \mathbb{R}^d \to \mathbb{R}^d$ is the *Jacobian*. It consists of all first derivatives of the components of the vector function $\mathbf{J}_\mathbf{v} = \left(\frac{\partial v_i}{\partial x_j}\right)_{i,j}$. Sometimes, we write also $\nabla \mathbf{v} = \mathbf{J}_\mathbf{v}$ and call this the velocity gradient tensor. It can be decomposed into a symmetric part $\mathbf{S}_\mathbf{v} = \frac{1}{2}\left(\mathbf{J}_\mathbf{v} + \mathbf{J}_\mathbf{v}^T\right)$ and an anti-symmetric part $\mathbf{\Omega}_\mathbf{v} = \frac{1}{2}\left(\mathbf{J}_\mathbf{v} - \mathbf{J}_\mathbf{v}^T\right)$.

The *divergence* of a vector field is given by $\mathrm{div}(\mathbf{v}) = \nabla \cdot \mathbf{v} = \mathrm{trace}(\mathbf{J}_\mathbf{v})$, where the *trace* of a matrix is the sum of its eigenvalues. For a three-dimensional vector field, its point-wise rotation or *curl* is defined by $\mathrm{curl}(\mathbf{v}) = \nabla \times \mathbf{v} = \left(\frac{\partial w}{\partial y} - \frac{\partial v}{\partial z}, \frac{\partial u}{\partial z} - \frac{\partial w}{\partial x}, \frac{\partial v}{\partial x} - \frac{\partial u}{\partial y}\right)$. The direction of the curl vector relates to the axis of the locally strongest rotation. The rotation plane is perpendicular to the vector. The amount of rotation is described by the magnitude of the vector. For two-dimensional fields, the curl reduces to a scalar function $\mathrm{curl}(\mathbf{v}) = \frac{\partial v}{\partial x} - \frac{\partial u}{\partial y}$. In the field of fluid dynamics, the curl is often referred to as *vorticity*.

Note that scalar fields give rise to *gradient fields*. For simply connected domains, these vector fields are curl-free, i.e., $\mathrm{curl}(\mathbf{v}) = 0$.

Feature curves. In time-dependent vector fields, there exist four types of *feature curves*: stream lines, path lines, streak lines and time lines. If the field does not change in time, the definitions of the first three types of lines yield the same curves – the stream lines. Note that the stream line is the only curve that lives in the spatial domain and can therefore be computed by using just one time step of the vector field.

Let $\mathbf{v}(\mathbf{x}, t)$ be a time-dependent vector field. For a fixed t_0, a *stream line* originating at $\mathbf{x}_0$ is defined as the solution of the ordinary differential equation (ODE)

$$\frac{d}{d\tau}\mathbf{x}(\tau) = \mathbf{v}(\mathbf{x}, t_0) \quad \text{with} \quad \mathbf{x}(0) = \mathbf{x}_0. \tag{2.1}$$

This stream line is a parameterized curve $\mathbf{C}(\tau)$ of the vector field. At each τ, the curve $\mathbf{C}$ is tangent to the vector at $(\mathbf{x}, t_0)$. The existence and uniqueness of the solution of this equation is guaranteed if the conditions of the theorem of Picard-Lindelöf [CL84] are fulfilled. Therefore, $\mathbf{v}$ has to be Lipschitz-continuous in $\mathbf{x}$. If the solution exists, the stream line itself is unique. Stream lines cannot intersect.

The next type of integral line is the *path line*. It is the solution of a similar equation

$$\frac{d}{d\tau}\mathbf{x} = \mathbf{v}(\mathbf{x}, t_0 + \tau) \quad \text{with} \quad \mathbf{x}(t_0) = \mathbf{x}_0. \tag{2.2}$$

Note that in contrast to the equation for a stream line, this equation is not autonomous – it depends on τ. However, path lines can be defined as tangent curves of a vector field which yields an autonomous differential equation. To do so, we extend the vector field by one dimension

$$\mathbf{v}'(\mathbf{x}, t) = \begin{pmatrix} \mathbf{v}(\mathbf{x}, t) \\ 1 \end{pmatrix}. \tag{2.3}$$

Now, path lines are the solution of

$$\frac{d}{d\tau}\mathbf{x} = \mathbf{v}'(\mathbf{x}, t) \quad \text{with} \quad \mathbf{x}(t_0) = \begin{pmatrix} \mathbf{x}_0 \\ t_0 \end{pmatrix}. \tag{2.4}$$

The curve that is the solution of this equation lives in a $d+1$-dimensional spatiotemporal domain. Interestingly, the stream lines of the vector field are also given by this equation, if we slightly change the definition of $\mathbf{v}'$:

$$\mathbf{v}'(\mathbf{x}, t) = \begin{pmatrix} \mathbf{v}(\mathbf{x}, t) \\ 0 \end{pmatrix}. \tag{2.5}$$

By interpreting the vector field as an advection field, both of these lines represent the evolution of a single infinitesimally small and massless particle. In contrast, streak and time lines show the evolution of multiple particles.

Streak lines consist of all points that originated from a common source location at different times. A single line is generated by choosing one point in a time-dependent flow field and continuously advect the line originating from this point by the vector field. Recently, Weinkauf et al. [WT10] have shown that streak lines can be alternatively computed as tangent curves of a derived vector field, which is defined as

$$q(\mathbf{x}, t, \tau) = \begin{pmatrix} (\nabla \phi_t^\tau(\mathbf{x}))^{-1} \cdot \frac{\partial \phi_t^\tau(\mathbf{x})}{\partial t} + \mathbf{v}(\mathbf{x}, t), \\ 0 \\ -1 \end{pmatrix} \tag{2.6}$$

where $\phi_t^\tau(\mathbf{x}) = \phi(\mathbf{x}, t, \tau)$ is the *flow map* $\phi : D \to D$. Its value is the location of the particle at $(\mathbf{x}, t)$ after advection time τ. The field $q(\mathbf{x}, t, \tau)$ is called the

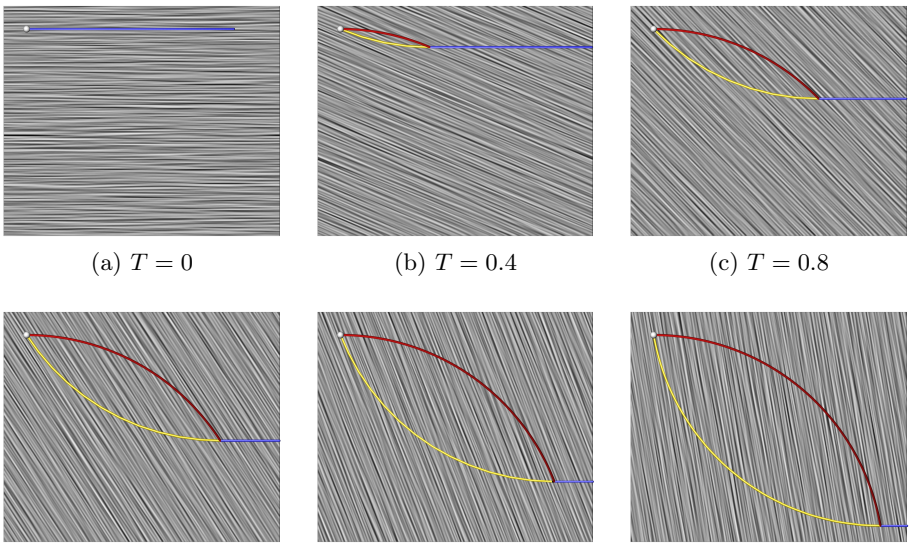

(a) $T = 0$ (b) $T = 0.4$ (c) $T = 0.8$

(d) $T = 1$ (e) $T = 1.2$ (f) $T = 1.4$

Figure 2.1 Different feature curves in a simple time-dependent two-dimensional vector field, cf. Equation (2.7). The stream lines are depicted by Line Integral Convolution (LIC). A path line is shown as a red, a streak line as yellow, and a time line as a blue curve. Note that the time line is cropped by the boundary of the data set ($[0, 1.2] \times [0, 1]$). While the time and streak line change over time, the part of the path line that is already computed holds its location.

streak line vector field. The parameter τ is the advection time of a point on the streak line. For details, we refer to [WT10].

The last type of lines are *time lines*. While a streak line describes a curve of advected points originating from a single source location, time lines are curves advected by the flow – there is not a common source point, but a line of connected points. They can be interpreted as the advancing front of multiple path lines. The best analog in the real world for these lines is a yarn thrown into a river.

To get a better insight into the behavior of these different curves, Figure 2.1 shows the evolution of these lines for a simple vector field

$$\mathbf{v}(\mathbf{x}, t) = \begin{pmatrix} \cos t \\ \sin t \end{pmatrix}. \tag{2.7}$$

None of the depicted curves coincides with another line. The start and end points of the streak and path line are the same, and the start point of the time line is always located at the end point of the path line.

Recently, a unified notion of tangent curves in time-dependent vector fields was proposed by Weinkauf et al. [WTH12].

2.1.3 Tensor fields

A *tensor* is a multi-linear map, i.e., a map that is linear in each argument. There exist tensors of different orders. For instance, tensors of order 0 are scalar values, and tensors of order 1 are vectors. Thus, similar to interpreting a scalar as a vector, scalar and vectors can be interpreted as tensors. However, in this thesis, if we speak of tensors, we mean tensors of order 2. For a given basis, a tensor can be written as an $n \times n$ matrix. Using this interpretation, tensors are also linear maps $\mathbf{T} : \mathbb{R}^n \rightarrow \mathbb{R}^n$. A *tensor field* $\mathbf{T}(\mathbf{x}, t)$ is then defined as a map that assigns each point in a space such a map $\mathbf{T} \in \mathbb{R}^{n \times n}$.

In this thesis, a tensor will occur as a derivative of a scalar or vector field. In fact, the Hessian, cf. Section 2.1.1, and the Jacobian, cf. Section 2.1.2, are tensors as defined above.

2.1.4 Two-dimensional scalar and vector field topology

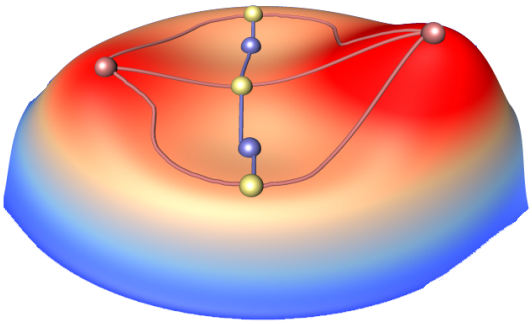

Figure 2.2 Topological features of a two-dimensional scalar function represented as a height field. The color is determined by the scalar value – blue corresponds to low values and red to high values. The topology consists of minima (blue), saddles (yellow), and maxima (red), and the minima lines (blue) and maxima lines (red) that separate the basins.

Vector field topology was introduced to the flow community by Tobak and Peake [TP82]. Helman and Hesselink [HH89, HH91] transferred the ideas to the visualization community a few years later. Afterwards, many extensions such as simplification and tracking algorithms have been published. We refer to the survey paper [LHZP07] and the references therein.

In this section, the first order topological features of scalar and vector fields are introduced. Since a scalar field can be interpreted as a gradient vector field, the topological features coincide. Their topology consists of critical points and separatrices. An example of the topology of a scalar function is shown in

Figure 2.2. For vector fields, attracting and repelling orbits are an additional part of the topology.

Critical points. Let $\mathbf{v}(\mathbf{x})$ be an arbitrary vector field on a domain D. A *critical point* $\mathbf{p}$ is a point in the domain for which the vector field is zero – $\mathbf{v}(\mathbf{p}) = \mathbf{0}$. In this thesis, we only consider first order critical points, i.e., at these points the Jacobian matrix has full rank. Other points are called *higher order critical points*.

To classify the critical points, one can use the *limit sets* of stream lines. Let $\mathbf{v}(\mathbf{x})$ be a non divergence-free ($\mathrm{div}(\mathbf{v}) \neq 0$), two-dimensional vector field and $C(\tau)$ be a stream line in this vector field. The *α-limit set* of the stream line C is defined by

$$\left\{ a \in D : \exists (t_n)_{n=0}^{\infty} \subset \mathbb{R}, t_n \to -\infty, \lim_{n\to\infty} C(t_n) \to a \right\}, \tag{2.8}$$

and its *ω-limit set*

$$\left\{ a \in D : \exists (t_n)_{n=0}^{\infty} \subset \mathbb{R}, t_n \to \infty, \lim_{n\to\infty} C(t_n) \to a \right\}. \tag{2.9}$$

If there exists an open neighborhood $U \subset D$ of a critical point $\mathbf{p}$, for which the α-limit sets of all stream lines in U only consist of $\mathbf{p}$, then $\mathbf{p}$ is called a *source*. Vice versa, if the ω-limit sets of all stream lines of U consist only of $\mathbf{p}$, then this point is called a *sink*. The sources and sinks of a vector field can furthermore be split up into classes of rotational behavior. If the stream lines in the neighborhood of $\mathbf{p}$ show rotational behavior, the sources and sinks are called *repelling and attracting foci*, respectively. If there is no such behavior, the sources and sinks are called *repelling and attracting nodes*. This classification does not cover all critical points. The remaining critical points are called *saddles*.

For divergence-free vector fields, only saddles and centers exist. The saddles are the points, where no rotational flow behavior is shown, and the centers are the critical points that are enclosed by rotational stream line behavior.

It can be shown that the above classification can be completely based on the eigenvalues of the Jacobian of the vector field. Let λ_1, λ_2 be these eigenvalues. Furthermore, let $Re(\lambda)$ be the real and $Im(\lambda)$ be the imaginary part of the eigenvalue λ. Then the first order critical points can be classified by

$$\begin{array}{lcccccc}
\text{Source (repelling)} & : & 0 & < & Re(\lambda_1) & \leq & Re(\lambda_2) \\
\text{Saddle} & : & Re(\lambda_1) & < & 0 & < & Re(\lambda_2) \\
\text{Sink (attracting)} & : & Re(\lambda_1) & \leq & Re(\lambda_2) & < & 0 \\
\text{Center } (Im \neq 0) & : & Re(\lambda_1) & = & Re(\lambda_2) & = & 0.
\end{array} \tag{2.10}$$

For the sources and sinks, the foci and nodes are distinguished by:

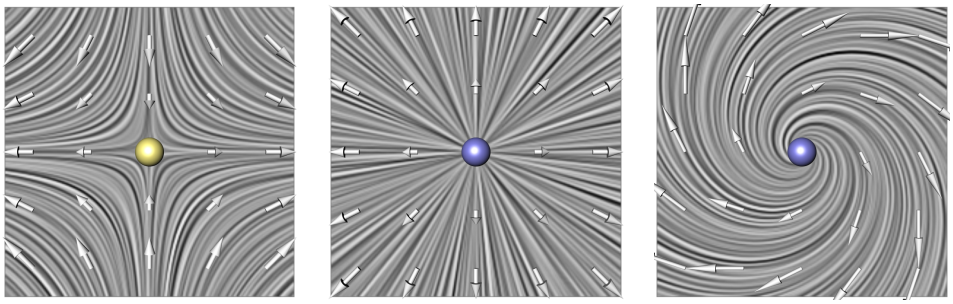

Saddle
$Re(\lambda_1) < 0 < Re(\lambda_2)$
$Im(\lambda_1) = Im(\lambda_2) = 0$

Repelling node
$0 < Re(\lambda_1) \leq Re(\lambda_2)$
$Im(\lambda_1) = Im(\lambda_2) = 0$

Repelling focus
$0 < Re(\lambda_1) \leq Re(\lambda_2)$
$Im(\lambda_1) = -Im(\lambda_2) \neq 0$

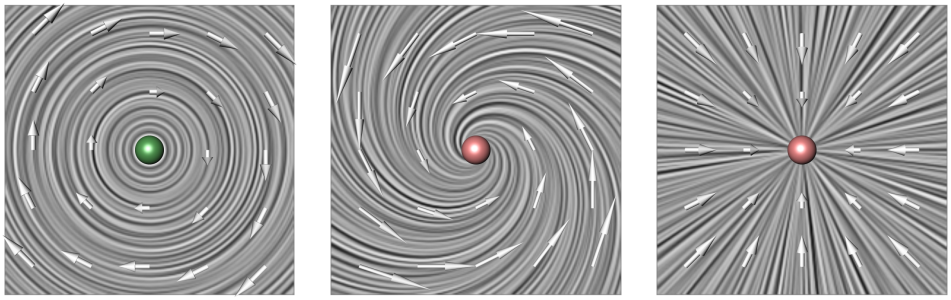

Center
$Re(\lambda_1) = Re(\lambda_2) = 0$
$Im(\lambda_1) = -Im(\lambda_2) \neq 0$

Attracting focus
$Re(\lambda_1) \leq Re(\lambda_2) < 0$
$Im(\lambda_1) = -Im(\lambda_2) \neq 0$

Attracting node
$Re(\lambda_1) \leq Re(\lambda_2) < 0$
$Im(\lambda_1) = Im(\lambda_2) = 0$

Figure 2.3 Different types of critical points of a vector field. The classification is done by the eigenvalues λ_1, λ_2 of the Jacobian of the vector field.

$$\begin{array}{lccccc} \text{Foci}: & Im(\lambda_1) & = & -Im(\lambda_2) & \neq & 0 \\ \text{Nodes}: & Im(\lambda_1) & = & Im(\lambda_2) & = & 0. \end{array} \tag{2.11}$$

If the eigenvalues of the Jacobian have an imaginary part, the stream lines in a neighborhood of the critical point show rotational behavior. An overview of the different types of critical points in a vector field and their classification is given in Figure 2.3. A simple vector field and its critical points are shown in Figure 2.4.

Since a scalar field can be interpreted as a gradient field, the definition of the critical points can be transferred. Note that a gradient field has no rotation and the imaginary part of the eigenvalues of the Jacobian is therefore zero. Thus, the critical points of a scalar field are sources, saddles, and sinks. They are typically called minima, saddles, and maxima, respectively. In Figure 2.2, all types of these critical points are shown.

Boundary switch points. For bounded domains, there is another type of distinguished points. Let $I \subset \partial D$ ($O \subset \partial D$) be the part of the boundary

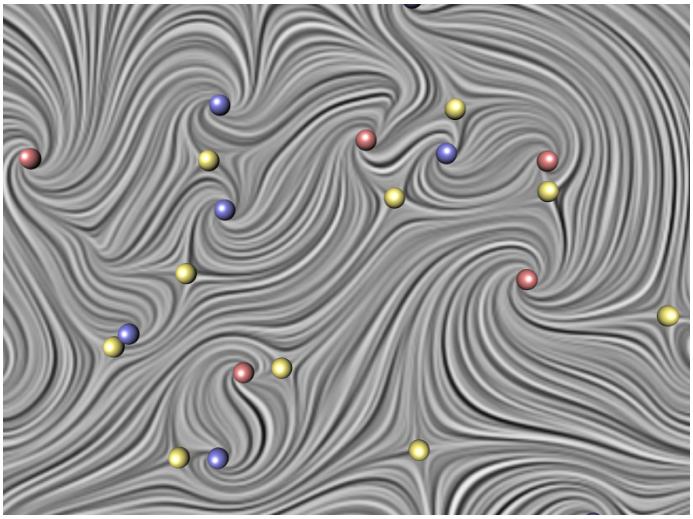

Figure 2.4 Critical points of a simple vector field. The vector field is depicted by LIC. The color of the critical points is determined by their classification as depicted in Figure 2.3.

of D, where the vector field points into (out of) the domain. The points on the boundary of the domain, where the inflow ($\mathbf{p} \in I$) changes to an outflow ($\mathbf{p} \in O$) are called *boundary switch points*. For details, we refer to Scheuermann [Sch99] or Weinkauf [Wei08].

Periodic Orbits. In an arbitrary vector field, there can be closed stream lines of attracting or repelling behavior. These are called attracting and repelling *periodic orbits*. They can also be characterized as α- and ω-limit sets. Note that in the case of orbits, the limit sets do not only contain a single point, but an entire line. They can only occur in vector fields and not in scalar fields. A periodic orbit is called *isolated periodic orbit* if it has an open neighborhood that does not contain any other periodic orbit. An example of this type of structures is shown in Figure 2.5.

Events in time-dependent vector fields. Let $\mathbf{v}(\mathbf{x}, t)$ be a time-dependent two-dimensional vector field. While the vector field smoothly changes in time, the location of the critical points also changes. There are four types of events that can occur: an entry or exit event, a Hopf bifurcation, and a fold bifurcation. A good description is given in the thesis of Tricoche [Tri02].

If a critical point enters or leaves the domain, this event is called *entry* or *exit*. If a critical point changes its type from a sink to a source, or vice versa, this event is called a *Hopf bifurcation*. For one moment in time, the type of the critical point will be a center. In that case, the eigenvalues of the Jacobian are purely imaginary. The last event is the *fold bifurcation*, which occurs

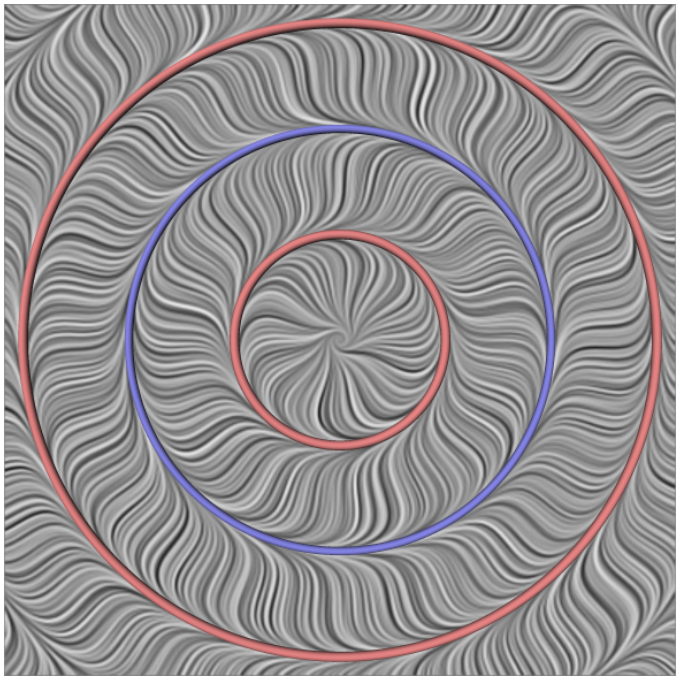

Figure 2.5 Isolated periodic orbits of a vector field. Attracting periodic orbits are shown in red, and repelling ones in blue. The stream line behavior is depicted by LIC.

when critical points are born or die. A birth or death event always produces or destroys not only one, but two critical points. In two-dimensional vector fields, for a sink or a source, always a saddle has to be created or destroyed.

Separatrices. In a two-dimensional, non divergence-free vector field, *separatrices* are stream lines that separate the field into regions of common stream line behavior, i.e., stream lines in one region share their source and destination. These destinations can be sources and sinks, inflow or outflow components of the boundary or periodic orbits.

Separatrices can be defined in the following way: First, we consider all limit sets of stream lines in the vector field. The α-limit sets consist of the set of all sources C_I, the set of all connected components of the inflow domain of the boundary $\{I_i : i = 1, ..., n\}$, and the set of all repelling periodic orbits $\left\{P_i^I : i = 1, ..., k\right\}$. On the other hand, the ω-limit sets consist of the set of all sinks C_O, the set of all connected components of the outflow domain of the boundary $\{O_i : i = 1, ..., n\}$, and the set of all attracting periodic orbits $\left\{P_i^O : i = 1, ..., k\right\}$. Now, we define an α-*basin* of an element of the α-limit set a as the set of all points $\mathbf{p}$, for which a stream line starting at a point $\mathbf{p}$ has a as its α-limit set. The ω-basins are defined by analogy. Note that the joint set of all α-basins covers the whole domain and the basins do not overlap

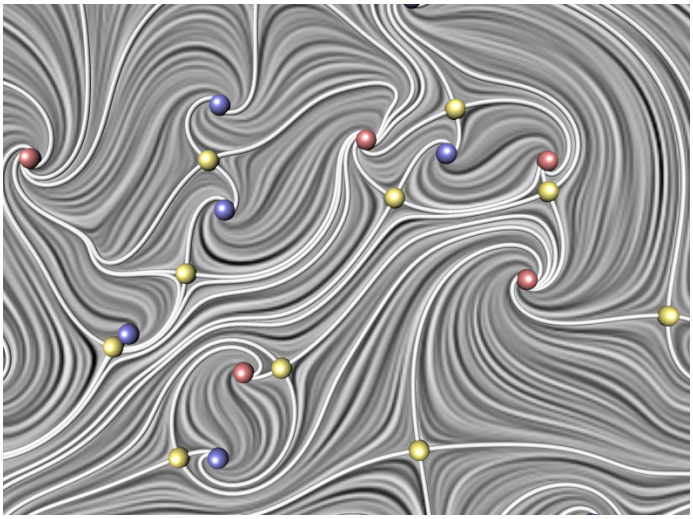

Figure 2.6 Separatrices of the vector field shown in Figure 2.4.

each other. This is also true for the ω-basins. Now, let $\{M_i \subset D : i = 1, ..., l\}$ be a set of subsets of the domain D in the way that all points $\mathbf{p} \in M_i$ share the same inflow and outflow basin. The boundary of each M_i excluding the associated α- and ω-limit set defines the separatrices. For details, we refer to Scheuermann et al. [SHJK00].

While the above definition is based on α- and ω-limit sets, the separatrices can also be defined using the saddles and the boundary switch points. A streamline is computed in forward and backward direction of the eigenvectors of the Jacobian at these points. For a two-dimensional vector field, at each saddle point, there are four such separatrices. Two are connected to sinks and the other two are connected to sources. This definition also holds for divergence-free vector fields, but here the separatrices connect the saddles. The separatrices of the vector field of Figure 2.4 are shown in Figure 2.6.

By interpreting a scalar field as a gradient vector field, one can define separatrices in the same way as for arbitrary vector fields. Fo scalar field topology, the separatrices that are connected from a saddle to a minimum (maximum) are called minimum (maximum) lines. These lines are also shown in the example in Figure 2.2.

Note that for the definition of extremal structures in scalar fields, the notion of *ridges* and *valleys* comes into play [Ebe96]. They are defined based on the Hessian of the scalar field. These structures are not always the same curves as the separatrices. There are scalar fields for which not all ridges or valleys are separatrices and vice versa. In this thesis, we will only use separatrices – even if we speak of ridges or valleys.

2.2 Algorithmic background

In this section, basic algorithms are presented to extract the topology of a scalar field and track the critical points over time.

2.2.1 Combinatorial methods to extract scalar field topology

Morse theory [Mil63] relates the topology of the domain to the extremal structure of a given scalar function on this domain. On the other hand, tools developed from Morse theory can be used to compute the extremal structure of a scalar function. We will use algorithms that are based on the discrete notion of Morse theory that was introduced by Forman [For01] for cell complexes. He defined a discrete version of a vector field, which is called *combinatorial vector field* [For98a]. Based on this work, extraction algorithms for the topological skeleton of a discrete vector field were proposed.

Lewiner [Lew05] presented the first implementation of Formans theory. With a focus on the extraction of the extremal structures of scalar fields, he used a computational realization of the combinatorial vector field using hyper graphs and hyper forests. Guylassy et al. [GNP$^+$06, GNPH07, GBHP08, Gyu08, GBPH11] proposed several efficient algorithms for the extraction of critical points of scalar fields – mainly in three dimensions. They do not compute the combinatorial vector field directly, but the *Morse-Smale complex* [Sma61], which represents the extremal skeleton of a given scalar function. King et al. [KKM05] presented an algorithm to compute the Morse-Smale complex from a given point data set.

Mostly, the implementation of combinatorial vector fields comes with a simplification strategy. The number of critical points can be thereby reduced until the minimum amount of critical points for a given domains is reached. For a sensible reduction of the critical points – often called *cancellation* –, the concept of homological persistence as introduced by Edelsbrunner [EHZ01, EH08] is used. We will describe this concept in the last part of this section.

In this thesis, we will make use of a recent algorithmic approach done by Reininghaus et al. [Rei12, RGH$^+$10]. Note that we will follow the notation and definitions of his thesis in the remainder of this section. While the methods are able to extract scalar and vector field topology, we only need the extremal structure of a scalar field. Therefore, we only describe the algorithms based on the combinatorial gradient field, which is a special case of a combinatorial vector field. The difference is that a gradient field cannot contain periodic orbits. We will introduce the basic concepts, but for details, we refer to the mentioned publications. Note that we speak of gradient fields in the remainder of this section, but the actual field is typically a scalar field.

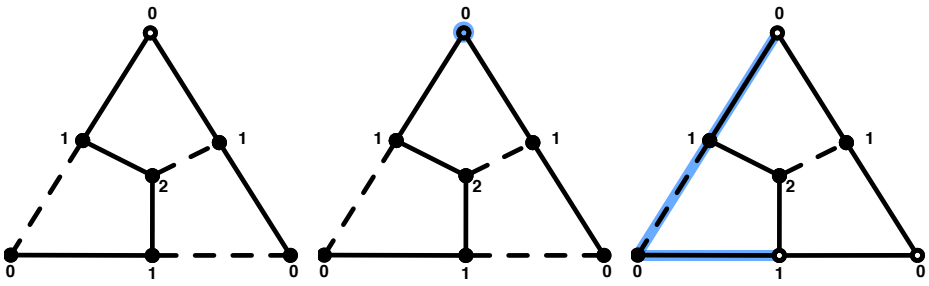

(a) Matching (b) Critical Point (Minimum) (c) Separatrix

Figure 2.7 A combinatorial gradient field is a matching on a given graph. The matched edges in the images are indicated by the dashed lines (a). A critical point is an unmatched node (b). A separatrix is an alternating path in the graph that connects two critical points (c).

Combinatorial gradient fields. Using the approach of [Rei12], the combinatorial representation of a gradient field consists of two components: the representation of the domain as a graph and the representation of the gradient vector field as a matching on this graph. For the sake of simplicity, the definition in this section will be done assuming that the grid of the original data is a simplicial complex, e.g., a triangulation. The same structures can be defined for arbitrary complexes using polygons as basic structural elements, e.g., the data can be given on a rectilinear grid. Then, the grid is a cell complex and the combinatorial vector field is defined on a cell graph.

Let S be a two-dimensional simplicial complex and S_d be the simplices of dimension d. An associated *simplicial graph* $G_S = (N, E, \phi, \psi)$ consists of the associated nodes N and edges E and two functions that evaluate the dimension of a node (ϕ) or an edge (ψ). First, for every d-dimensional simplex $s \in S_d$, a node is inserted to the simplicial graph with the same dimension d. An edge (a, b) is inserted in the graph, if a is in the boundary of b in the simplicial complex S. The dimension of this edge is given by the dimension of a. The dimension is also called *layer*. To define a gradient field on this graph, each node has to be assigned a scalar value. For the nodes of layer zero, a scalar value is typically given by the original scalar field associated to the gradient field. For the other nodes, the maximum value of the lower layered nodes in their boundary is used. Figure 2.8 depicts a simplicial graph for a given triangulation.

A combinatorial vector or gradient field is now defined by a *matching* on this graph. In detail, a matching is a subset V of the edges E of the graph G_S in the way that each two elements of V are disjoint, see Figure 2.7. A *combinatorial stream line* in this discrete representation of the vector field is defined as an alternating path with respect to the matching. An abstract algorithm to trace the stream lines of layer p starting at a node u is given in

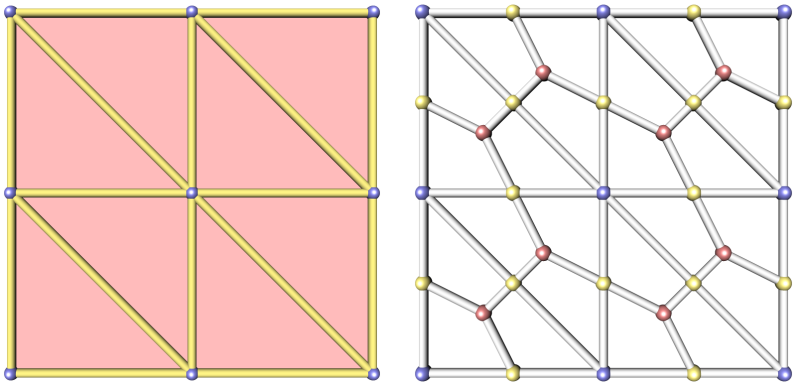

(a) Triangulation (b) Simplicial Graph

Figure 2.8 Construction of a simplicial graph based (right) on a triangulation (left). Each point, edge and face in the triangulation corresponds to a node in the graph. The layer of the node is determined by the dimension of the simplex. Here blue spheres represent nodes of layer 0, yellow spheres nodes of layer 1, and red spheres represent nodes of layer 2. The edges in the graph are determined by the connectivity in the triangulation.

Algorithm 2.1: Combinatorial Streamline Integrator: *traceLine(...)*

Input: $G_S = (N, E, \phi, \psi)$, $V \subset E$, $u \in N$, $p = 0, 1$
Output: Combinatorial p-streamline that starts in u

```
1: loop
2:    Line.append( u )
3:    if  there exists w: {u, w} = ℓ^p ∈ V  then
4:       u ← w
5:       V ← V^c
6:    else
7:       return
```

Algorithm 2.1. Thereby V^c denotes the complement of V in E.

The topological features defined in Section 2.1.4 can be easily transferred. A critical point in this vector field is a node of the graph that is not contained in any pair of the matching. The type of the point is defined by its layer. For two-dimensional fields, minima have layer 0, saddles have layer 1 and maxima have layer 2. A separatrix is defined as a combinatorial stream line connecting critical points. Again, the type of the separatrix is defined by the layer. An overview of the topological features is given in Figure 2.7.

Construction of the matching and cancellation. The matching needs to be determined in a way that the resulting combinatorial gradient field re-

sembles the original field best. Reininghaus et al. [Rei12, RGH+10] implemented an approximation algorithm for this problem. They begin with an empty matching. Then, a sequence of augmentation paths is computed. An augmentation means that the matched edges along the augmenting path become unmatched and vice versa. Choosing the correct set of augmentation paths results in a matching that resembles the scalar field best. To further reduce the topological complexity of the combinatorial gradient field, Reininghaus et al. [RGH+10] augment the matching beyond the exact extremal structure of the scalar function. As a notation, for a matching M and an augmenting path s, the augmented matching is denoted as $M \triangle s$.

The main problem in choosing the augmentation paths is to make sure that an augmentation of an existing valid matching, i.e., a Morse matching [For98b], results in another valid matching. Here, Forman's *cancellation theorem* [For98b] helps to fulfill this condition: If two unmatched nodes are connected by exactly one separatrix s in a Morse matching M, then $M \triangle s$ is also a Morse matching. Thus, it is sensible to choose the separatrices as the augmentation paths. Augmenting a matching along a separatrix removes a pair of critical points: a minimum and a saddle, or a maximum and a saddle. This is the reason why an augmentation is also called *cancellation*.

Algorithm 2.2: Generate Matching Sequence

Input: $G = (N, E, \phi, \psi), \omega$
Output: $AugPaths$, V_{k_n}

```
1:  M ← ∅, AugPaths ← ∅, heap ← ∅
2:  for all u ∈ N and p = 1 do
3:      (path, weight) ← getMaxUniqueSeparatrix(G, ω, M, u^1)
4:      heap.push(u, weight)
5:  while heap ≠ ∅ do
6:      (u, weight) ← heap.pop()
7:      (path, weight) ← getMinUniqueSeparatrix(G, ω, M, u)
8:      (nextNode, nextWeight) ← heap.top()
9:      if weight ≤ nextWeight then
10:         M ← M △ path
11:         if weight > 0 then
12:             AugPaths.push(path)
13:     else if weight < ∞ then
14:         heap.push(u, weight)
15: V_{k_n} ← M
```

The details of the construction of the matching sequence are given in Algorithm 2.2 [Rei12]. It makes use of the function $getMinUniqueSeparatrix(...)$, which iterates over all four separatrices of a given saddle and returns the augmenting path s with the lowest weight. The weight is defined as the value of

the higher-layered critical node minus the value of the lower layered critical node. The function also tests the uniqueness condition as mentioned above. Unique means that the minimum or maximum that is connected to the saddle can only be reached by this separatrix outgoing from the saddle. If no such separatrix exists, an empty augmenting path is returned by the function with the weight ∞. Note that as long as augmenting paths with negative weight exist, the matching that represents the correct extremal structure of the scalar function has not been reached yet. Augmenting paths with positive weight further reduce the topological complexity of the extremal structure. Therefore, first the negative paths have to be processed before the positive ones. The first matching for which no valid path with a negative weight exists is called *initial matching*.

Algorithm 2.2 is run in the following way. First, we begin with an empty matching, no augmenting paths and an empty min-heap (Line 1). Now, all saddles of the grid are added to the heap with the weight of their minimum unique separatrix (Lines 2 - 4). While the heap is not empty, the following is done: The saddle with the lowest weight in the heap is taken (Line 6). Then, the current weight returned by $getMinUniqueSeparatrix(...)$ is computed for this saddle (Line 7). Note that augmentations can change the weights of the saddles in the heap. According to Reininghaus [Rei12], it is sufficient to check if the next element in the heap has a higher weight (Lines 8 and 9). If this is true, the saddle is still valid and the associated separatrix can be used as an augmentation path (Line 10). If the weight of the augmentation path is positive, we already reduce the complexity of the extremal structure of the scalar field. We therefore want to save the augmenting path (Lines 11 and 12). If the augmenting path was not valid anymore, the saddle is reinserted to the heap, if it still has a valid separatrix (Lines 13 and 14). The resulting matching is saved at the end (Line 15).

Note that after the initial matching is constructed, a hierarchy of the extremal structure of the scalar function is given by the order of the augmenting paths. It was shown by Dey et al. [DLL$^+$10] that this hierarchy is similar to the hierarchy introduced to the critical points by homological persistence, which is described in the next section.

Alternatively, Reininghaus et al. employ an approach of Robins et al. [RWS11] to construct the initial matching. Here, the construction of the initial matching is parallelized. Thus, the computation can be done fast on current multi-core platforms. In addition, the resulting unmatched nodes of the initial matching are guaranteed to be critical. After constructing the initial matching, the above algorithm to construct the hierarchy is still employed.

Homological persistence. An importance measure for critical points is defined by *persistence*. Loosely speaking, it measures the resistance of a critical point against perturbation of the data values in its neighborhood. The measure

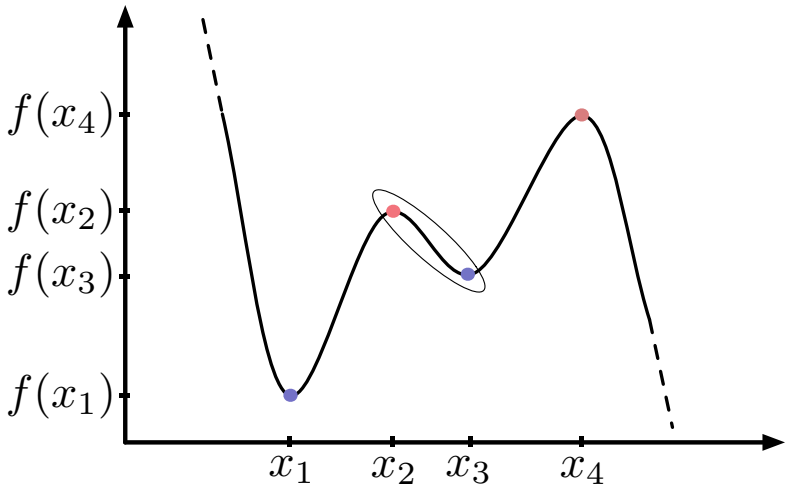

Figure 2.9 Pairing induced by homological persistence for a one-dimensional scalar function. At the maximum in the center, two components of the sub-level sets of the function merge. There, the maximum is paired with the minimum of the two components that has the highest value. The other two critical points will be paired afterwards, when the other maximum is reached.

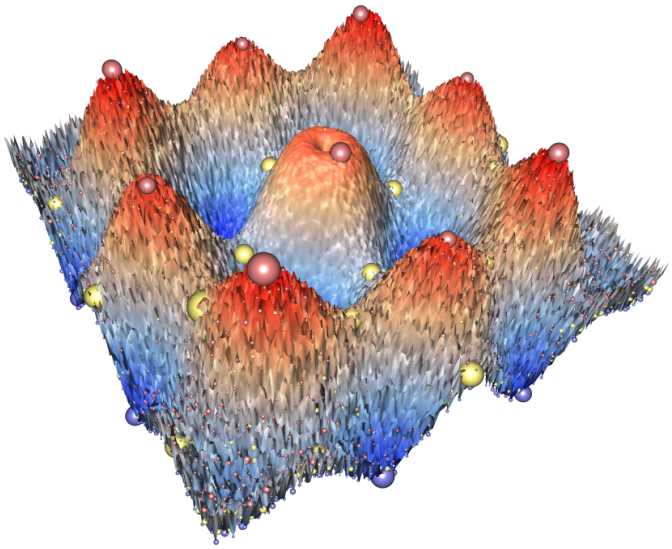

Figure 2.10 Critical points of a scalar function. To the function a small amount of noise is added that grows towards the boundary. The color is determined by the classification as in Figure 2.3. The size of the critical points is determined by the persistence value. The algorithm extracted 37957 critical points. Homological persistence classifies most of them as unimportant.

was proposed by Edelsbrunner et al. [EHZ01, EH08]. Its computation is related to the notion of sub-level sets and Betti numbers. We will briefly introduce these concepts – without giving a formal definition, since details would need an explanation of homology groups. For details, we refer to [EHZ01] for the persistence measure and to [Hat02] for an introduction to homology theory.

In two dimensions, the Betti numbers indicate the number of connected components (β_0) or the number of holes in a surface (β_1). For instance, a disk has $\beta_0 = 1$ and $\beta_1 = 0$. Another example is a two-dimensional surface that looks like the digit 8. It has $\beta_0 = 1$, but $\beta_1 = 2$.

For a given function $f : D \to \mathbb{R}$ and a given value t, the sub-level set $S_t \subseteq D$ is defined as

$$S_t(f) = f^{-1}\left((-\infty, t]\right) \tag{2.12}$$

It consists of all point of D for which the function value of f is smaller than t.

After introducing these two ideas, we can now define homological persistence of critical points. Let $f : \mathbb{R}^2 \to \mathbb{R}$ be a two-dimensional scalar function. Furthermore, let $\beta_0(f, t)$ and $\beta_1(f, t)$ be the two relevant Betti numbers of the sub-level set $S_t(f)$ for a given t. With increasing t, these Betti numbers change. Homological persistence measures these changes. There are four events in two-dimensional fields: First, a new connected component in the sub-level set can be born. This happens at a minimum. Furthermore, two connected components can merge, which occurs when the parameter t passes the value of a saddle. Third, a new hole can also be born at a saddle. Last, a hole in a connected component can die. This occurs at a maximum.

The persistence value of the critical points is thereby determined in the following way: A new-born connected component is labeled with the associated minimum. At a saddle, two connected components merge that are labeled with two different minima. The persistence value for the saddle and the minimum with the higher function value is defined as their height difference. The merged component is labeled with the remaining minimum. A maximum is paired with the saddle with the highest function value and, again, their persistence value is defined as their height difference. Note that this informal explanation of persistence does not hold in three dimensions.

In Figure 2.9, an example of a one-dimensional function and the pairing is given. While here only minima and maxima exist, persistence is defined in a similar way as for two-dimensional fields. The critical points in the center are paired first and the outer two afterwards. A two-dimensional example of the critical points of a scalar function weighted with persistence is shown in Figure 2.10.

The changing Betti numbers of the sub-level sets can be interpreted as time-dependent functions. Thus, by the pairing of the critical points, some kind of lifetime is induced. This explains the name persistence for the importance measure.

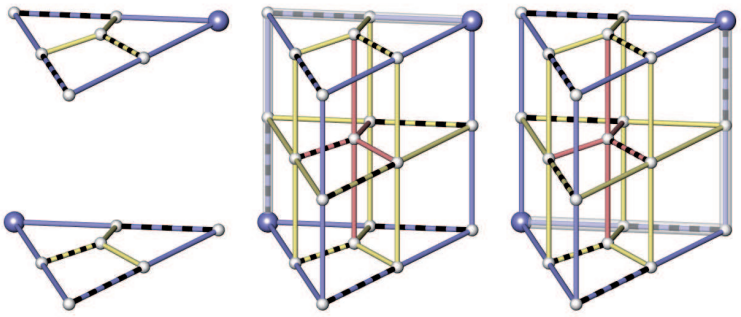

Figure 2.11 Combinatorial feature flow fields. Left: Two subsequent combinatorial gradient fields V_0 and V_1. Middle: Forward tracking field $V_{[0,1]}$. Right: Backward tracking field $V_{[1,0]}$. The minima (blue) in V_0 and in V_1 are tracked as there is a combinatorial 0-streamline (transparent) in $V_{[0,1]}$ and a combinatorial 0-streamline in $V_{[1,0]}$ that connect these points.

2.2.2 Combinatorial feature flow fields (CFFF)

Using combinatorial gradient fields, Reininghaus et al. [RKWH12] proposed a method to efficiently track the critical points in two-dimensional scalar fields. Their method is based on the mathematical foundation proposed by King et al. [KKM08]. In this thesis, we will use and adapt their approach to track minima in time-dependent scalar fields. The relevant algorithms are discussed in the following.

Tracking fields. The approach is based on two fields that represent the combinatorial flow of the critical points from one to the next time slice and vice versa. The method is called combinatorial feature flow fields (*CFFF*). The individual fields are called forward and backward tracking field. They are based on the combinatorial gradient fields of the scalar field. For the sake of simplicity, we assume that the simplicial graph $G_S = (N, E, \phi, \psi)$ of these gradient fields is the same for all slices of the gradient field, i.e., the grid the data is given on is the same for all time-slices and only the data values change over time.

Let $(V_t)_{t=0,1,2,\ldots,T}$ be the sequence of combinatorial gradient fields for which the critical points shall be tracked. We assume $T = 1$ for now. The forward and backward tracking field is now defined as a combinatorial gradient field of a complex $S \times [0, 1]$. The graph $G_{S\times[0,1]}$ can thereby be constructed from the simplicial graph G_S. Note that $S \times [0, 1]$ is a cell complex, but no simplicial complex. $G_{S\times[0,1]}$ is therefore a cell graph. To construct this cell graph, we start with three copies G_S^1, G_S^2, and G_S^3. Then, for each node of G_S^1 an edge to the corresponding node of G_S^2 is added. The same is done for G_S^2 and G_S^3. The layer of each node in G_S^2 is increased by one.

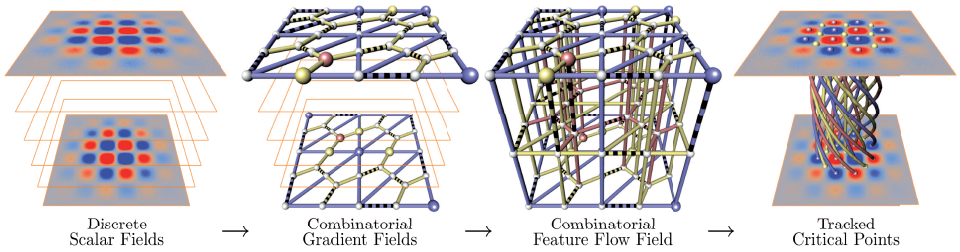

Figure 2.12 Pipeline of the combinatorial feature flow fields approach.

Now, the *forward tracking field* is defined by a matching on this graph. Thereby, the matching on G_S^1 and G_S^2 is determined by the matching of V_0, i.e., the matching of the earlier time slice. The matching on G_S^3 is defined by the matching on V_1. Furthermore, all links that connect a critical point of V_0 to a node in G_S^2 are added to the matching. This defines a combinatorial gradient field, as was shown in [KKM08].

Iteratively, the forward tracking field can be defined for the whole sequence $(V_t)_{t=0,1,2,\ldots,T}$. If the tracking field is given for $V_{[0,k]}$, then the field for $V_{[0,k+1]}$ is constructed as the union of $V_{[0,k]}$ and $V_{[k,k+1]}$. The *backward tracking field* is given by reversing the sequence $(V_T)_{k=0,1,2,\ldots,T}$. An example for a forward and backward tracking field is given in Figure 2.11.

Using the approach of King et al. [KKM08], two critical points of two adjacent time slices are connected to each other, if they are connected by streamlines in both the forward and backward tracking field. We will call these connections *unique tracking*. The lines connecting critical points are called *critical lines*. Note that the only critical points of the resulting forward tracking field exist in V_T and in V_0 for the backward tracking field. However, the critical points are extracted in the original combinatorial gradient fields. Just their evolution is computed in the combinatorial feature flow fields. Note that this evolution can also be computed on the combinatorial gradient fields that are simplified by homological persistence.

Efficient computation. Using the above mentioned definition, Reininghaus et al. [RKWH12] proposed an efficient implementation to track the critical points. First of all, an out-of-core algorithms is proposed. Only two combinatorial gradient fields are needed to track the critical points form one to another time slice. In addition, they show that it is not necessary to compute the actual combinatorial feature flow fields. The tracking of the minima can be done by tracing stream lines in the two-dimensional combinatorial gradient fields. The maxima can be extracted in a similar way by switching the combinatorial gradient fields and the direction of the stream line computation. The saddle tracking is given by appropriately intersection of the separatrices of the saddles in the adjacent time slices. Note that the tracking of saddles and maxima is

Algorithm 2.3: Main CFFF algorithm

Input: S, $(f_t)_{t=0,1,\dots,T}$, σ
Output: All critical lines in $V_{[0,T]}$
1: $G_S \leftarrow$ constructCellGraph(S)
2: **for** $t = 0$ to $T - 1$ **do**
3: $V_t \leftarrow \mathrm{CGF}(G_S, f_t, \sigma)$
4: $V_{t+1} \leftarrow \mathrm{CGF}(G_S, f_{t+1}, \sigma)$
5: lines $\leftarrow$ lines $\cup$ trackMin(G_S, V_t, V_{t+1})

Algorithm 2.4: Minimum tracking algorithm: *trackMin(...)*

Input: $G_S = (N, E, \phi, \psi)$, $V_t \subset E$, $V_{t+1} \subset E$
Output: All critical min lines in $V_{(t,t+1)}$
1: **for all** $u \notin N(V_t)$ and $p = 0$ **do**
2: Line $\leftarrow$ traceLine$(G_S, V_{t+1}, u, 0)$
3: $w \leftarrow$ Line.last()
4: Line $\leftarrow$ traceLine$(G_S, V_t, w, 0)$
5: **if** Line.last() $= u$ **then**
6: MinCritLines.append($\{u, w\}$)

not needed in this thesis. We refer to [RKWH12] for details and a reasoning of the simplification of the tracking.

The algorithmic approach for tracking the minima is given in the following. The main pipeline is shown in Figure 2.12. An abstract implementation is outlined in Algorithm 2.3 that computes the tracking of a time-varying function$(f_t)_{t=0,1,\dots,T}$ on a grid S. Note that with the parameter σ, the persistence threshold for the simplification of the combinatorial gradient fields is determined.

First, since the simplicial graph is the same for all time slices, this one is constructed (Line 1). From a stack of time slices of a scalar function, for two adjacent slices, the combinatorial gradient fields are now defined as the matching (Line 3 and 4). To the set of critical lines, the tracked minima lines are added (Line 5).

To track the minima lines, Algorithm 2.1 is used to compute the stream lines. Algorithm 2.4 shows the general approach. The input is a simplicial graph G_S and two matchings V_t andV_{t+1} that represent the adjacent combinatorial gradient fields. The tracking is computed in a loop that goes over all nodes u that are not in the matching V_t and have layer $p = 0$ (Line 1). These nodes are minima. Given a minimum u in V_t, a combinatorial stream line is started at this node in the combinatorial gradient field V_{t+1} that ends in a minimum w (Line 2 and 3). Then a new stream line is started form the node w in the combinatorial gradient field V_t (Line 4). If this stream line ends in u, the

minima u and w are connected (Line 5 and 6).

Integrated persistence. Reininghaus et al. [RKWH12] introduced an importance measure for the critical lines in addition to the efficient computation. Each critical point in each time slice has a persistence value as described in Section 2.2.1. The importance measure is then defined as the sum of the persistence values of the critical points that make up the line. The value is divided by T, i.e., the number of time steps. This is necessary, since different temporal resolutions for the same temporal interval would result in different importance measures otherwise. The measure is called *integrated persistence*.

2.3 Physical concepts

While arbitrary vector fields occur in many applications, we focus on vector fields that describe flow fields, i.e., they have a physical meaning: they capture the motion of a substance. The flow fields that we are interested in obey a physical law: the Navier-Stokes equations. We will derive these in Section 2.3.1. Afterwards, we introduce two physical concepts that are important for the understanding of the physical meaning of the feature identifier that will be used in Chapter 5.

2.3.1 Navier-Stokes equations

In this section, we will derive the basic equations that describe the motion of Newtonian fluids. We will deduce these in three dimensions. While the derivation might change, the equations are also valid in two dimensions. Furthermore, we will assume that all functions are that smooth that the derivatives exits and that integrals are finite. The derivation is based on the mathematical introduction to fluid dynamics by Chorin and Marsden [CM93]. All details are given in the first chapter of that book. In this section, just a brief excerpt is given.

Assume a fluid given in a domain $D \subseteq \mathbb{R}^3$. Let S be a surface in this domain and $\mathbf{v}(\mathbf{x}, t)$ be the vector field that describes the motion of this fluid. This motion is controlled by two forces: pressure and stress. The pressure $p(\mathbf{x}, t)$ is a force acting on the surface S into the direction of a chosen unit normal $\mathbf{n}$. If S is a shear layer in the fluid, where particles above the surface have a significantly different velocity as the particles below the surface, a high amount of diffusion occurs, i.e., the particles interact with each other. Faster particles transfer momentum across the surface and slower particles slow down the faster ones. It can be said that there is stress along the surface. This is expressed by the stress tensor $\sigma(\mathbf{x}, t)$.

For the definition of σ, three assumptions are made: First, σ linearly depends on the velocity gradient tensor $\nabla\mathbf{v}$. Second, if the fluid undergoes a rigid body rotation, this should have no effect on the diffusion of momentum. By interpreting σ as an operator, it has therefore to obey

$$\sigma(\mathbf{U} \cdot \nabla\mathbf{v} \cdot \mathbf{U}^{-1}) = \mathbf{U} \cdot \sigma(\nabla\mathbf{v}) \cdot \mathbf{U}^{-1}, \tag{2.13}$$

where U is an orthogonal matrix. Last, the balance of angular momentum should be obeyed by σ, which leads to σ being symmetric. Note that these assumptions approximate real particle motion.

It can be shown that the only way σ can fulfill this assumption is by:

$$\sigma = \lambda(\operatorname{div}\mathbf{v})\mathbf{I} + 2\mu\mathbf{S}_\mathbf{v} = 2\mu\left[\mathbf{S}_\mathbf{v} - \frac{1}{3}(\operatorname{div}\mathbf{v})\mathbf{I}\right] + \zeta(\operatorname{div}\mathbf{v})\mathbf{I}, \tag{2.14}$$

where $\mathbf{I}$ is the identity, $\mathbf{S_v}$ the symmetric part of $\nabla\mathbf{v}$, and $\zeta = \lambda + \frac{2}{3}\mu$. Thereby, μ is typically called the *first coefficient of viscosity* and ζ the *second coefficient of viscosity*.

On the surface S, we can now describe the force acting on the surface as

$$\text{force on } S \text{ per unit area} = -p(\mathbf{x},t)\mathbf{n} + \sigma(\mathbf{x},t)\cdot\mathbf{n}. \tag{2.15}$$

Newton's second law (force = mass × acceleration) states that for any portion of fluid W_t, the change of its motion is proportional to the forces acting on the fluid. This is called balance of momentum. In its integral form it is written as

$$\frac{d}{dt}\int_{W_t}\rho\mathbf{v}dV = -\int_{\partial W_t}(p\mathbf{n} - \sigma\cdot n)\,dA, \tag{2.16}$$

where $\rho(\mathbf{x},t)$ is the mass density.

The *transport theorem* states

$$\frac{d}{dt}\int_{W_t}\rho\mathbf{v}dV = \int_{W_t}\rho\frac{D\mathbf{v}}{Dt}dV. \tag{2.17}$$

For a vector field $\mathbf{v}$, $\frac{D}{Dt} = \frac{\partial}{\partial t} + (\mathbf{v}\cdot\nabla)$ is called the *material derivative*. In addition to the transport theorem, we use the *divergence theorem* that states

$$\int_{W_t}\operatorname{div}\mathbf{v}dV = \int_{\partial W_t}\mathbf{v}\cdot\mathbf{n}dA. \tag{2.18}$$

For a scalar field s, the divergence theorem yields

$$\int_{W_t}\nabla s dV = \int_{\partial W_t} s\mathbf{n}dA. \tag{2.19}$$

Thus, Equation (2.16) can be written as

$$\int_{W_t}\rho\frac{D\mathbf{v}}{Dt}dV = \int_{W_t} -\nabla p + \operatorname{div}(\sigma)\,dV. \tag{2.20}$$

Now, we have to compute $\operatorname{div}(\sigma)$. Using vector and tensor calculus operations and assuming a Cartesian coordinate system, we get

$$\begin{aligned}\operatorname{div}(\sigma) &= \operatorname{div}(\lambda(\operatorname{div}\mathbf{v})\mathbf{I} + 2\mu\mathbf{S_v}) \\ &= (\lambda+\mu)\nabla\operatorname{div}\mathbf{v} + \mu\Delta\mathbf{v},\end{aligned} \tag{2.21}$$

where $\Delta\mathbf{v} = \nabla(\operatorname{div}\mathbf{v}) - \operatorname{curl}(\operatorname{curl}(\mathbf{v}))$ is the *vector Laplacian*. In (three-dimensional) Cartesian coordinates, it can be written as $\Delta = \left(\frac{\partial^2}{\partial x^2} + \frac{\partial^2}{\partial y^2} + \frac{\partial^2}{\partial z^2}\right)$ applied to each component of the vector field. Note that we could write the above derivation for each vector component. This way, we would not need to use the divergence of a tensor.

Equation (2.20) can now be written as

$$\int_{W_t} \rho \frac{D\mathbf{v}}{Dt} dV = \int_{W_t} -\nabla p + (\lambda + \mu)\nabla \operatorname{div} \mathbf{v} + \mu \Delta \mathbf{v} dV \tag{2.22}$$

Since the equation holds for every portion of fluid W_t, we get

$$\rho \frac{D\mathbf{v}}{Dt} = -\nabla p + (\lambda + \mu)\nabla \operatorname{div} \mathbf{v} + \mu \Delta \mathbf{v}. \tag{2.23}$$

Together with the *continuity equation*

$$\frac{\partial \rho}{\partial t} + \operatorname{div}(\rho \mathbf{v}) = 0, \tag{2.24}$$

these equations are called *Navier-Stokes equation*. They describe the motion of particles in a Newtonian fluid. Sometimes another term that acts as a force f is added to the right side of Equation (2.23). For instance, this term can represent the gravitational force.

In this thesis, we will deal with fluids that are incompressible. This means that $\rho = \rho_0$ is constant. It follows from the continuity equation, that the field is divergence free. The *incompressible Navier-Stokes equations* are

$$\begin{aligned} \frac{D\mathbf{v}}{Dt} &= -\frac{1}{\rho_0}\nabla p + \nu \Delta \mathbf{v} + f, \\ \operatorname{div} \mathbf{v} &= 0. \end{aligned} \tag{2.25}$$

where $\nu = \frac{\mu}{\rho_0}$ is the *kinematic viscosity*.

2.3.2 Eulerian vs. Lagrangian viewpoints

A flow field can be observed in two different ways. First, the dynamic properties can be assigned to fixed coordinates in space and time. This is the *Eulerian viewpoint*. The flow is described as a field. Second, the *Lagrangian viewpoint* assigns the dynamic properties to moving fluid parcels. The equations are given for this specific particle. However, both viewpoints are equivalent and the equations can be transformed into each other. For details, we refer the reader to the book of Panton [Pan05] and the lecture notes of McDonough [McD87].

An example to understand the difference can be given by the measurement of wind on the earth. It is possible to build a grid of weather stations at fixed positions on a continent. They will measure the wind vectors at the points $(\mathbf{x}, t)$. The resulting data is an Eulerian representation of the wind vector field on earth $\mathbf{v}(\mathbf{x}, t)$. Another way to measure weather is by a registering balloon. It is released at a certain position and is advected by the flow. It follows the path line of a certain particle X. The data captured by the balloon is given in the Lagrangian representation. For a sequence of successive positions, the

velocity is given by the temporal derivative of the position x of the balloon at time t

$$\mathbf{v}(X,t) = \frac{\partial \mathbf{x}}{\partial t}(X,t). \tag{2.26}$$

An important derivative in this setting is the material derivative as introduced in the last section:

$$\frac{D}{Dt} = \frac{\partial}{\partial t} + (\mathbf{v} \cdot \nabla). \tag{2.27}$$

It is sometimes also called *substantial derivative* or *Lagrangian derivative*. It measures the change of a quantity along the path line over time. Thus, it links the Lagrangian view to the Eulerian view: for a given quantity $f(\mathbf{x}, t)$ – scalar or vector valued –, the material derivative

$$\frac{Df}{Dt}(\mathbf{x},t) = \frac{\partial f}{\partial t} + v \cdot \nabla f \tag{2.28}$$

defines a scalar or vector field that can be evaluated at each position in space and time. However, the values are directly linked to certain particles.

2.3.3 Galilean invariance

Using the Eulerian viewpoint, a flow field has to be evaluated in a certain *frame of reference*, which is a given coordinate system in which the field is described. Typically, there is no distinguished frame of reference.

The different coordinate systems of the frame of references can be transformed into each other. An important subset of the possible transformations are *Galilean transformations*. The observer changes his viewpoint in the new coordinate system S' with a relative constant, non-accelerated velocity to the original viewpoint in the coordinate system S. Let $\mathbf{u}$ be this constant relative motion of the frames of references, i.e., $(\mathbf{x}', t') = (\mathbf{x} - \mathbf{u}t, t)$ whereby x' and x represent the spatial coordinates with respect to S' and S, respectively. Note that for a Galilean transformation $t = t'$. Furthermore, let $\mathbf{v}$ be the flow field with respect to the frame of reference S and $\mathbf{v}'$ be the transformed flow field with respect to the frame of reference S'. Then the two flow fields are transformed into each other by $\mathbf{v}' = \mathbf{v} - \mathbf{u}$, which is a Galilean transformation.

Now, a scalar, vector, or tensor field derived from the flow field is called *Galilean invariant* if its values do not change under a Galilean transformation. For instance, the velocity is changed under a Galilean transformation as can be seen above. It is therefore not Galilean invariant. On the other side, the Jacobian of a flow field is Galilean invariant, since its entries do not change by a Galilean transformation – the derivatives do not reflect a change of the velocity function by a constant vector.

Even though the velocity is one component of the material derivative, it is anyway Galilean invariant, which is shown in the following. For an arbitrary function $f'(\mathbf{x}', t')$ with respect to S', its value is given by the function value

$f(\mathbf{x}' + \mathbf{u}t', t')$ of a function f in S. Computing its temporal derivative, we get $\frac{\partial f'}{\partial t'} = \frac{\partial f}{\partial t} + (\mathbf{u} \cdot \nabla f)$. Since f was arbitrary, we get for the material derivative in S'

$$\begin{aligned} \frac{D}{Dt'} &= \frac{\partial}{\partial t'} + (\mathbf{v}' \cdot \nabla') \\ &= \frac{\partial}{\partial t} + (\mathbf{u} \cdot \nabla) + ((\mathbf{v} - \mathbf{u}) \cdot \nabla) \\ &= \frac{\partial}{\partial t} + (\mathbf{v} \cdot \nabla) \\ &= \frac{D}{Dt} \end{aligned} \tag{2.29}$$

Note that despite changing the frames of reference $\nabla = \nabla'$. Thus, the material derivative of a quantity is the same in both frames of reference and is Galilean invariant.

Chapter 3

Related work

In the last chapter, the foundation and its related work was given. In this chapter, we present other work that is related to the topics in this thesis, i.e., vector field visualization, feature extraction in and exploration of time-dependent flow fields. Since this thesis is also concerned with feature tracking, we will briefly summarize publications on this topic in the last section of this chapter.

3.1 Vector fields – visualization

While it is possible to depict a vector field by arrows, this simple visualization cannot represent the whole complexity of flow fields. In this thesis, we therefore apply different techniques to visualize two-dimensional time-dependent flow fields. One class of algorithms uses textures to visualize two-dimensional flow fields. A good overview of these dense visualization techniques is given in the publication of Laramee et al. [LHD+04]. A prominent example of these methods is Line Integral Convolution (LIC). It was first introduced by Cabral and Leedom [CL93]. LIC blurs a noise texture along the stream lines of a vector field. A fast algorithm was given by Stalling and Hege [SH95]. They reuse parts of the stream lines for an efficient computation of LIC.

While LIC gives a dense representation of the fields, sometimes the actual stream lines result in a better representation of the flow field. To cover all interesting structures, e.g., the critical points, a sensible seeding of the stream lines has to be applied. We apply an approach that was presented by Rosanwo et al. [RPP+09], which is based on vector field topology as proposed by Verma et al. [VKP00]. An overview of topology based flow visualization is given by Hauser et al. [HLD02]. Partition-based techniques were summarized by Salzbrunn et al. [SJWS08].

To visualize three-dimensional or two-dimensional time-dependent flows, LIC is not appropriate. Here, the direct rendering of stream lines is useful.

Unfortunately, the three dimensional depth of the individual lines can be misinterpreted. Zöckler et al. [ZSH96] presented an approach to add illumination to stream lines. This approach was later enhanced by Mallo et al. [MPSS05].

Sometimes, it is not sufficient to depict the evolution of particles, but the development of lines. This results in the computation of stream, streak or path surfaces. A good overview of methods computing geometric representations of flow is given by McLoughlin et al. [MLP+10].

3.2 Vector fields – feature extraction and exploration

To analyze flow data sets, it is possible to reduce the data to a set of interesting structures – often called features. In the context of flow visualization, the focus lies on mainly two types of structures in the recent years: vortices and Lagrangian coherent structures as identified by the finite-time Lyapunov exponent. A vast amount of publications deals with different aspects of the definition, extraction, and interpretation of these structures. These are presented in the following.

3.2.1 Vortices

The definition and extraction of vortices in fluid flows is topic of many publications in the fields of fluid mechanics and flow visualization. Despite the importance of flow structures, there is still no unique mathematical definition of a vortex. Rather, the different kinds of applications entail different needs for appropriate vortex definitions. For a good overview, we refer to Post et al. and Fuchs et al. [Pos03, FKS+10]. In addition, methods to analyze time-dependent vector fields have been proposed. There are many promising approaches; we refer to Pobitzer et al. [PPF+10] for an extensive overview of the recent publications.

Vortices can be extracted analyzing the geometric properties of trajectories of particles. For instance, Sadarjoen et al. [SP00] proposed an approach using stream line curvature to locate vortices.

Alternatively, vortices can be extracted as extremal structures of a scalar field derived from the velocity as done in this thesis. Such quantities are vorticity, pressure, helicity, or normalized helicity. Hunt [Hun87] presented the Q-criterion. For two-dimensional flow fields, the quantity was derived independently by Okubo [Oku70] and Weiss [Wei91]. Jeong and Hussain proposed the λ_2 value [JH95]. Recently, Haller proposed a feature identifier that is rotation invariant [Hal05]. These quantities build the analytic foundation for the extraction of vortical structures. Elaborated algorithms enable the extraction of vortices in complex flows. Stegmaier et al. [SRE05] extract vortices in a three-dimensional steady flow field based on the λ_2-criterion. They introduce a vortex browser to select and compare different kinds of vortices in a dataset. Schneider et al. [SWC+08] apply a contour tree extraction algorithm to different derived quantities such as λ_2 and pressure. They extract vortices as iso-surfaces of these quantities. Their framework is able to find similarities between different features and it is applied to various three-dimensional steady flows. Sahner et al. [SWTH07] used the Okubo-Weiss criterion to extract vortex and strain skeletons in three dimensional flows. Schafhitzel et al. [SBV+11] recently proposed a visualization and tracking system based on the λ_2 measure. In principle, every algorithm that is able to track extremal

structures in scalar fields is able to extract vortex core lines. Due to their wider applicability, these methods are presented separately in Section 3.3.

Different methods employ the parallel vectors operator as introduced by Peikert et al. [PR00] to compute vortex core lines. Theisel et al. [TSW+05] generalize the use of the parallel vectors operator to track vortex core lines. Weinkauf et al.[WSTH07] also used the parallel vectors operator to extract cores of swirling particle motion. This extraction approach was also used by Fuchs et al. [FPH+08] for unsteady flow vortices.

Most of the methods mentioned above are based either on streamlines or the Jacobian matrix. They are well-suited for analysis of single time-slices but not for characteristics of unsteady flow fields. Thus, more attention has been paid to methods based on path line analysis, representing the Lagrangian point of view. Theisel et al. [TWHS05] have presented an extension of stream line topology to path lines. Salzbrunn et al. [SGSM08] proposed a framework based on path line predicates. A Boolean function decides if a path line, constricted to the data domain, exhibits a certain property of interest. Fuchs et al. [FPS+08] accumulate Eulerian quantities along path lines to add a Lagrangian view. Similarly, Shi et al. [STW+08] explore the dynamical process of a flow by averaging the kinetic energy and momentum along path lines.

3.2.2 Vortex regions

Often, not only the vortex core line, but also its region of influence is of interest. Extraction techniques for these vortex regions can be divided in the following categories:

First, there are approaches that use an indicator function related to vortical activity. Here, the above mentioned vortex-related quantities can be used. A vortex region can be defined through a threshold that distinguishes the influence region of the vortex from the rest of the domain. Iso-surface extraction can be used to visualize the region boundary. As a drawback, using iso-surface extraction, it is not possible to distinguish between nearby vortices, if their regions partially merge. Moreover, one has to choose a global threshold parameter, which is quite arbitrary, since there is only an intuitive notion of vortex activity for the mentioned quantities. Since some of the quantities define vortex strength, there may be no threshold value to extract the regions of both strong and weak vortices. As a remedy, Schneider et al. [SWC+08] proposed an extraction algorithm for vortex regions (based on λ_2) using the contour tree for the selection of the geometry. An exploratory technique to visualize time-dependent vortices in three-dimensions was introduced by Tikhonova et al. [TCM10].

The second class of definitions of vortex regions uses the combination of a vortex indicator function and a geometrical extraction algorithm. Here, vortex regions are typically extracted for previously defined vortex core lines by

sending out a fan of rays from the center. The rays are cut, if a certain criterion is met on the ray. The resulting regions are restricted to star-shaped geometries seen from the vortex core. These are not arbitrary star-shaped regions. Banks and Singer [BS95] introduced this method to construct a vortex hull as a series of connected contour lines. The contour line that connects the endpoints of the rays is the outer boundary of the vortex in that plane. They used a pressure threshold to mark the boundary of a vortex region induced by the length of the rays. Bauer et al. [BPSS02] used a threshold of the absolute value of the imaginary part of the complex eigenvalues of the Jacobian instead of the pressure threshold. Furthermore, Stegmaier et al. [SRE05] used a threshold of λ_2 to determine the termination of the rays. Garth et al. [GTS+04a] searched for local maxima of the tangential velocity component using the Rankine vortex model as a basis for their definition. Jankun-Kelly et al. [JKJTM06] build an approach to robustly extract vortices based on local extrema of different scalar fields. They extract three-dimensional vortices using a predictor-corrector method and k-means clustering to find the correct extremal structures. The corresponding vortex regions are also based on the maximum tangential velocity. Note that their extracted vortex regions depend on the frame of reference, since velocity is Galilean variant.

The third category consists of approaches that use a purely geometric definition of vortex regions. Sadarjoen and Post [SP99] searched for streamlines with a winding angle of 2π. They restricted their definition to streamlines for which the distance of start end endpoint is "close". A clustering of streamlines belonging to the same vortex result in an elliptical representation of the vortex regions. Reinders et al. [RSVP02] extended the approach to 3D. Petz et al. [PKPH09] defined vortex regions searching for closed streamlines in rotated version of the vector field. They were able to build a hierarchy of these regions. All these approaches are not Galilean invariant, since they use streamlines that depend on the chosen frame of reference.

3.2.3 Finite-time Lyapunov exponent

In Chapter 4, we will discuss an approach to Lagrangian coherent structures (LCSs) by Haller [Hal01a, Hal02] called finite-time Lyapunov exponent (FTLE). FTLE measures the maximum separation of close-by particles of a time-dependent flow field after a fixed, finite particle advection time. We give details on LCSs and FTLE in Section 4.1. While we also introduce further publications in the field of fluid mechanics there, some approaches to FTLE that were brought up in the visualization community will be discussed in the following.

Many papers have been published dealing with efficient and robust computation of the FTLE fields based on the flow map and the extraction of their ridges. Sadlo et al. [SP07] present a ridge extraction algorithm with filtered

adaptive mesh refinement. Garth et al. [GGTH07] propose an adaptive refinement algorithm utilizing the coherence of particle paths to generate smooth approximations of the FTLE field. An approach to extract the FTLE ridges by grid advection has been introduced by Sadlo et al. [SRP11].

In addition, the physical meaning of FTLE was investigated. Sadlo et al. [SW10] analyzed the connection of FTLE to a time-dependent version of vector field topology. While Shadded [Sha06] has found that along FTLE ridges there is a small amount of material transport, Germer et al. [GOPT11] introduced an approach to extract structures from the FTLE field without any material transport. They therefore use level sets instead of ridges. Pobitzer et al. [PPF+11] filtered FTLE structures that are due to shear in the flow. Fuchs et al. [FSP12] investigated scale-space approaches for FTLE ridges.

3.3 Tracking algorithms to compute trajectories of critical points

In this section, we give a brief overview of the existing methods to track features in time-dependent data sets.

Originally, the concept of tracking is located in the field of computer vision. Here, objects in images are traced, e.g., the movement of a person in a video. A good overview of the methods in this area is given in [YJS06]. In the area of visual data analysis, the tracking of features in different data sets is more common. The algorithms can thereby be divided into three classes depending on the treatment of the temporal dimension [Pos03].

First, one can extract the features in each slice individually and then employ a correspondence algorithm that matches the features of one time slice with the features of the next one. The advantage of these methods is that no temporal interpolation is needed. On the other hand, the detection of events such as bifurcations is complicated. These have to be evaluated implicitly using an appropriate event function. A common approach to match the features is to use distance metrics based on the domain and attribute space. Using application specific attributes, appropriate heuristics can be used to fit the algorithm to the given sort of data. Examples of such attributes are the size of the features or their shape. For instance, Caban et al. [CJR07] use texture characteristics for their tracking approach. Using distance metrics, features are typically matched, if their distance is below a certain threshold. Examples of these algorithms are given in [SSZC94, RPS99, LBM$^+$06, dLvL01]. While these approaches use Euclidean distances, the feature overlap can also be used as shown by Silver et al. [SW97]. A similar approach based on the contour tree was introduced by Sohn et al. [SB06]. Instead of using local metrics, a global approach might improve the correspondence resulting in a best matching as proposed by Ji et al. [Ji06]. Another improvement is to use motion prediction as done by Reinders et al. [RSVP02]. Last, the position of the features of the current time step can be used as a initial guess for the next time step. This results in a progressive tracking approach as proposed by Bajaj et al. [BSS02].

Instead of treating each time slice independently, it is possible to consider the temporal as another spatial dimension. The features are extracted in the space-time. Note that this increases the dimension of the feature extraction by one, which can complicate the algorithm or increase the computational costs. For instance, a two-dimensional time-dependent scalar field can be interpreted as a three-dimensional scalar field. Here, three-dimensional scalar field topology would extract the time-dependent features. After the tracking, typically an event analysis is done. Weigle et al. [WB98] and Ji et al. [JSW03] proposed methods to extract the iso surface in space-time. Weber et al. [WBD$^+$11] and Bremer et al. [BWP$^+$10] introduced methods to do the topological event anal-

ysis based on the Reed-Graph of the surface resulting from sweeping contours. For time-dependent two- and three-dimensional flow fields, topology tracking has been performed by Tricoche et al. [TWSH02] and Garth et al.[GTS04b]. Their method is applicable to vector field that are composed of space-time cells in which the values are only linearly interpolated. This has the advantage that the events are restricted to the boundary of that cells and the entry and exit points of the critical points has only to be found on that boundary. Using a parallel vector test on each cell, Bauer et al. [BPSS02] introduced a method to track vortex core lines. While giving accurate results, these methods are sensitive to noisy data and a high feature density. To reduce the number of extracted features and events, a common practice is to delete short living features. A combinatorial approach to track critical points is based on the definition of Jacobi sets as proposed by Edelsbrunner et al. [EH04]. It consists of Jacobi edges, which are extracted from a spatiotemporal simplicial complex assuming a linear interpolant. The decision whether an edge belongs to the Jacobi curve involves the topological analysis of the lower link of vertices and edges of the simplicial complex. While providing a nice theoretical framework, the resulting Jacobi curves of real data sets are often very complex and hard to analyze. Based on this work it is also possible to track the evolution of the Reeb graph of a scalar function [EHM$^+$08].

The algorithms in the third class consider space-time in a combination of the aforementioned types. They consider the temporal as an extra dimension, but these algorithms do not look at each time slice individually. In contrast, the Feature Flow Fields (FFFs) approach introduced by Theisel et al. [TS03] extracts the tracked critical points by tracing a tangent curve in a derived field of the scalar (gradient) or vector field. A combinatorial method that is similar to the notion of FFFs has been proposed by King et al. [KKM08]. This approach gives the mathematical foundation of the efficient version of Reininghaus et al. [RKWH12] for two-dimensional scalar fields. Both are presented in Section 2.2.2.

Chapter 4

Flow analysis based on the finite-time Lyapunov exponent

In this chapter, we discuss an approach to Lagrangian coherent structures (LCS) that uses the finite-time Lyapunov exponent (FTLE). The FTLE measures the separation of infinitesimally close particles for an advection time T. Integrating path lines in the backwards direction, the FTLE also determines the convergence of particles. To distinguish the resulting fields, the forward FTLE is written as FTLE^+ and the backwards FTLE as FTLE^- in the remainder of this chapter.

In Section 4.1, the idea of LCSs in the context of the FTLE is given. The computation method based on flow maps is also described. Afterwards, in Section 4.2, a new computation method is proposed that links the FTLE to a single path line. This method is called localized FTLE (L-FTLE). How far the concept of FTLE is applicable to complex flow behavior is discussed in Section 4.3.

4.1 Lagrangian coherent structures in the context of FTLE

The concept of *Lagrangian coherent structures* (LCSs) plays a fundamental role in the analysis of time-dependent flow fields. The idea of *coherent structures* (CSs) developed about fifty years ago in the context of semi- or fully turbulent flows [Hus83]. One of the first observations of such large-scale structures was made by Roshko and Brown [BR74] at a turbulent plane mixing layer using shadowgraphs. Before CSs were found, it was assumed that turbulent flows are only determined by chaotic particle motion where structures of

different scales arise, dissolve, and affect each other. The analysis of the vast amount of structures was restricted to statistical methods. Today, there is a general consensus that besides the chaotic motion of particles, there are coherent structures exhibiting a more coarse and orderly flow behavior. The finding that turbulent flow is not purely chaotic but embodies orderly structures had a deep impact on fluid mechanics.

However, despite their importance, there is no commonly accepted mathematical definition of coherent structures. Moreover, Hussain [Hus86] states that "*in principle, concepts like coherent structures are best left implicit*". On the other side, the extraction of CSs is a fundamental goal in the analysis of complex flow fields. As a result, a variety of individual interpretations and more or less formal definitions of CSs have been proposed, from a Eulerian as well as Lagrangian point of view. Examples are the definitions by Michalke [Hus86] or Farge [FSK98], both proposing a "*coherence function*". Others give more conceptual definitions. Yule [Yul81] suggests that coherent structures should follow three requirements: (i) being repetitive, (ii) survive distances larger than structure size, (iii) significantly contribute to the kinetic energy. While Hussain considers these conditions, at least partly, as "*unnecessary and unrealistic*", he defines coherent structures as "*connected turbulent fluid mass with instantaneously phase-correlated vorticity over its spatial extent*" [Hus83]. Farge states that "*the only definition of a coherent structure that seems objective is a locally meta-stable state, such that, in the reference frame associated with the coherent structure, the nonlinearity of Navier Stokes equations becomes negligible*" [FSK98].

In the past ten years, an approach to LCSs by Haller became quite popular. He proposes a concept of distinguished material lines or surfaces in the flow field [Hal00]. To extract these structures, he refers to the finite-time Lyapunov exponent (FTLE) [Hal01a]. Haller has suggested characterizing LCSs as extremal structures of both the forward and backward FTLE field. Later on, he has relativized this view presenting an example where FTLE ridges do not necessary mark LCSs [Hal02]. But still, FTLE ridges represent LCSs in a wide range of configurations and are used in many applications [PD10]. Shadden even defines LCSs as ridges in the FTLE [SLM05, Sha06] fields.

4.1.1 Flowmap FTLE (F-FTLE)

The FTLE is based on the Lyapunov exponent (LE), which originates in the theory of dynamical systems. The LE measures the rate of separation of infinitesimally close trajectories exhibiting exponential behavior with time, cf. Nese [Nes89]. It is defined as $\lim_{t\to\infty} \frac{1}{t} \ln \frac{\delta(t)}{\delta(0)}$, where $\delta(t)$ is the deviation of the trajectories at time t. It is constant along a trajectory and measures the predictability of a dynamical system.

In general, flow data is only available for a finite-time interval and does not

follow a periodic pattern. This makes LE not applicable. Thus, the LE is only computed for a finite advection time of particles T. With FTLE, this concept has been introduced to flow analysis by Haller [Hal01a]. He proposed to compute the FTLE using the flow map of a vector field. In the following, this method is described.

Let $\mathbf{v} : \mathbb{R}^d \times I \to \mathbb{R}^d$ be a d-dimensional, time-dependent flow field. The advection of a particle with the flow for a time T can be described using the *flow map*

$$\phi : \mathbb{R}^d \times I \times I' \to \mathbb{R}^d. \tag{4.1}$$

It maps a particle at position $\mathbf{x}_0$ and time t_0 onto its advected position $\phi(\mathbf{x}_0, t_0, T) = \phi_{t_0}^T(\mathbf{x}_0)$ at time T. The gradient of the flow map

$$\nabla\phi_{t_0}^T : \mathbb{R}^d \to \mathbb{R}^{d\times d} \tag{4.2}$$

characterizes the local flow deformation of a particle neighborhood. Maximum stretching of nearby particles is given by the spectral norm $||.||_\lambda$ of $\nabla\phi_{t_0}^T$. Flow map FTLE (F-FTLE) is defined as the normalized maximal separation

$$\text{F-FTLE}^+(\mathbf{x}_0, t_0, T) = \frac{1}{T}\ln(||\nabla\phi(\mathbf{x}_0, t_0, T)||_\lambda). \tag{4.3}$$

In practice, the flow map is mostly computed by sampling particles on regular grids. This introduces a hidden parameter δ_x, the spatial sampling distance of nearby particles. During advection, nearby particles might separate far-off, and do not measure the local separation rate accurately. Thus, δ_x is a crucial parameter for the computation of FTLE.

4.1.2 Concepts for Lagrangian coherent structures

Despite the efforts to define LCSs, there is still no consensus. However, in all of the above mentioned characterizations, there are common ideas of what LCSs should look like. In the following, two notions are briefly described and their relation to FTLE is discussed.

Material lines. Many discussions pursue the idea that temporally developing flow features should be close to material lines. Such features result in structures building a kind of material barrier, minimizing crossflow. These lines are distinguished material lines in the flow. Haller defines a material line as a "smooth curve of fluid particles advected by the velocity field" and describes them as finite-time invariant manifolds [Hal01a]. In terms of integral lines, material lines correspond to time lines in a flow field. Material lines can be interpreted as transport barrier – similar to the separatrices of the vector field topology of steady flow fields. As mentioned above, Haller proposed to define LCSs boundaries as distinguished material lines advected with the flow. As an example, he refers to hyperbolic repelling material lines. Using the

FTLE fields as indicators for these distinguished material lines, Shadden has shown that the resulting structures are approximately advected by the flow with negligible fluxes across the structures [SLM05]. This puts FTLE into context with material lines.

Path line features. The second common idea is that the LCSs should be connected to particle motion. Thereby, a cluster of path lines is marked to be the support of the LCSs. Salzbrunn et al. [SGSM08] proposed a framework based on predicates to select path lines. A Boolean function decides if a path line, constricted to the data domain, exhibits a certain property of interest. Thereby, two groups of predicates can be distinguished. The first group considers the path line as a geometric entity. The second group relies on properties derived from the flow like vorticity. This framework is very general. Many path line based approaches, including material surfaces, can be subsumed under this concept. Note that methods that do not investigate the entire available path line, but only a finite-time interval T, do not strictly follow this idea of path line predicates. Typically, the computation of FTLE utilizes the flow map. Since this involves the integration of multiple path lines, it does not strictly fit into the framework of path line predicates. In Section 4.2, another variant of the FTLE computation is given – called *localized FTLE* (L-FTLE). It bases the computation on the local separation generated by the Jacobian along a single path line. This approach comes closer to the concept of path line predicates.

4.2 Localized FTLE

Since the introduction of FTLE, many papers have been published dealing with efficient and robust computation of the FTLE fields, cf. Chapter 3.2.3. All these approaches base the computation of the FTLE on the flow map (F-FTLE). However, this method has two main limitations. First, for the computation of a single FTLE value, four path lines have to be traced and their initial distance δ_x has to be set, which introduces a parameter. Second, the separation is not measured for the evolution of a single particle. For long integration times, far away separation events can have an influence on the resulting FTLE value that do not really correspond to the flow behavior in the vicinity of a single particle. Sometimes, renormalization is used. If the FTLE is thereby computed for a certain position using the flow map, the four path lines traced to compute the FTLE are restarted at the original path line. The intermediate flow map gradients are accumulated. However, this complicates the implementation.

To overcome the limitations, the localized FTLE method is introduced in the following. It is based on the integration of the Jacobian matrix J along a path line. Given a flow field $\mathbf{v}$, the Jacobian of $\mathbf{v}$ is a generator of separation. Its symmetrical part quantifies the separation along the path line. In addition to the definition, a fast implementation of the L-FTLE is given that efficiently reuses FTLE values of previous time steps following an idea similar to FastLIC [SH95]. Afterwards, the results are discussed and compared to the existing FTLE method.

4.2.1 Definition

Consider a pathline $\mathbf{p}(t) = \mathbf{p}(\mathbf{x}_0, t_0, t)$ for a particle started at space-time location $(\mathbf{x}_0, t_0)$. The deviation of trajectories of infinitesimally close particles started at $(\mathbf{x}_0 + \delta_0, t_0)$, with $\delta_0 \to 0$, is given by the differential equation

$$\dot{\delta}(t) = \mathbf{J}_\mathbf{v}(\mathbf{p}(t), t_0 + t)\delta(t). \tag{4.4}$$

Solving the differential equation yields

$$\delta(t) = exp\left(\int_0^t \mathbf{J}_\mathbf{v}(\mathbf{p}(\tau), t_0 + \tau)d\tau\right)\delta_0. \tag{4.5}$$

Given a finite time span T, the matrix

$$\Psi_T(\mathbf{p}) = exp\left(\int_0^T \mathbf{J}_\mathbf{v}(\mathbf{p}(t), t_0 + t)dt\right) \tag{4.6}$$

expresses the mapping of a neighborhood at the starting point $\mathbf{p}(0)$ onto its deviations at the end point $\mathbf{p}(T)$. Compared to the flow map approach, this matrix corresponds to the gradient of the flow map. Defining a temporal

discretization of the pathline $T = \Delta t \cdot N$, where Δt is the length of one time step and N the number of steps, Equation (4.6) can be approximated as

$$\Psi_T(\mathbf{p}) \simeq \prod_{i=0}^{N-1} \exp\left(\mathbf{J_v}(\mathbf{p}(i\Delta t), t_0 + i\Delta t) \cdot \Delta t\right). \tag{4.7}$$

L-FTLE is now defined as the largest separation of this mapping. It is computed as

$$\text{L-FTLE}^+(\mathbf{x}_0, t_0, T) = \frac{1}{T} \ln(||\Psi_T(\mathbf{p})||_\lambda), \tag{4.8}$$

where $||.||_\lambda$ represents the spectral norm of the resulting matrix.

The exponential of the matrix in Equation (4.4) can be solved analytically using the eigenvalues and eigenvectors of $\mathbf{J_v} = \nabla\mathbf{v}$. For a two-dimensional vector field and a matrix with complex eigenvalues λ_0, λ_1, the exponential is

$$\exp\left(\mathbf{J_v} \cdot \Delta t\right) = \mathbf{S} \begin{pmatrix} \exp(\lambda_0 \Delta t) & 0 \\ 0 & \exp(\lambda_1 \Delta t) \end{pmatrix} \mathbf{S}^{-1}, \tag{4.9}$$

with $\mathbf{S} \in \mathbb{C}^{2\times 2}$ is the coordinate transform into the eigenspace. Alternatively, for small Δt, the first order approximation of the exponential yields

$$\exp\left(\mathbf{J_v} \cdot \Delta t\right) \approx 1 + \mathbf{J_v} \cdot \Delta t. \tag{4.10}$$

4.2.2 Implementation and optimization

We implemented the new localized L-FTLE method and the flow map based F-FTLE method. Path lines are computed with a Runge-Kutta integration scheme of fourth order precision with step size control (RK4-3). A small tolerance was chosen for the step size control of the integrator, such that the FTLE results do not exhibit discretization errors.

The flow map for F-FTLE is computed on a regular grid. For each grid node, a path line is advected for the time T, and the destination is stored at the grid location. Central differences are used for gradient reconstruction of the flow map. Re-normalization is not performed. Grid resolution determines the sampling distance δ_x of nearby path lines.

Localized FTLE is computed directly for each path line. During path line integration, the Jacobian matrix of the velocity field is sampled at equidistant time steps Δt along the path line. Separation is accumulated with Equation (4.7), by either using Equation (4.9) or the approximation Equation (4.10). Gradients of the velocity field are computed consistently to the interpolation scheme of the underlying data. In the case of a time-dependent two-dimensional vector field on a triangular grid that is linearly interpolated, gradients are constant per triangle and linear between two time steps.

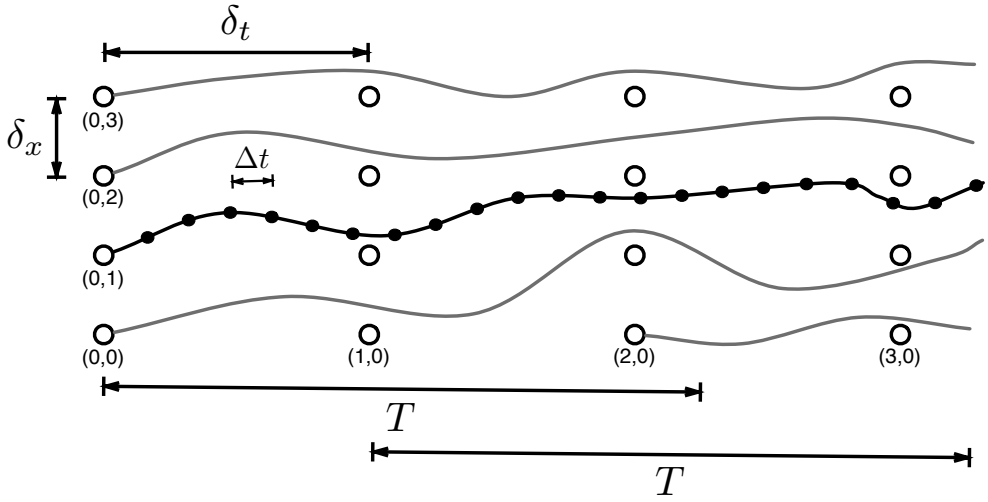

Figure 4.1 The path line started at the first time slice in $(0, 1)$ yields results for the grid points $(1, 1)$, $(2, 2)$ and $(3, 2)$. Small black dots on the path line indicate the sampling of the Jacobian with distance Δt. δ_x and δ_t denote the grid resolution. A new path line is started at $(2, 0)$ as none of the previous path lines get close-by to that grid point.

Fast L-FTLE. With *Fast L-FTLE*, we adapted the idea of FastLIC [SH95] to speed up L-FTLE computation for a sequence of time steps. Separation is re-used, by further accumulating the separation at the head, and retracting it at the tail of a path line. The separation of a moving active time interval T gives the L-FTLE values at passing locations.

Fast L-FTLE computation, see Figure 4.1, is done on a regular grid in the space-time domain, with spatial and temporal sampling distance δ_x and δ_t, determined by the grid resolution. Path lines are traced for all grid nodes of the first time slice, resulting in L-FTLE separation values for grid nodes that are touched by these path lines. Afterwards, additional path lines are traced until L-FTLE values are obtained for all grid nodes. A nearest neighbor interpolation was chosen for obtaining L-FTLE values on grid points.

4.2.3 Results

To evaluate the L-FTLE method and compare it to F-FTLE, it is applied to two different data sets: the cylinder data set, cf. Appendix A.4, and the cavity data set, cf. Appendix A.6.

Figure 4.2 depicts L-FTLE results in forward and backward time for $T = 3$ (3 periods) of the cylinder data set using a two-dimensional transfer function as proposed in [GLT+07]. Convergent regions with high values of L-FTLE$^-$ are colored blue, high values of L-FTLE$^+$ are colored red. Ridge structures and crossing points are clearly visible.

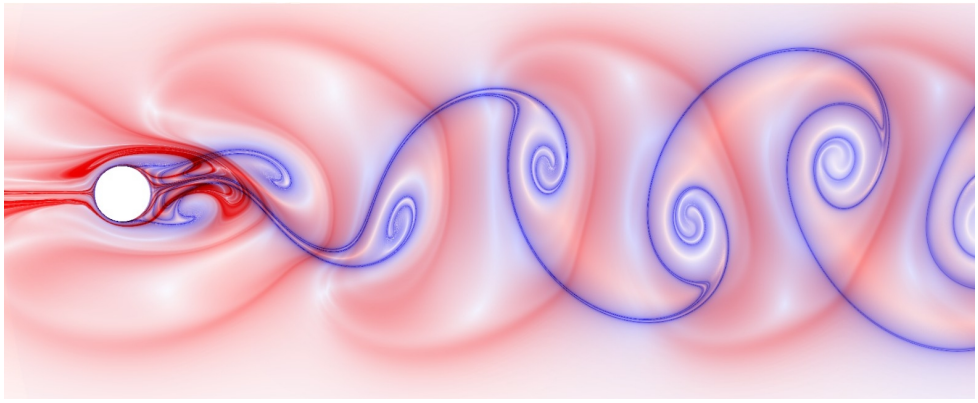

Figure 4.2 Simultaneous visualization of forward (red) and backward (blue) L-FTLE, integration time $T = 3$ periods.

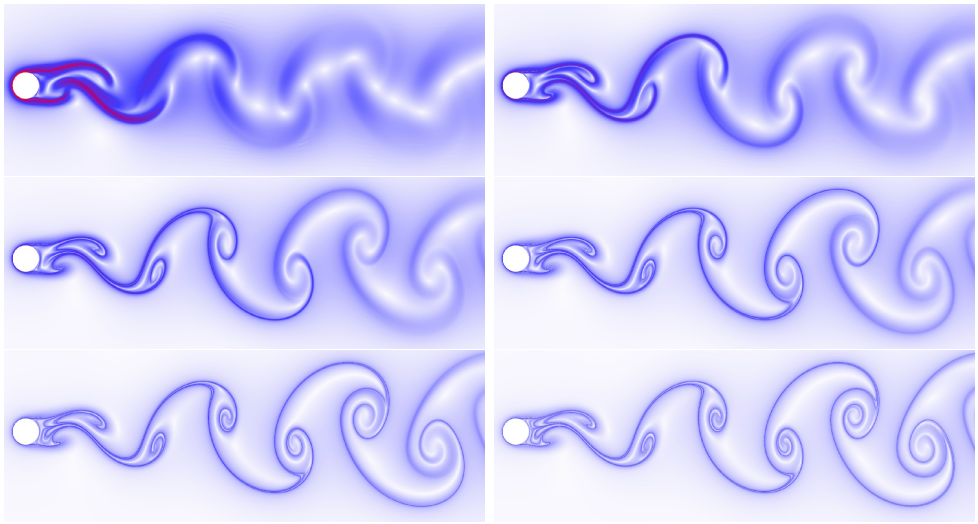

Figure 4.3 L-FTLE$^-$. Integration time varied in steps of 0.5 from $T = 0.5$ (top left) to $T = 3$ (bottom right).

Parameter Analysis. The computation of the FTLE field depends mainly on two parameters. The first parameter is the integration time T, which is a structural parameter that is inherent to the definition of FTLE. Changes in the results due to this parameter are part of the concept and have already been discussed in other papers dealing with FTLE, e.g., by Garth et al. [GLT$^+$07]. The second parameter Δt, a discretization parameter, should not have a strong influence on the result.

The influence of the integration length T to FTLE is depicted for L-FTLE$^-$ in Figure 4.3, showing the cylinder data set. The integration length is varied between 0.5 and 3 periods. The longer the integration time, the more pro-

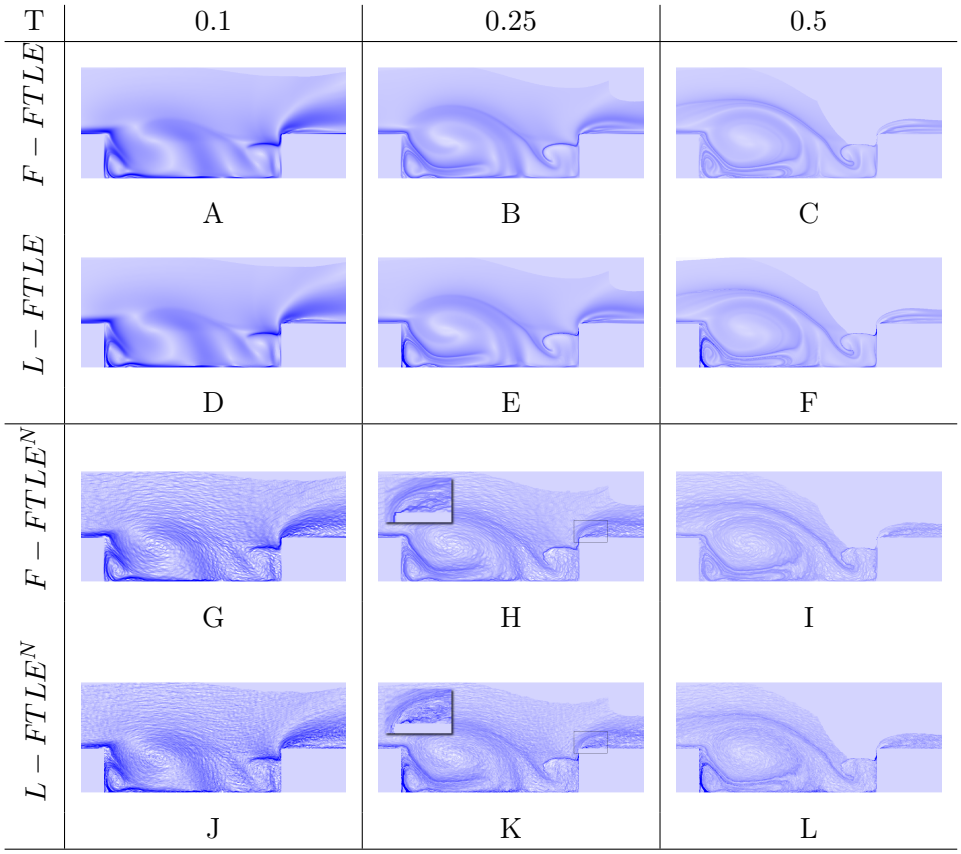

Table 4.1 Comparison of F-FTLE and L-FTLE. The effect of noise (label:^{N}) is depicted in the pictures for different integration times T. The data set is a cavity flow field. The noisy version is generated by adding a Gaussian noise to the vector directions.

nounced are the FTLE structures. Centers of spiraling motion are deducible. L-FTLE$^+$ results of the cavity data set for different integration times are depicted in Table 4.1 D,E,F. Three main vortices are surrounded by ridges of high separation. Ridge structures get sharper for larger integration times.

In Figure 4.4, a comparison of different sampling distances Δt for an integration time $T = 1$ of the cylinder data set is shown. Δt was set to 1/120, 1/30 and 1/3. The thin white line in the images mark a cutting line, the values of L-FTLE$^+$ along the lines are depicted as profiles in Figure 4.5. Path line accuracy is not affected by the parameter and equal for the comparison. No difference can be seen between the two top images. The third image shows two converging black lines of low separation in the marked section. The profiles in Figure 4.5 reveal this more clearly. Only at a very coarse sampling distance of $\Delta t = 1/3$ notable differences can be observed. Even then, the global structure of the profile matches the fine-sampled profiles very well.

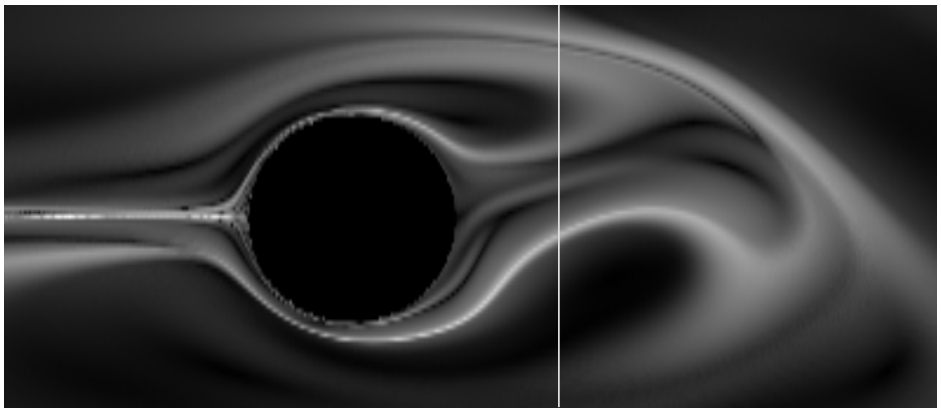

(a) $\Delta t = 1/120$

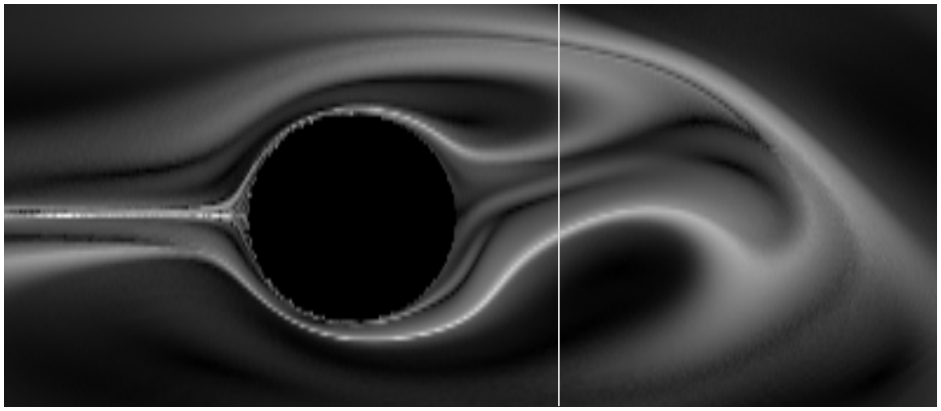

(b) $\Delta t = 1/30$

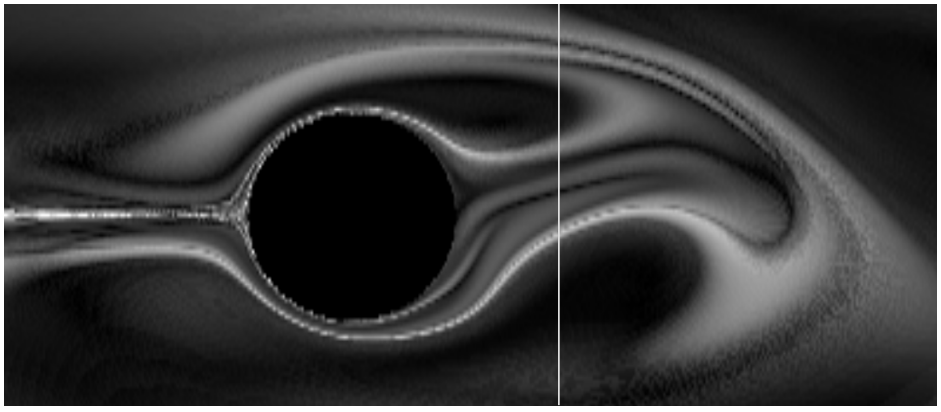

(c) $\Delta t = 1/3$

Figure 4.4 Comparison of L-FTLE$^+$ for integration time $T = 1$. The Jacobian of the vector field was sampled in steps of 1/120, 1/30 and 1/3. Even for very large sampling distances, the resulting separation fields look surprisingly alike. Accuracy of path line integration was in all cases identical. The perpendicular white lines denote the position of a cutting line used for the comparison in Figure 4.5.

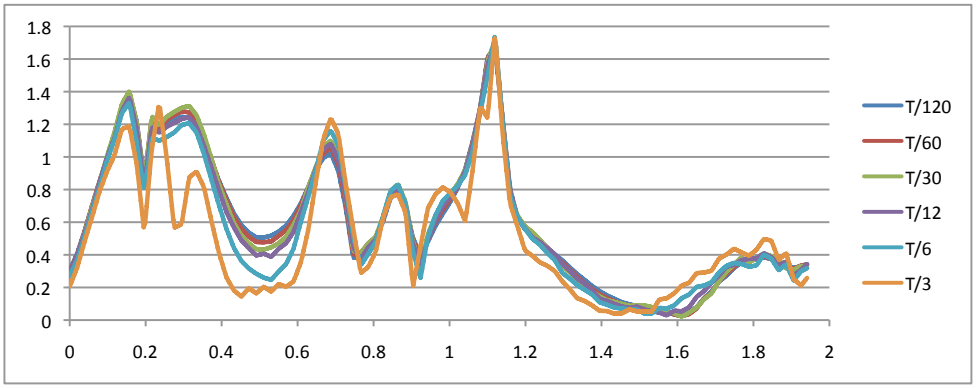

Figure 4.5 Comparison of Forward FTLE along a line as indicated in Figure 4.4 – the x axis from left to right corresponds to the lines from top to bottom. In addition to the images, sampling distances of $T/60$, $T/30$ and $T/6$ are depicted.

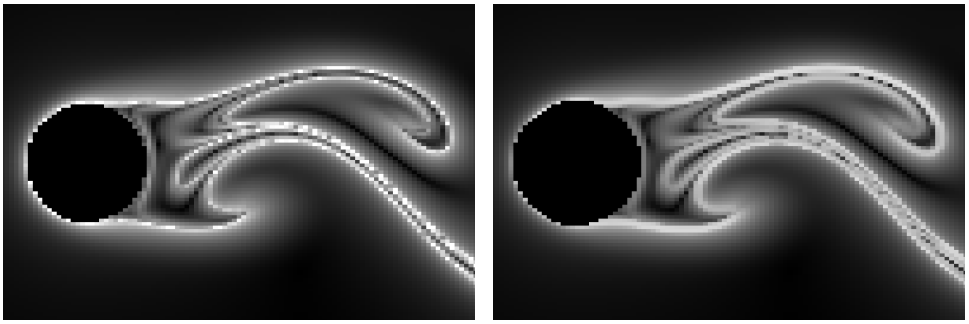

(a) L-FTLE$^-$ (b) F-FTLE$^-$

Figure 4.6 Comparison of L-FTLE$^-$ to F-FTLE$^-$ for $T = 2$ using the cylinder data set. In both cases, the grid resolution are the same and one path line is started per pixel. Apart from a slight blurring in (b), the results are identical. Blurring is due to the gradient approximation by central differences.

Comparison. As basis for the comparison of L-FTLE to the standard approach based on the flow map, both FTLE methods are implemented using the same path line integrator. For the F-FTLE computation, a central differences approach has been used to approximate the gradient of the flow map. The results are visualized applying the identical transfer function as shown in Figure 4.6 for FTLE$^-$. The resulting structures as well as the magnitude of separation are surprisingly similar for both cases. Hardly any differences can be noticed. The features from the L-FTLE approach are slightly sharper, which seems to be a consequence of the gradient reconstruction.

A comparison of F-FTLE$^+$ and L-FTLE$^+$ for different grid resolutions is presented in Figure 4.7. The flow map for F-FTLE is computed on a regular

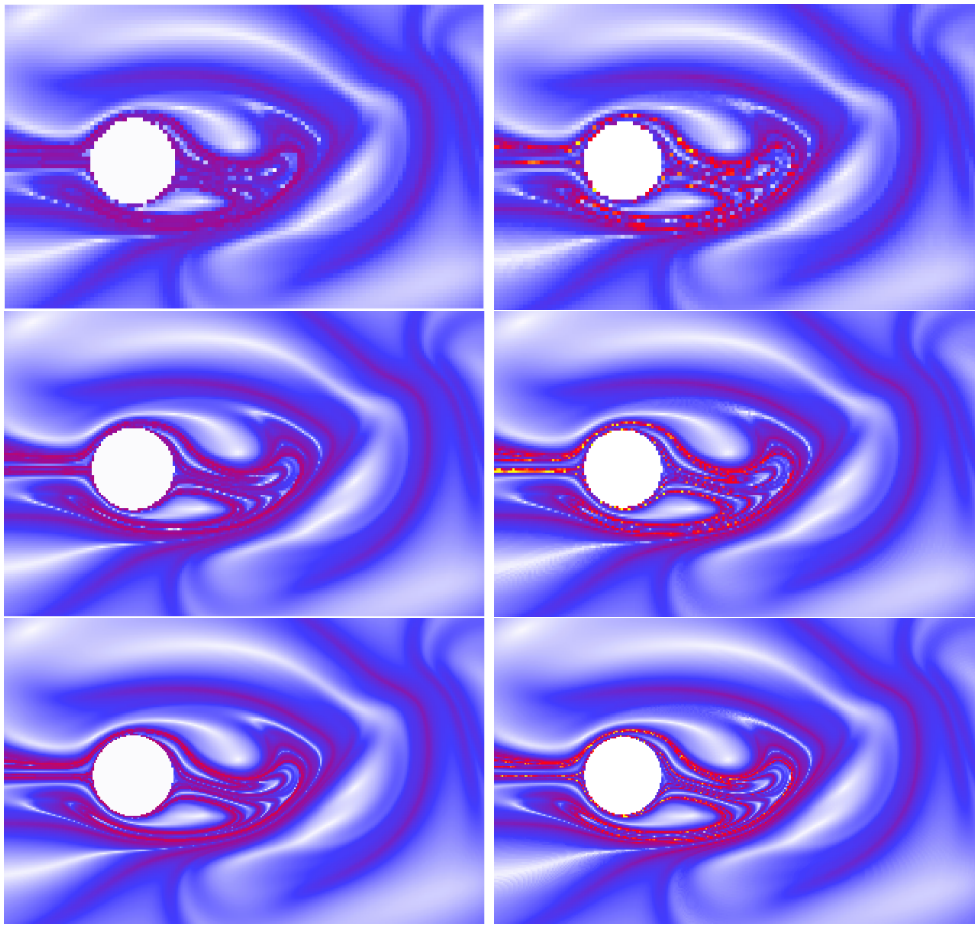

Figure 4.7 Comparison of F-FTLE$^+$ (left column) and L-FTLE$^+$ (right column) for different resolutions. Result resolutions are 120×80 (first row), 210×140 (second row) and 300×200 (third row). Integration time is $T = 3$.

grid. Thus, the sampling distance of adjacent grid nodes determines the distance of neighboring path lines and thus the accuracy of the resulting FTLE field. In contrast, the accuracy of the L-FTLE approach is determined by accuracy of the computation of the Jacobian independently from the sampling density. This leads to differences in the results especially in regions of high field frequencies, i.e., at sharp ridge structures of the separation. For lower resolutions, the F-FTLE approach results in a smoothed version of the original field. In Figure 4.7, this is reflected by the fact that the maximum separation values decreases with decreasing resolution for the F-FTLE approach, whereas it stays constant for the L-FTLE approach.

For the cavity data set, the results of the two methods are presented in Table 4.1. F-FTLE$^+$ results are shown in the first row, L-FTLE$^+$ in the second row. Nearly the same structures are obtained for both algorithms, but

Algorithm			L-FTLE		F-FTLE
			basic	fast	
R	T	Δt			
100^3	2	0.02	2 : 40	0 : 14	1 : 05
50^3	2	0.02	0 : 20	0 : 04	0 : 08
100^3	1	0.02	1 : 33	0 : 15	0 : 35
100^3	2	0.01	4 : 02	0 : 22	1 : 13

Table 4.2 Comparison of the basic and accelerated L-FTLE implementation. The main parameters were investigated as there are the resolution R (two spatial and one temporal component), the time span T and the sampling parameter Δt. The accelerated implementation has a speedup factor of 8 on average.

slight differences are observable. L-FTLE reveals some structures of strong separation for $T = 0.25$ and $T = 0.5$; with F-FTLE features do not emerge that clearly.

The performance of both approaches is compared in Table 4.2. The flow map approach is faster than basic implementation of the L-FTLE approach which has to evaluate the local separation at many sample points along the path line on an unstructured grid. On average, the new approach is a factor of 3 slower for the example. The Fast L-FTLE approach, however, outperforms the flow map FTLE implementation by a factor of 3.

L-FTLE Performance. Without exploiting the temporal coherence of L-FTLE, by advecting path lines for each time slice of the result individually, the runtime of implementation takes about 2 minutes and 40 seconds for computing the L-FTLE for 100 time slices on a 100^2 grid for the cylinder data set with $T = 2$ and $\Delta t = 0.02$ on standard hardware. Point location on the unstructured grid of the cylinder data set during path line tracing is one of the dominant tasks.

The same computation done with the accelerated Fast L-FTLE implementation takes only 14 seconds, a speedup factor of 11. A more detailed comparison is given in Table 4.2. On average, the accelerated implementation yields a speedup factor of 8. It can be seen that the parameter Δt has no influence on the acceleration factor. On the other side, the number of calculated path lines that is determined by the resolution has a clear impact as well as the length of each path line T. The implementation reuses separation values on a path line, no segment of a path line is computed twice. In Figure 4.8, a result for the cylinder data set computed with the accelerated implementation is depicted. Compared to the non-accelerated implementation, some artifacts due to nearest neighbor interpolation are visible, but the structures are nearly the same.

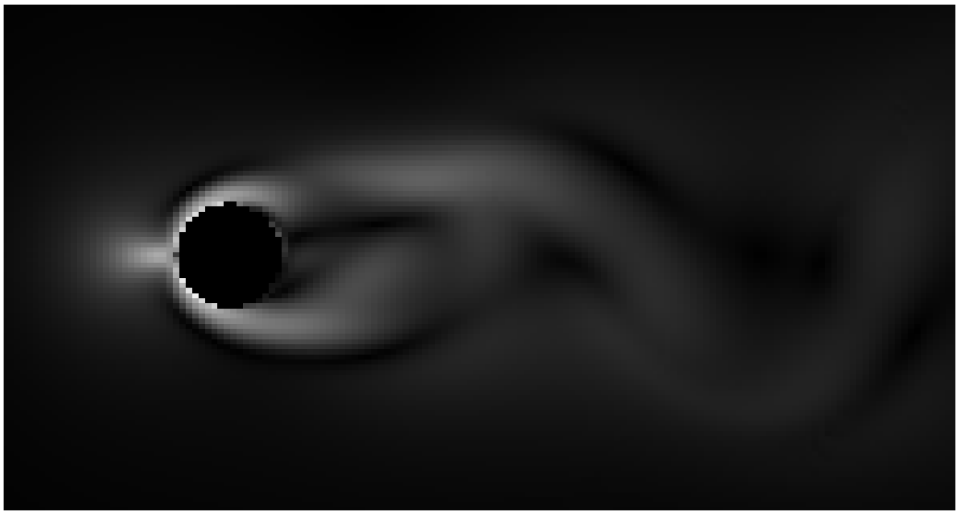

(a) L-FTLE$^-$

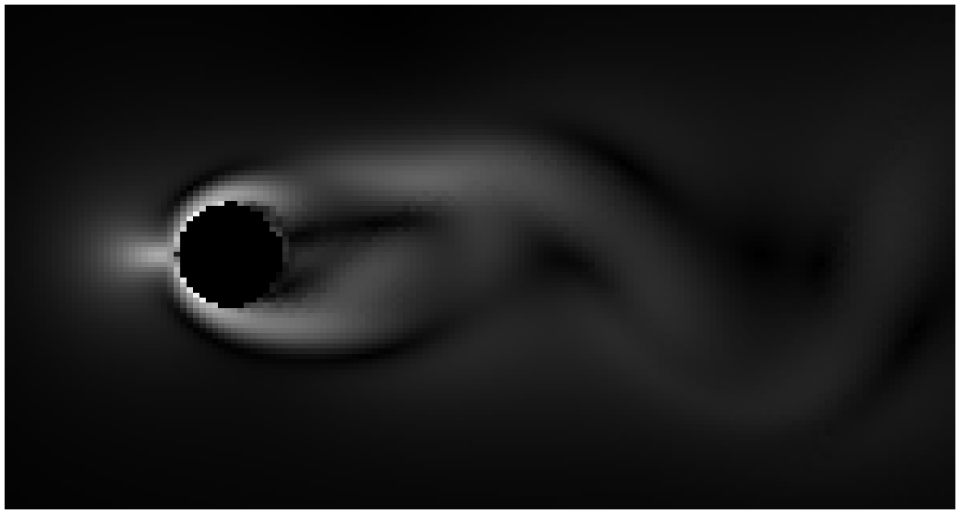

(b) Fast L-FTLE$^-$

Figure 4.8 Comparison of the basic and the accelerated implementation of the L-FTLE approach. The resolution is 150×100 with $T = 1$. Nearly no differences can be observed, only a few artifacts arise due to the nearest neighbor approach for interpolation to grid points.

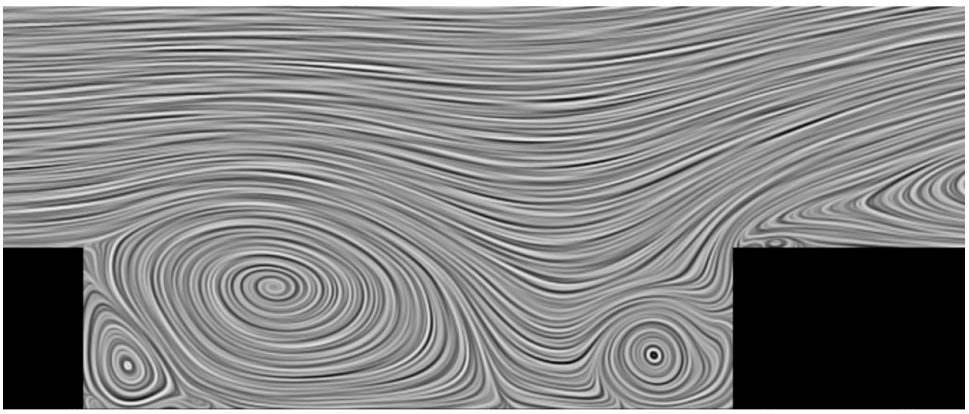

(a) Without noise

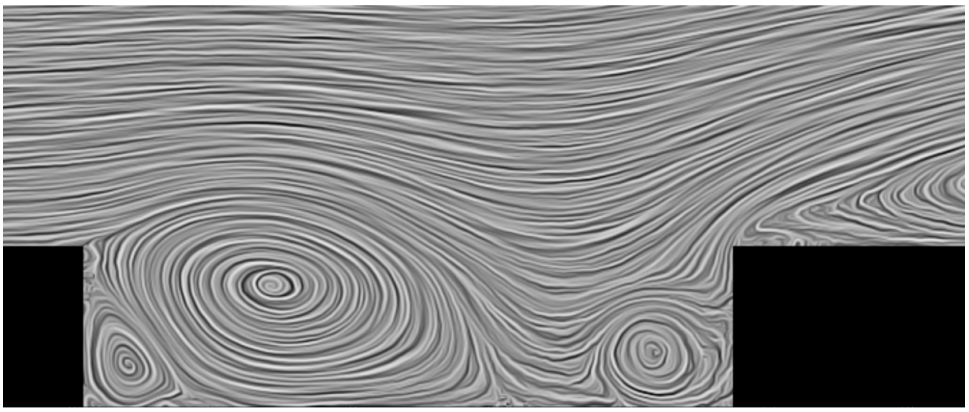

(b) With noise

Figure 4.9 The two images show one time slice of the cavity data set with and without noise. The noisy data set is generated by adding Gaussian noise to each vector component.

The L-FTLE approach needs only slightly more memory than the standard approach, since the intermediate values for one path line have to be saved, if the data set fits completely into the memory.

Noise. To analyze the sensitivity of the different approaches with respect to noise, we added Gaussian noise to the cavity data set. The noise is added to the two spatial components independently. We chose Gaussian noise, since it arises in the flow measurement using the PIV method [FCS04].

The influence of noise to the vector field is depicted in a time slice in Figure 4.9. The effect is apparent in areas of low velocity by highly curved streamlines in the LIC image. The macro structure of the velocity field is unaffected. The comparison matrix in Table 4.1 shows the impact of the noise to both

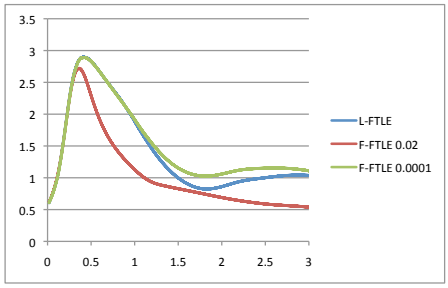

(a)

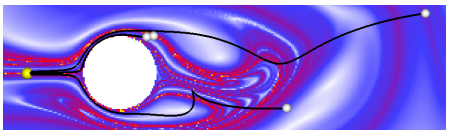

(b)

Figure 4.10 (a) Influence of the F-FTLE seeding distance to the separation. Depicted is the integration time T vs. separation for the start point depicted in (b). If the seeding distance for F-FTLE is chosen too large (1/50 of cylinder diameter), separation measure is not local. By decreasing the seeding distance to 1/10000, the separation converges towards the L-FTLE value. (b) Path lines of advected particles.

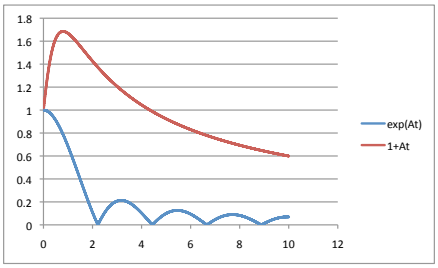

(a) $v(x, y) = (-2y, x)$

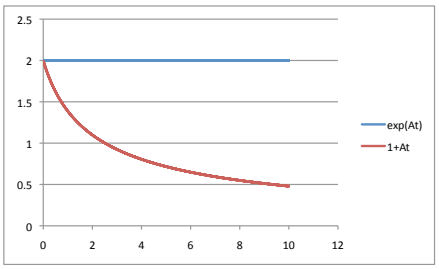

(b) $v(x, y) = (-x, y)$

Figure 4.11 L-FTLE$^+$ plotted against T for steady vector fields v. Sampling distance is equal to T, thus Equation (4.10) (red) and Equation (4.9) (blue) are only evaluated once for each value. The approximation diverges rapidly from the exact solution and is only valid for very small sampling distances.

approaches, respectively. As expected, F-FTLE and L-FTLE are both affected by the addition of noise. While for both methods the most prominent separation features are still visible, the introduced structures exhibit different characteristics, c.f. Table 4.1 H and K. While F-FTLE introduces many ridge-like structures, L-FTLE patterns are smoother with weaker structure.

4.2.4 Discussion

The structures resulting from L-FTLE are in many aspects very similar to the structures obtained with F-FTLE. The new definition of L-FTLE is not dependent on a sampling density parameter and does not need re-normalization steps during path line integration, as needed for the commonly used F-FLTE definition. In F-FTLE, the sampling density parameter can have a large influence to the separation measure as exemplified in Figure 4.10. The separation measure of L-FTLE is local by construction and not dependent on such a parameter.

Despite the different approach to compute the separation for a flow field, the new algorithm shows the same resulting structures as the standard approach. The L-FTLE approach computes a separation value with only one path line. For the standard algorithm, at least four path lines have to be traced. Thus, for a given number of path lines the new algorithm leads to a better resolution in the resulting field. Moreover, the seeding distance δ_x of the path lines is a parameter of the standard FTLE algorithm, which is not needed L-FTLE. Since L-FTLE incorporates the separation on the whole path line, the separation and later merging of particles within the interval T can be detected by the algorithm. As the particles merge on the path line, F-FTLE is insensitive regarding this behavior.

Images computed with the fast L-FTLE algorithm show nearly the same structures as those computed with the basic algorithm. Only a few artifacts arise due to the nearest neighbor interpolation for mapping to grid points. The resulting values are therefore not wrong, but only mapped to a slightly wrong position. The average acceleration factor of 8 outweighs this slight incorrectness.

As seen in the results section, the dependency of the L-FTLE approach on the sampling parameter Δt is not critical. Even if with a coarse sampling, the results are still good. The sampling parameter Δt influences also the evaluation of Equation (4.9) or its approximation in Equation (4.10). A comparison of the impact of the approximation is depicted in Figure 4.11. In the diagrams, L-FTLE$^+$ is plotted against the integration time T. Sampling distances are set to $\Delta t = T$, such that the exponential is evaluated only once. The approximation of Equation (4.10) diverges rapidly in first order from the correct separation values using Equation (4.9). Thus, in all the presented examples, Equation (4.9) was chosen. The parameter T shows the expected effects on the results.

The analysis of the standard and the new approach regarding noise sensitivity shows, that the macro structures are still visible both approaches, but tiny structures vanish or cannot be distinguished from the noise. The flow map approach shows fine blurry line-like structures that cannot be distinguished from tiny FTLE features. The structures altogether are much more blurry than in the non-noisy data. In contrast, the localized approach shows more block-like structures that differ from typical features of the separation field. Thus, the user can distinguish between noise artifacts and real structures.

4.3 Analysis of FTLE

In Section 4.1, we have seen that LCSs are sometimes characterized by material lines. To yield proper material lines, it is typically stated that the integration time T of the FTLE has to be increased. It is assumed that longer integration times capture more of the time-dependent motion and neglect the instantaneous motion. Thereby the snapshot flow behavior is considered to not showing the correct flow behavior, e.g., standard vector field topology is not applicable to time-dependent flows. In this section, we want to analyze, if this assumption is correct. The motivating questions are: 1. What does the FTLE actually show? 2. Do longer integration times yield more accurate results? 3. How far is the FTLE applicable to complex time-dependent flow behavior?

To answer these question, we apply the FTLE to an analytic example, i.e., a data set of Stuart vortices, a simple flow configuration, i.e., the flow behind a circular cylinder, and a complex flow, i.e., a semi-turbulent jet.

Note that we use the L-FTLE approach as presented in the last section in the remainder. However, we did the same computations with F-FTLE and the results were visually comparable.

Averaged stretching. L-FTLE considers the deformation of the neighborhood of a particle over a finite time T. In addition to this measure, we are also interested in the averaged separation a particle experiences, independent from its direction. This corresponds to the average of the instantaneous maximum separation. In the discretized version, we therefore use the L-FTLE computed only for one time step Δt and define

$$\mathcal{S}_{\Delta t}(\mathbf{x}, t) = \frac{1}{\Delta t} \ln \left(|| \exp(\mathbf{J}_{\mathbf{v}}(\mathbf{x}, t)\Delta t)) \, ||_{\lambda} \right). \tag{4.11}$$

This measure is averaged along the path line for a finite time interval $T = \Delta t \cdot N$

$$\mathcal{I}_T(\mathbf{x}_0, t_0) = \frac{1}{T} \sum_{k=0}^{N} \mathcal{S}_{\Delta t}(\mathbf{p}(\mathbf{x}_0, t_0, k\Delta t), t_0 + k \cdot \Delta t) \cdot \Delta t. \tag{4.12}$$

We call this new measure *averaged stretching*.

4.3.1 Stuart vortices

The Stuart vortex is an analytical, periodic vortex model, cf. Appendix A.2. We use a dataset resulting from a sampling to a regular grid.

To analyze the dataset, we computed the forward L-FTLE for different integration times T, see Figure 4.12. Red indicates high FTLE values and white low values. The blue regions indicate areas, where the FTLE cannot be computed due to the dataset boundary. As expected, the increasing integration

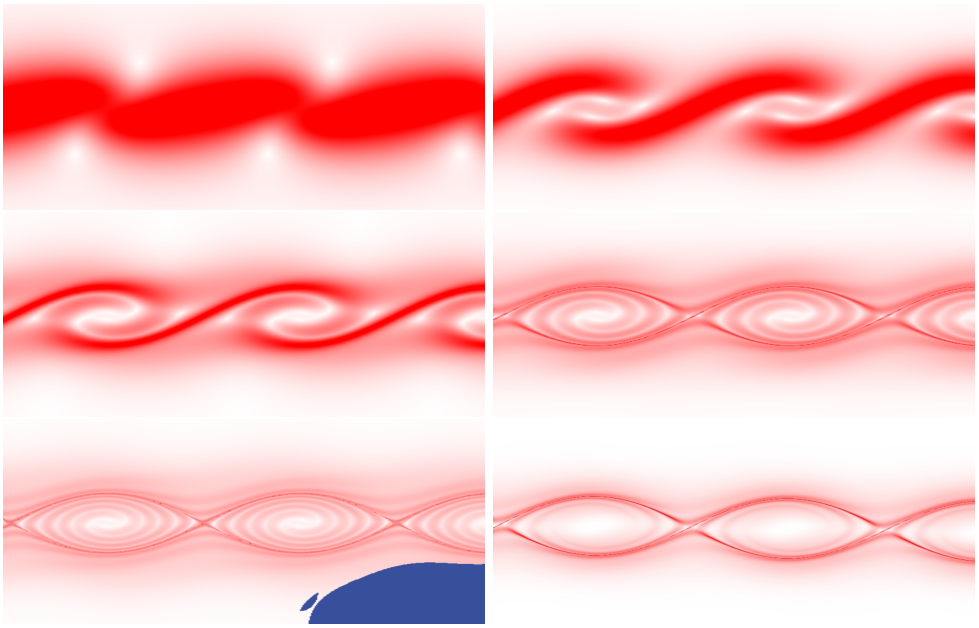

Figure 4.12 Forward L-FTLE of the Stuart vortex dataset for $T = 1, 2, 5, 10,$ and 15, where one period corresponds to $T = \pi$ (from left top to bottom right). The image bottom right is the result of averaging the images for $T = 10, 11,$ and 12. The colormap is the same for all images – white color corresponds to low and red to high FTLE values. With the increasing integration time the features become more crisp and detailed, partially resulting from an structure advection along trajectories.

time leads to more and crisper details in the visualization. The elliptical Stuart vortices are clearly highlighted.

Besides, one can make following observations: After a few periods a stable ridge bounding the vortices is emerging. This matches the statement by Green et al. [GRH07] that the location of the ridge indicating the boundary of the vortex does not change with increasing time. In contrast, the inner regions become clearer and sharper, but also change in position and frequency. The location of these FTLE-ridges depends on the integration time and does not converge for increasing integration time T. The high FTLE values result from 'separation events' far away in spatiotemporal domain, which are advected with the flow. The significance of such features for flow analysis is not clear and should not be interpreted as LCS.

In order to filter out the stable ridges, representing LCS, we propose to average the FTLE fields belonging to different integration times. The result for an average of integration times $T = 10, 11,$ and 12 is shown at the bottom right of Figure 4.12. The high FTLE values within the vortex vanish and the region boundaries stay visible.

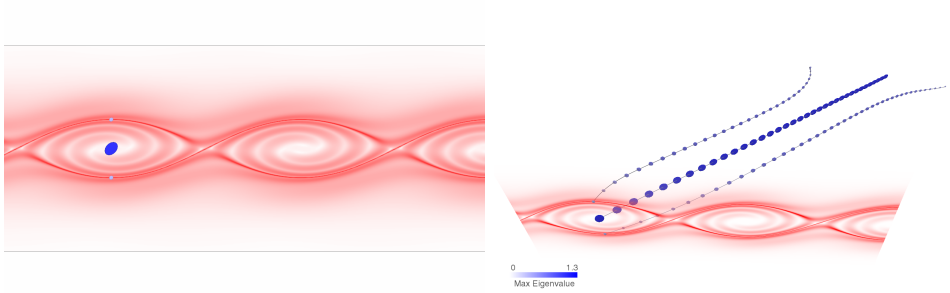

Figure 4.13 Analysis of the local separation along three path lines. The colormap is the same as in Figure 4.12. The local separation is depicted by glyphs deformed by the Jacobian matrix. While the FTLE value is high in the outer regions and low in the center, the local separation shows strong values along the center path line and lower values along the outer path lines.

Next, we focus on the white regions in the center of the vortices indicating no separation. Here, the FTLE value changes from red (high separation) for small T to white (low separation) after a few integration periods. In the center, the locally strong separation vanishes. To understand this behavior, we have seeded three path lines, one in the vortex center and two on the vortex boundary on the FTLE ridge. Along the path line, the instantaneous deformation induced by the Jacobian $\exp(\mathbf{J}_\mathbf{v}(\mathbf{x}, t)\Delta t)$ is visualized using glyphs, see Figure 4.13. In the left figure, the seeding points are displayed including the first glyph. The right image shows the path lines and the glyphs in a three-dimensional visualization, where time is used as third dimension. The integration time for the FTLE and the path lines is $T = 10$, which corresponds to approximately three periods of the dataset. The color of the glyphs is determined by the maximum local separation as defined in Equation (4.11). Blue represents high and white low values. It can be seen that the path line in the center exhibits a constantly high local separation, which is always higher than the local separation along the other two path lines. Moreover, the separation points always in the same direction on the center path line. Thus, it might be surprising at first sight that the FTLE value vanishes. Closer inspection shows that this results from the rotational part of the Jacobian, which is not visualized in this representation. Keeping this in mind, it cannot be concluded that low FTLE values mean that the particle does not experience high separation. FTLE shows a combination of both flow components – rotation and stretch.

A feature identifier that measures the local separation a particle experiences has been introduced by Equation (4.12). Figure 4.14 displays the result for integration times of $T = 1, 5, 10,$ and15. Red marks high and white low average separation. Again blue regions represent seedings where the path lines left the domain. These visualizations illustrate that the average separation is high in the entire vortex region with maximal values in the center and at the boundary

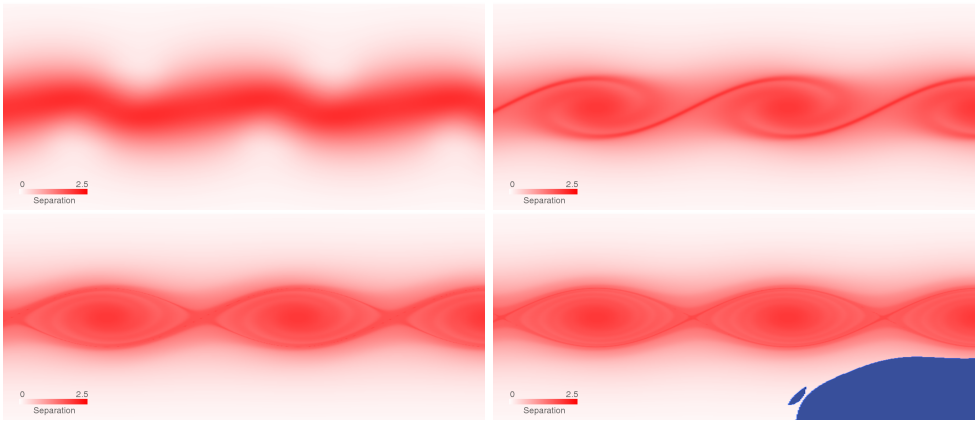

Figure 4.14 Forward averaged stretching values of the Stuart vortex dataset for $T = 1, 5, 10$ and 15 (from left top to bottom right). With increasing integration times, the separation in the vortex centers does not vanish in contrast to the values of the L-FTLE measure.

of the vortices. The averaged separation value converges towards its final value after a few time periods.

To put it in a nutshell, we can make the following observations when analyzing this dataset:

1. The locations of FTLE ridges do not necessarily indicate boundaries of LCS. One has to distinguish two kinds of structures. First, there are structures that stabilize after some integration periods. The corresponding path lines experience periodic 'separation events' and represent the actual boundaries of LCS. Second, there are structures with no definite position, where one 'separation event' is transported along path lines. It is to expect that for an integration time approaching infinity, it will become arbitrary dense and will fade out.

2. Low FTLE values do not necessarily mean that there is no separation along the path line. Therefore, it is meaningful to analyze the local separation in addition to FTLE.

4.3.2 Cylinder dataset

The second data set analyzed is the flow behind a circular cylinder, cf. Appendix A.4.

To analyze the contribution of the advection of separation to the final FTLE image, we compare the FTLE results, see Figure 4.16, with a simple visualization using dye-advection, see Figure 4.15. The dye is injected into the time-dependent flow in front of the cylinder. Advection results in a streak line visualization with very similar patterns to backwards FTLE. Thus, if lo-

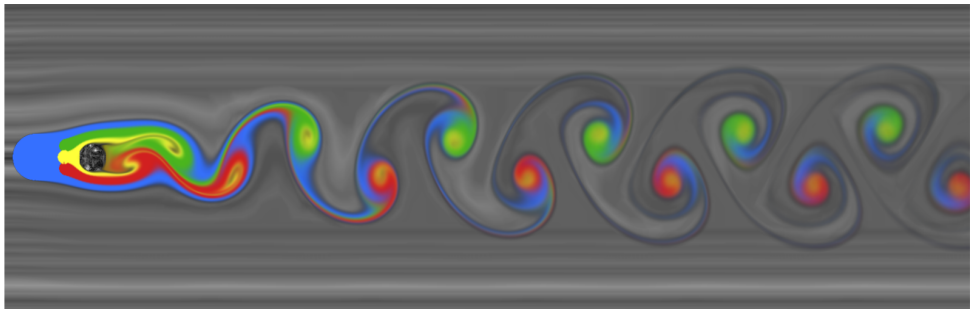

Figure 4.15 Visualization of time-dependent dye-advection combined with image-based flow visualization. The dye is advected along streaklines. The typical pattern of backward FTLE can be recognized in the advected dye.

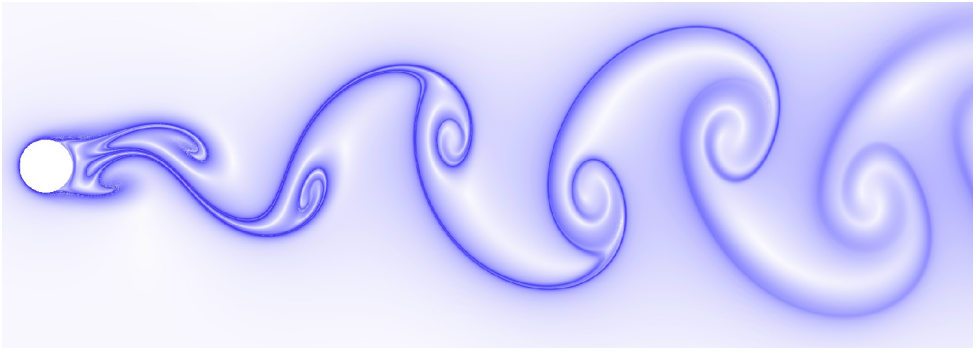

Figure 4.16 L-FTLE computed for the cylinder dataset computed for two shedding periods. White color corresponds to low and blue to high FTLE values.

cal separation takes place constantly at one position – as it is the case for this dataset at the cylinder, FTLE mainly transports this high separation values just as streak lines transport the stationary dye. The apparent feature originates mainly from the local separation at the cylinder.

4.3.3 Turbulent jet

The last data set is a complex flow configuration, cf. Appendix A.8, of a jet. It consists of 6000 time steps – we used steps $5000 - 5500$ for our computation, which corresponds to a temporal interval of length 50. From this dataset, the center slices are extracted resulting in a two-dimensional unsteady dataset. In Figure 4.17, the forward and backward FTLE computed in the unsteady two-dimensional dataset for a length of $T = 5$ are displayed.

The discovery of the existence of large-scale structures, so-called coherent structures, superimposing a chaotic background-flow was a big breakthrough in turbulent flow research. Under this perspective, it is interesting to have a look

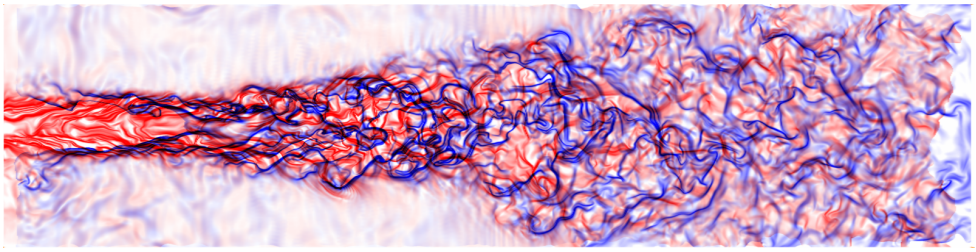

Figure 4.17 Forward (red) and backward (blue) FTLE for the two-dimensional time-dependent dataset of a jet for the integration time $T = 5$. The colormap was introduced by Garth et al. [GGTH07].

at how well FTLE copes with turbulent data. Figure 4.17 shows the forward and backward FTLE structures extracted from the jet dataset. There is a vast amount of structures visible, in particular multiple crossings of forward and backward FTLE. Even though the explicit physical interpretation of this slicing is not clear, it is sufficient to demonstrate the complexity of the emerging structures, which we leave without interpretation at this point.

4.3.4 Discussion

In the analysis, we experienced that the FTLE does not always behave as it was expected at first sight. However, the FTLE field and its extremal structures can be considered as one successful realization of LCSs. It highlights interesting flow structures in many applications. But one should also be aware that, even in non-turbulent flow fields, there are structures that cannot be represented by FTLE. It is important to interpret the results carefully to avoid misconceptions. There are also examples where similar features can be obtained with much simpler, less computationally expensive methods. As Example 4.3.2 shows, there can be a close connection to streak lines. In addition, increasing integration time does not always improve the results. Regarding complex flow configurations, the FTLE does not always yield the coarse structures of a flow configuration. There is not yet a satisfying interpretation of FTLE ridges for complex and especially for non-periodic data sets.

Finally, we conclude that FTLE is *one* realization of LCSs but does not cover all aspects of LCSs. There are still problems with the amount of structures. The interpretation is not always simple. To approach these problems, we therefore introduce another feature concept based on the acceleration in the next chapter.

Chapter 5

Flow analysis based on the particle acceleration

In the last chapter, we encountered problems using FTLE to extract features of time-dependent flow fields. First, the interpretation is not always clear. Especially, for complex flow fields, the physical meaning of the resulting structures can be questionable. Second, the density of the features complicates the analysis of complex flow fields. Third, FTLE is a concept for distinguished material *lines* of two-dimensional flows. On the contrary, for instance, a vortex core is a point structure in these flows. Thus, the FTLE reveals such structures at most only implicitly.

In this chapter, a new feature concept based on the material acceleration of a flow field is introduced in Section 5.1. For these structures, the physical interpretation is much simpler. The feature extraction is based on scalar field topology. To deal with feature-rich flow fields, a hierarchy of the features based on an importance measure is proposed. The first component of this measure is the lifetime resulting in the extraction of the long-living features as discussed in Section 5.2. In Section 5.3, it is shown how robust tools can be employed to extract vortex core lines based on the acceleration. This enables us to deal with complex flow fields. In addition, the feature hierarchy based on the lifetime is extended by a spatial feature importance measure. In Section 5.4, it is demonstrated that the associated vortex regions can be extracted in the same topological setting. Last, in Section 5.5, the resulting features are analyzed.

5.1 Lagrangian equilibrium points

In this section, a new set of feature points for time-dependent flow fields is introduced. First, we will determine requirements for the new feature identifier, cf. Section 5.1.1. Afterwards, we will show that the minima of the acceleration magnitude fulfill these specification, cf. Section 5.1.2. The relation to vortices

of the newly defined features is given, cf. Section 5.1.3, and their meaning in two dimensions is reconsidered, cf. Section 5.1.4. Additionally, the definition is evaluated using selected analytic illustrating examples, cf. Section 5.1.5.

5.1.1 Requirements

In the following, we will deduce three requirements for the new feature definition. We will thereby focus on the successful concept of standard vector field topology, cf. Section 2.1.4. Topological analysis of velocity fields has been successfully applied for examination of flow fields with a distinguished frame of reference. However, its applicability to general flow fields is limited. The location of the velocity zeros as feature points depends on the chosen frame of reference – even the existence of a velocity zero depends on the frame of reference. We therefore want to find an alternative feature concept, which generalizes the snapshot topology in a local sense and overcomes the abovementioned limitations.

R1 – Correspondence to velocity field topology. The concept of standard vector field topology or velocity field topology, respectively, is successful for steady flow fields. Thereby, we consider a vector field as steady, if there is a distinguished frame of reference for which the vector field is stationary, i.e., it does not change in time. These flow fields consist of *frozen* convective structures. They satisfy Taylor's hypothesis [Tay38]. If the flow field is steady, we examine its velocity field in exact this distinguished frame of reference. For incompressible steady flows, the velocity field then shows the exact position of centers, which correspond to vortex cores, and saddles. This concept is not applicable to unsteady flow fields, since there is no such distinguished frame of reference. Anyhow, we want our new feature definition to coincide with velocity field topology for steady flow fields. In addition to the set of feature points that should be the same, we require that the classification of the points is preserved. Note that this contradicts Haller's definition of an objective vortex [Hal05]. In his paper, the features have to be invariant under rotational transformation. Thereby, saddles become centers and vice versa; thus, their classification is changed.

R2 – Galilean invariance. A Galilean invariant feature identifier reveals the same structures when changing the frame of reference. For general time varying flows, the feature points are invariant under the change of the frame of reference. Thus, Galilean invariance is a desired property.

In the following, we will have a closer look on the meaning of a Galilean transformation for the purpose of getting a better understanding of Galilean invariance and frames of references. Let $\mathbf{v}(\mathbf{x}, t)$ be a time-dependent vector field on a finite spatial domain $D \subset \mathbb{R}^2$ with a single convecting center from

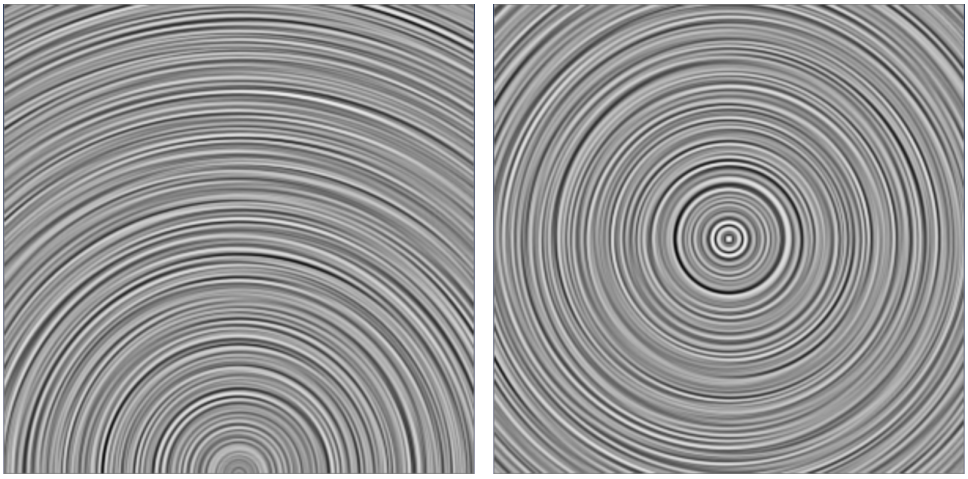

(a) Convecting center (b) Distinguished frame of reference

Figure 5.1 A convective center in the original (a) and transformed (b) frame of reference. By choosing an appropriate Galilean transformation, the actual flow behavior of the center is revealed.

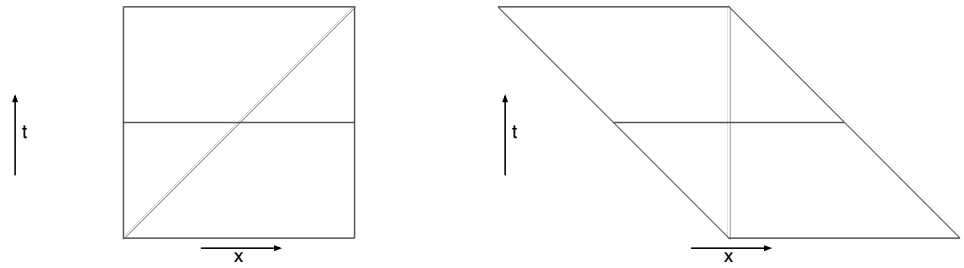

(a) Original frame of reference (b) Sheared frame of reference

Figure 5.2 Considering time as an additional dimension helps to understand Galilean invariance. In fact, a Galilean transformation corresponds to a shear of the temporal dimension. On the left side, the bounding box in the frame of reference of the convective center of Figure 5.1 (a) is shown. On the right side, a shear in time results in a stationary data set. The white line represents the vortex core line in time.

left to right. The fixed point of the center lies on the x-axis. The instantaneous velocity field is shown in Figure 5.1 (a). Fortunately, this flow field has a distinguished frame of reference for which the velocity field is stationary. The frame of reference just has to move with the center itself – a Galilean transformation. The corresponding velocity field is shown in Figure 5.1 (b). While the flow behavior itself was not changed by the transformation, the visual output has changed.

The effect is easier to understand if we consider the time of the flow field as

a third dimension. In Figure 5.2 (a), the core line of the center is shown in the original frame of reference. If we now change the frame of reference to get the output of Figure 5.1 (b), this corresponds to a shear of the temporal domain, see Figure 5.2 (b). The new frame of reference moves with the center. The spatial origin therefore shifts outside the finite domain D. This interpretation of a Galilean transformation shows why the flow behavior stays the same, while the visual output changes. Keep in mind that in this spatiotemporal representation of the two-dimensional time-dependent vector field each vector consists of three components $\mathbf{v} = (u, v, 1)$. Using the stream line field to visualize the flow, we only look at projections of these velocity vectors into the spatial domain. A Galilean transformation thereby changes this projection. Galilean invariance means that the feature identifier does not depend on this projection. Note that using this interpretation, it is immediately clear that the material derivative has to be Galilean invariant.

In the above example, we used an actually steady field to explain the impact of a Galilean transformation. On the other side, arbitrary time-dependent flow fields do not necessarily consist of structures with a common convective motion. Even more, each feature in the flow field might have its own motion, which is naturally influenced by the other structures. However, the above interpretation is still possible locally.

R3 – Lagrangian viewpoint. To guarantee a physically sensible feature identifier, we want to focus on particle motion. We therefore require that our feature definition incorporates a Lagrangian viewpoint on the flow.

5.1.2 Definition

In the last section, we defined three requirements for our new feature identifier: (i) correspondence to velocity field topology, (ii) Galilean invariance and (iii) Lagrangian viewpoint. The definition of the feature identifier has to be done using a Eulerian viewpoint. As already stated in Section 2.3, the material derivative links the Lagrangian to the Eulerian viewpoint. In addition, it was also shown that quantities based on the material derivative are Galilean invariant. The need to have similar features as vector field topology suggests that we should use the material derivative of the flow field itself. This quantity is called the material acceleration;

$$\mathbf{a}(\mathbf{x}, t) = \frac{Dv}{Dt}(\mathbf{x}, t) = \frac{\partial v}{\partial t}(\mathbf{x}, t) + (\mathbf{v}(\mathbf{x}, t) \cdot \nabla)\mathbf{v}(\mathbf{x}, t). \tag{5.1}$$

We now define that a minimum of the magnitude of the material acceleration $\|\mathbf{a}\|$ is called *Lagrangian equilibrium point* (LEP). This point can be classified on the basis of the Jacobian of the velocity field, $\nabla\mathbf{v}$. An LEP is called *saddle-like* if its eigenvalues are real and *center-like* if its eigenvalues are complex.

In the following, it is shown that this definition satisfies requirement R1. Let $\mathbf{x}_0$ be a zero of the stationary velocity field

$$\mathbf{v}(\mathbf{x}_0) \equiv 0. \tag{5.2}$$

This implies that the material acceleration

$$\mathbf{a}|_{\mathbf{x}_0} = (\partial_t \mathbf{v} + \mathbf{v} \cdot \nabla \mathbf{v})\,|_{\mathbf{x}_0} = 0 \tag{5.3}$$

vanishes at $\mathbf{x}_0$. Summarizing, LEPs as minima of the acceleration magnitude are a superset of acceleration zeros and these zeros are a superset of the critical points of the velocity field. Hence, LEPs can be considered a generalization of the critical points of the velocity fields. In addition, these points can exhibit vortex- as well as saddle-like behavior, depending on the eigenvalues of the velocity Jacobian.

5.1.3 Interpretation as a vortex indicator

Another perspective onto the acceleration minima is given by their relation to the pressure gradient via the incompressible Navier-Stokes equation:

$$\begin{aligned} \mathbf{a}(\mathbf{x},t) &= -\frac{1}{\rho_0}\,\nabla p(\mathbf{x},t) + \nu\,\Delta \mathbf{v}(\mathbf{x},t), \\ \operatorname{div} \mathbf{v}(\mathbf{x},t) &= 0, \end{aligned} \tag{5.4}$$

where p is the pressure of the flow field, ρ_0 and ν are the density and kinematic viscosity of the fluid, respectively, and Δ is the spatial Laplacian operator, cf. Section 2.3.1. For ideal flows, the equations reduce to the Euler equation:

$$\begin{aligned} \mathbf{a}(\mathbf{x},t) &= -\frac{1}{\rho_0}\,\nabla p(\mathbf{x},t), \\ \operatorname{div} \mathbf{v}(\mathbf{x},t) &= 0. \end{aligned} \tag{5.5}$$

Then, local extrema of the pressure field, which are zero points of the pressure gradient coincide with zeros of the acceleration field. In this case, the above defined LEPs form a superset of local extrema of the pressure field. Since pressure minima are often associated with vortices, the LEP are also be related to these structures.

5.1.4 Considerations in two dimensions

For steady flow fields, we have seen that the features corresponding to the critical points of vector field topology are zeros of the acceleration. We defined our features of interest as minima of the acceleration magnitude. We therefore choose to use scalar field topology instead of vector field topology. In addition, our definition encompasses a wider range of features – including the zeros. We

made our choice due to the following reasons: (i) Minima of the acceleration magnitude represent distinguished structures in the flow field. They reveal an equilibrium of the particle motion. (ii) We are confident that the minima or minima lines of the acceleration magnitude in a three dimensional field have similar properties as discussed for two-dimensional fields in this chapter. The definition of the LEPs can therefore be transferred. (iii) Defining features as minima of a certain quantity eases an extraction of the structures since robust methods for the extraction of scalar field topology can be utilized. The robust extraction of zeros in the context of vector field topology is much more complicated. (iv) The magnitude of the acceleration reveals more interesting structures. For instance, we will see that vortex regions can be defined in the context of the acceleration magnitude.

Note that Goto et al. [GV06] have independently chosen to define their feature points as zeros of the acceleration. Actually, we will often deal with minima of the acceleration magnitude that are zeros in the examples shown in this chapter. This is illustrated by the following example. Imagine a moving vortex that changes direction and speed. This vortex is therefore accelerated. Its region of influence can be characterized by centripetal acceleration which induces the rotational flow behavior. In two dimensional flows, the center of the centripetal acceleration has to be a critical point in the acceleration vector field. Its magnitude is therefore zero. Note that the this consideration does also not hold in three dimensions. Furthermore, a vortex may not always be characterized by centripetal acceleration. There might be structures that one would define as vortices that do not have zero acceleration within their region of influence, but a minimum in the acceleration magnitude.

In a nutshell, the definition of the LEPs as minima of the acceleration magnitude is a concept that is transferrable to three dimensions. In the context of scalar field topology, more interesting information about the acceleration is revealed. For complex data set, the utilization of scalar field topology makes the extraction of the LEPs possible in the first place.

5.1.5 Analytic illustrating examples

In this section, two two-dimensional incompressible flows are considered: the Stuart solution of the inviscid mixing layer and the Oseen vortex pair. These analytical examples illustrate that local minima of the total acceleration magnitude are sensible time-dependent counterparts of critical points of standard velocity field topology and good indicators of vortices and saddles.

Stuart solution of the mixing layer. The first data set considered is a simple version of a shear layer, cf. Appendix A.2.

First, we want to reconsider the effect of Galilean transformations. The Stuart vortices are depicted in Figure 5.3 as streamlines using planar line

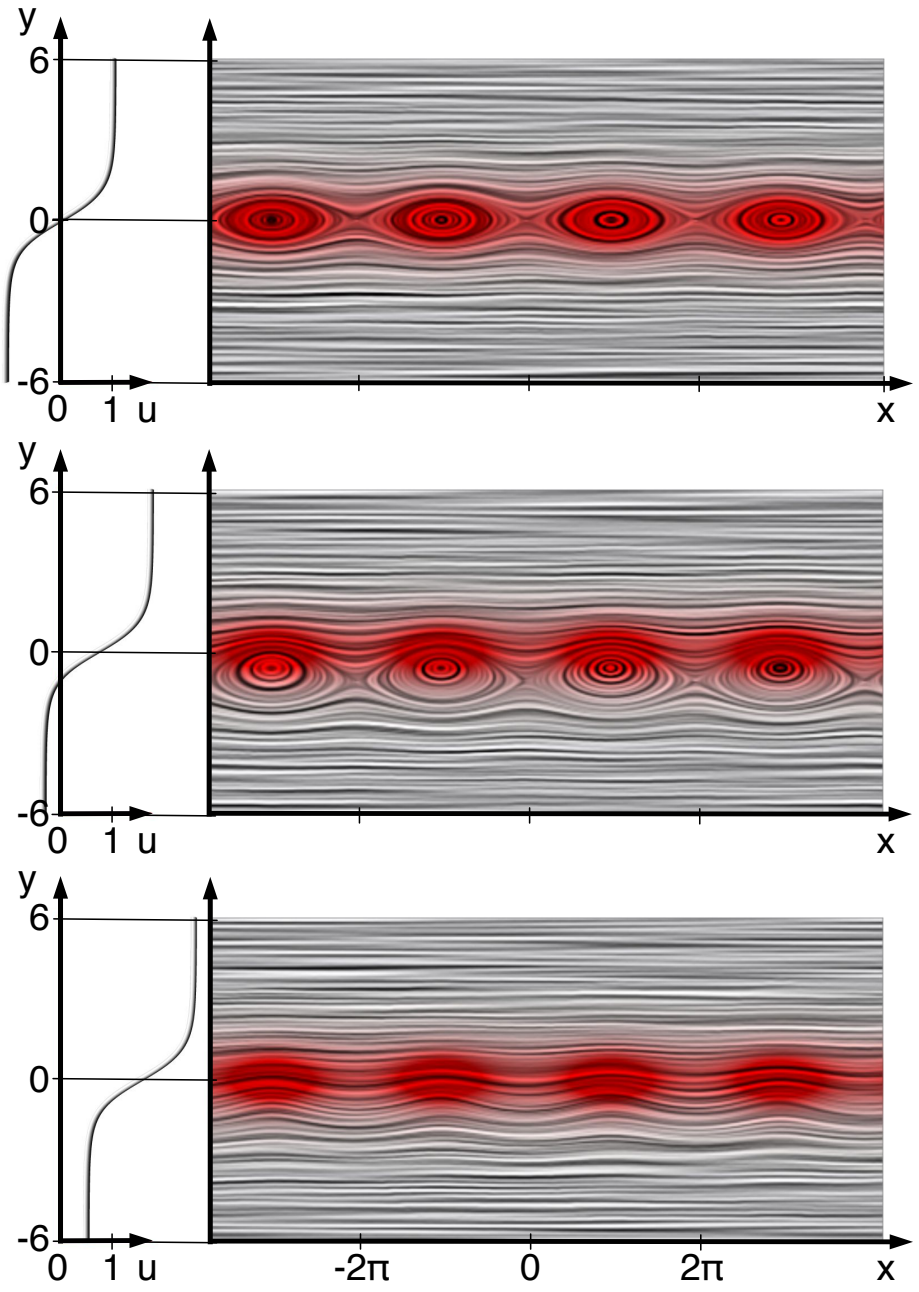

Figure 5.3 Stuart vortices in various convecting frames. The mean velocity profile is shown at the left. The Stuart vortices are indicated by visualizing the instantaneous velocity field using line integral convolution. The coloring is determined by vorticity; more intense red corresponds to higher vorticity.

integral convolution (LIC) [CL93, SH95]. The top picture shows the well-known cat eyes in a periodic sequence of centers (vortices) and saddles for a vortex-fixed frame of reference ($u_c = 0$). For this configuration, the flow field is stationary. The middle picture depicts the same structures but in a frame of reference moving to the left with the lower stream at velocity $(-0.7, 0)$, or, equivalently, the vortices moving to the right at $u_c = 0.7$. Thus, the data set is now time-dependent. The centers and saddles are displaced towards the slower stream. The bottom picture illustrates the same flow with a frame of reference moving at velocity $(-1.5, 0)$, i.e., $u_c = 1.5$. Now, no zeros are observed.

These pictures illustrate that velocity field topology strongly depends on the frame of reference as discussed above. In case of the Stuart solution, one might argue that the frame of reference convecting with the structures is the most natural one. However, the convection velocity of a jet and many other flows depend on the stream-wise position, i.e., generally no single natural frame of reference exists for topological considerations. In a nutshell, velocity field topology is not applicable to time-dependent flow fields.

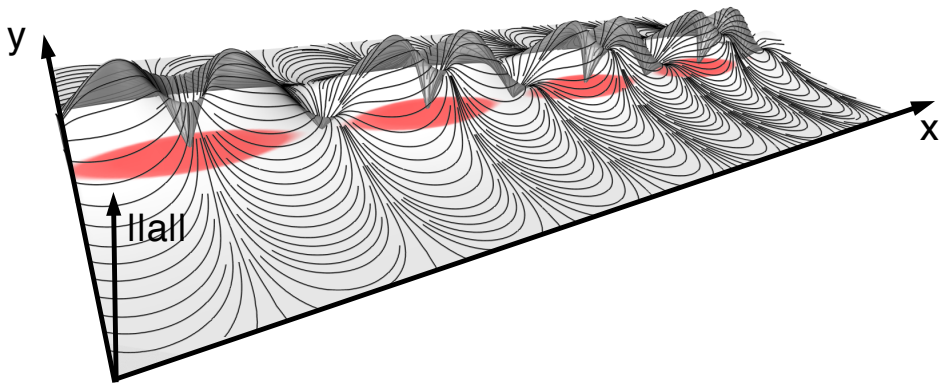

Figure 5.4 The acceleration field of convecting Stuart vortices. The coloring at the bottom is determined by the vorticity. The height field shows the acceleration magnitude and the curves represent integral lines of the acceleration vector field.

Figure 5.4 illustrates the acceleration field. In this image, it can be seen that the saddles and centers of a stationary Stuart solution are not only zeros of the velocity field but also zeros of the material acceleration field. Note that the zeros of the acceleration field and the local minima of the acceleration magnitude coincide in this example. In general, the latter quantity is a superset of the first. Furthermore, a subset of the minima of the acceleration magnitude also represents vortex cores as is verified by the vorticity magnitude depicted as red coloring at the bottom of Figure 5.4.

Oseen vortex pair. Now, we consider a pair of two co-rotating Oseen vortices, cf. Appendix A.1. In this example, r_c is chosen as 0.5 and Γ as 2π. The distance of the vortex to the center is chosen as $R = 1/\sqrt{2}$. The data set is instationary.

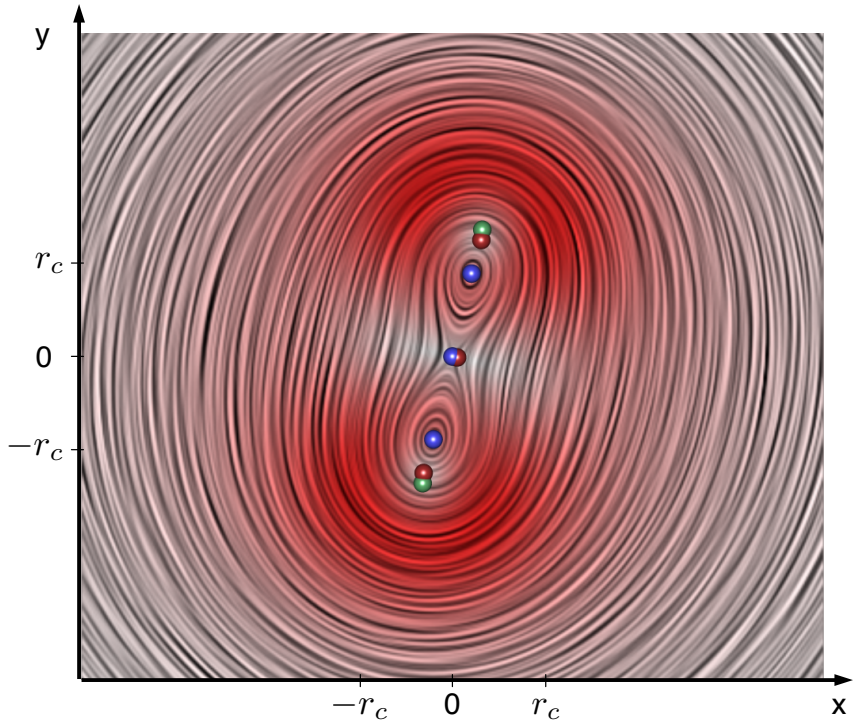

Figure 5.5 Depiction of two co-rotating Oseen vortices by their instantaneous streamlines using line integral convolution. The color-coding is determined by the acceleration magnitude; more intense red encodes higher values. The minima of the acceleration magnitude are marked by red spheres. For comparison, the critical points of standard velocity field topology (blue spheres) and the maxima of the vorticity (green spheres) are added.

Figure 5.5 illustrates the Oseen vortex pair. Here, the instantaneous streamlines can be inferred from the planar LIC. Blue circles mark the corresponding critical points of the velocity field. Regions of large acceleration are marked by red. The minima (zeros) of the acceleration field are denoted by red circles. It should be noted that the maxima of the vorticity (indicated by green circles) are much closer to the minima (zeros) of the acceleration than to the zeros of the velocities. Thus, the minima of the acceleration magnitude correspond more to the vortex cores than the velocity field topology does. This difference is insignificant for *frozen* vortices but increases with increasing angular rotation. Hence, the difference is correlated with the radial acceleration of the vortex motion. Only a non-inertial co-rotating frame of reference minimizes

the difference between vorticity maximum and the center of the velocity field. For the saddles, the critical point found by vector field topology still coincides with the minimum of the acceleration magnitude.

5.2 Long-living features

In this section, a method to extract long-living counterparts of critical points of velocity field topology is introduced. The features are based on the concept of LEPs.

5.2.1 Motivation

In real-world datasets, the high density of features often complicates a proper analysis. An appropriate filter mechanism differentiating between important and unimportant structures can ease this problem. Since fluid flow researchers are mainly interested in long-living structures, the lifetime of features is a meaningful filter criterion. In the following, special attention is paid to particles that carry the minimality property of $\|\mathbf{a}\|$ for at least a small period of time. The proposed feature extraction approach makes use of the 'feature lifetime' in two ways: (i) Considering and averaging the acceleration magnitude along path lines over a lifetime interval reinforces the Lagrangian perspective of the approach. (ii) An explicit *feature lifetime* filter selecting particles that stay in a feature state a certain time period enables the extraction of long-living features.

5.2.2 Feature extraction technique

As noted in Section 2.3.2, the center of a Lagrangian point of view is the behavior of particles, represented by path lines and the evolution of flow properties along these lines. Thereby, each path line is identified by its initial position $\mathbf{x}_0$ at time t_0 and the corresponding trajectory $\mathbf{p}(t, \mathbf{x}_0, t_0) = \mathbf{p}$ depending on the time parameter t.

In the following, we introduce a new approach to extract a feature $\mathcal{F}$ based on the observation of a scalar *feature identifier* $f(\mathbf{x}, t)$ along a path line $\mathbf{p}$. Therefore, the contribution of a path line to a certain feature is measured using a *feature importance* $I_{\mathcal{F}}$; it is defined as the average of the feature identifier over some feature time span $[t_{min}(\mathbf{x}_0, t_0), t_{max}(\mathbf{x}_0, t_0)]$

$$I_{\mathcal{F}}(\mathbf{x}_0, t_0) = \frac{1}{t_{max}(\mathbf{x}_0, t_0) - t_{min}(\mathbf{x}_0, t_0)} \int_{t_{min}(\mathbf{x}_0, t_0)}^{t_{max}(\mathbf{x}_0, t_0)} f\left(\mathbf{p}(t, \mathbf{x}_0, t_0), t\right)^2 dt. \tag{5.6}$$

The choice of the parameters $t_{max}(\mathbf{x}_0, t_0)$ and $t_{min}(\mathbf{x}_0, t_0)$ is crucial, since they describe the time range of influence to the local value. They are determined by the time a path line exhibits a certain feature state. Thus, they depend on the feature considered and are derived for each path line segment.

The *feature lifetime* is defined as

$$T_{\mathcal{F}}(\mathbf{x}_0, t_0) = t_{max}(\mathbf{x}_0, t_0) - t_{min}(\mathbf{x}_0, t_0). \tag{5.7}$$

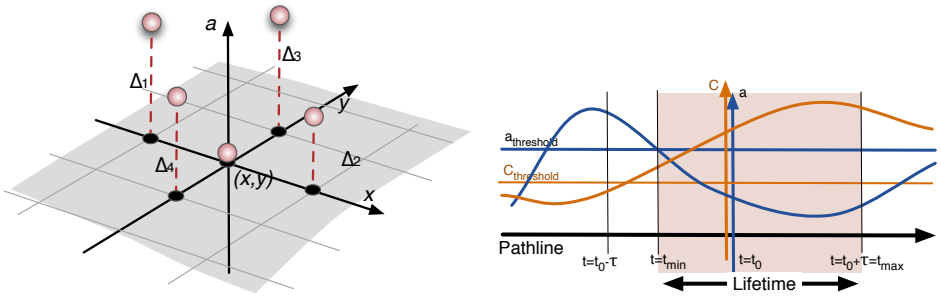

(a) (b)

Figure 5.6 (a) The minimality of the acceleration can be measured by the Laplacian of the scalar field $\|a\|$, which can be computed by central differences. (b) Definition of a feature's lifetime along a path line. The parameter t_{min} is determined by the acceleration threshold and t_{max} by the maximum lifetime window.

More specifically, for LEPs, the feature identifier is the acceleration magnitude $a(\mathbf{x},t) = \|\mathbf{a}(\mathbf{x},t)\|$. The lifetime parameters $t_{min}(\mathbf{x}_0,t_0)$ and $t_{max}(\mathbf{x}_0,t_0)$ are based on three quantities: acceleration magnitude a, a minimality measure of the acceleration C_a, and a maximum lifetime window τ. To measure the minimality the differences of $a(\mathbf{x}_0,t_0)$ at neighboring points are averaged in the four main directions: $C_\mathrm{a} = 1/4\sum_{i=1}^{4}\Delta_i$, where $\Delta_i, i = 1,..,4$ are defined in Figure 5.6(a). $C_\mathrm{a} > C_{threshold}$ indicates that a particle has low acceleration compared to its neighbors.

A maximum lifetime window $[t_0-\tau, t_0+\tau]$ restricts the values of t_{max} and t_{min}. Since saddle and vortex regions exhibit different characteristic behavior, the parameter τ can be chosen for each of these structures separately. In the following, the Jacobian matrix is used to distinguish between saddles and vortex-like features.

As described in Figure 5.6 (b), the lifetime parameters are defined as

$$\begin{aligned} t_{min}(\mathbf{x}_0,t_0) \quad = \quad & \min(t' \in [t_0-\tau, t_0] \mid \forall t \in \left[t', t_0\right] : \\ & a(\mathbf{p}(t,\mathbf{x}_0,t_0),t) \leq a_{threshold} \text{ and} \\ & C_\mathrm{a}(\mathbf{p}(t,\mathbf{x}_0,t_0),t_0) \geq C_{threshold}), \end{aligned} \tag{5.8}$$

and

$$\begin{aligned} t_{max}(\mathbf{x}_0,t_0) \quad = \quad & \max(t' \in [t_0, t_0+\tau] \mid \forall t \in \left[t_0, t'\right] : \\ & a(\mathbf{p}(t,\mathbf{x}_0,t_0),t) \leq a_{threshold} \text{ and} \\ & C_\mathrm{a}(\mathbf{p}(t,\mathbf{x}_0,t_0),t_0) \geq C_{threshold}). \end{aligned} \tag{5.9}$$

If one of the criteria is not fulfilled at particle position $\mathbf{x}_0$ and time t_0, the feature lifetime is defined as zero and $t_{max}(\mathbf{x}_0,t_0) = t_{min}(\mathbf{x}_0,t_0) = t_0$; furthermore, the acceleration is not averaged over the lifetime and the resulting importance value is set to the square of the local acceleration magnitude.

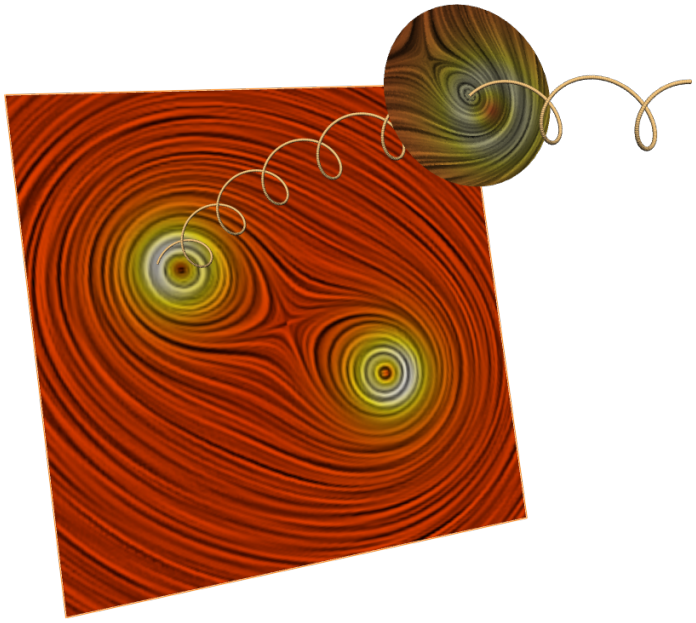

Figure 5.7 The path line of a particle seeded in one time-slice is displayed. The time is represented as third dimension. The relative behavior of the flow field in the neighborhood of this particle at a later point in time is displayed on a surrounding circular disk. The acceleration magnitude is color coded in the line integral convolution (LIC) images of the flow field.

Subsequently, feature candidates are extracted by searching minima in the resulting scalar importance field $I_{\mathcal{F}}$. Finally, a filtering with the extracted lifetime distinguishes important and unimportant features.

5.2.3 Implementation

The input to the algorithm is a 2D vector field defined on a sample grid. The algorithm consists of three main steps: integration of the acceleration values, extraction of the minimum points and filtering of these points with the lifetime.

Integration. The first step is the determination of the lifetime parameters, according to Equations (5.7), (5.8) and (5.9). A suitable threshold value for a is extracted by analyzing the acceleration characteristics of the first time-slice of the dataset. In the remainder of this section, it is simply set to ten percent of the maximum value. The threshold C_a has to be set a little above zero, to avoid setting a long lifetime for regions with low acceleration at all.

For each discrete point $(\mathbf{x}_0, t_0)$, a backward search in time on the trajectory $\mathbf{p}$ determines $t_{min}(\mathbf{x}_0, t_0)$. The lifetime criteria at each sample step on $\mathbf{p}$ is tested until either one of the thresholds is violated, or the maximum time window or the domain boundary is reached. Then, the feature importance is

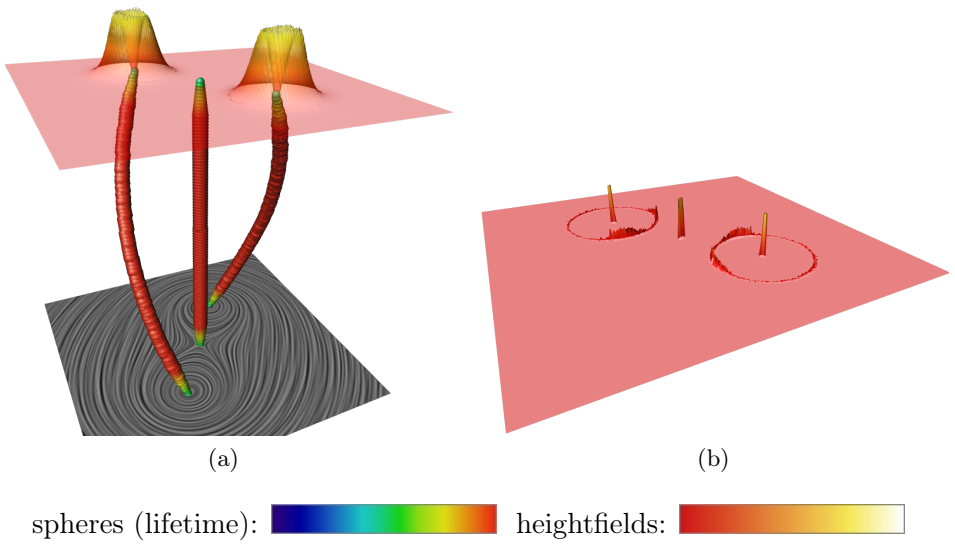

Figure 5.8 Illustration of the averaged LEP concept for two co-rotating Oseen vortices. The color-coded heightfield represents: (a) integrated acceleration, (b) and lifetime for the last time step.

computed according to Equation (5.6). For numerical integration, a Runge-Kutta integrator RK4(3) with adaptive step-size control is used. After the starting point t_{min} for the forward integration is found, the accumulation of the acceleration magnitude along $\mathbf{p}$ is started. The integration is terminated if one of the lifetime criteria is not fulfilled. Note that the integration is done at least until t_0 is passed. Then, the resulting values are normalized by the factor $1/T_{\mathcal{F}}(\mathbf{x}_0, t_0)$ and both lifetime $T_{\mathcal{F}}(\mathbf{x}_0, t_0)$ and importance measure $I_{\mathcal{F}}$ are stored as scalar fields.

Extraction. Feature candidates are extracted by searching local minima in the importance field I using a discrete neighbor analysis. Alternatively, other methods like the watershed transformation [Soi99] could be used for locating local minima.

Filtering. After these initial feature candidates are found, the lifetime filter is applied. Using a threshold for lifetime, it is now possible to emphasize long-living structures. The threshold can be chosen separately for saddles and centers to account for the different lifetime characteristics.

5.2.4 Visualization

All results in this paper are visualized in a volume spanned by two spatial coordinates and time. The extracted feature points are illustrated using spheres.

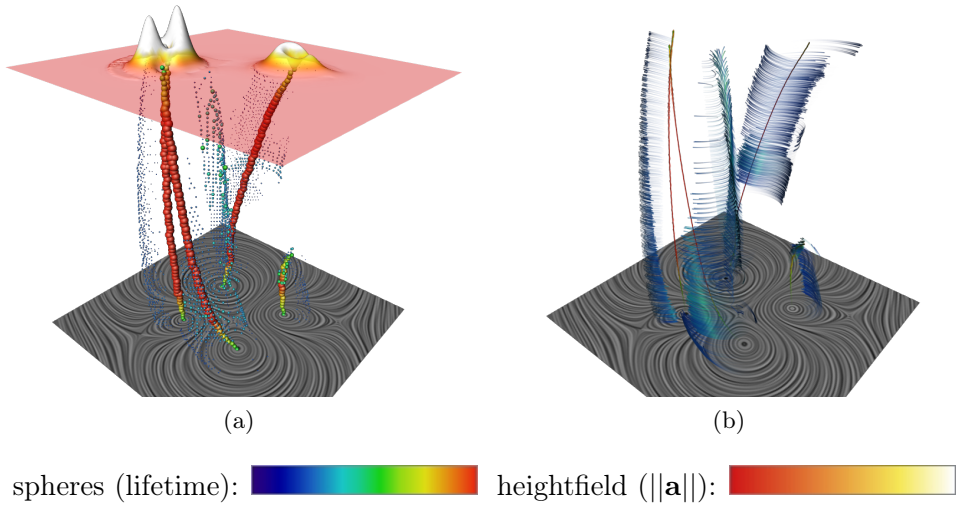

Figure 5.9 (a) Extraction of features for a motion of six Oseen vortices. Since particles leave the saddles regions quickly, the saddles do not emerge as prominently as the vortex cores. The integration windows of 0.3 in each direction are too large for particles passing through the saddle in the center. In comparison, all other long-living structures such as the vortex cores are extracted effectively. The height field represents the integrated acceleration. (b) Visualization of the feature lifetime. The illuminated path line segments show the interval of the lifetime used for the integration of the acceleration. Path lines seeded in vortex-like feature points are long centerlines, while path lines seeded in saddle-like feature points diverge rapidly.

The spheres are scaled and colored according to the associated lifetime, choosing a color table where high lifetime values are marked red, see Figure 5.8 and Figure 5.9 (a). In some images, illuminated path line segments are seeded in the extracted feature points to get a more intuitive notion of the lifetime. The path lines are terminated after exceeding their feature lifetime, as shown in Figure 5.9 (b). Color-coding is the same as for the spheres. The scalar fields used for the feature extraction can be added as height field for one time step.

To understand the local flow structure, it is helpful to observe not only single path lines but also the behavior of bundles. Such an exploratory analysis is facilitated by the possibility to select a point of interest in the LIC image. For this location, the path line is displayed together with a moving disk representing the flow relative to this path line, see Figure 5.7.

5.2.5 Results

To evaluate its effectiveness, the proposed method has been applied to two different datasets. The first dataset represents a pair of co-rotating Oseen vortices, cf. Appendix A.1, similar to the one used in the last section. Note

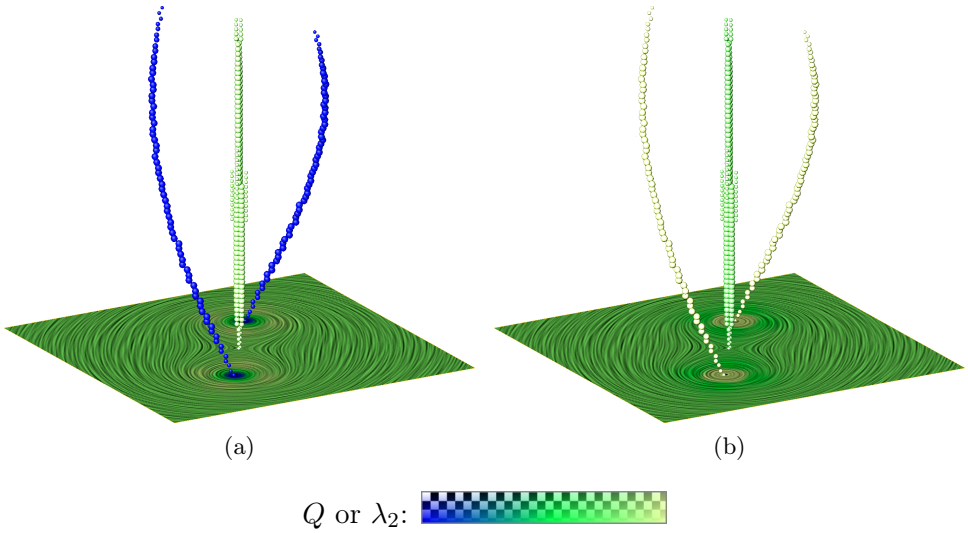

Figure 5.10 Comparison of (a) λ_2 and (b) Q with the proposed Lagrangian equilibrium points. The extracted feature points include the vortex cores marked by high values of Q or low values of λ_2. In addition the saddle between the two vortices is detected.

that for this data set, the parameter r_c was set to 0.25. This moves the minima of the acceleration magnitude towards the critical points of the velocity field topology. A more complex flow field is generated by the interplay of six moving Oseen vortices, cf. Appendix A.1. Both datasets are given for a temporal bounding box of $[-1.0, 1.0]$. The maximum lifetime window τ for integration is set to 0.3 in each direction. The extraction process takes a couple of minutes on standard hardware using non-optimized software.

For both datasets, it can be seen in Figure 5.8 (a) and Figure 5.9 (a) that the integrated acceleration is low at vortex centers and saddle points. While the lifetime is high for all features of interest in the co-rotating case, the lifetime only marks centers clearly in the complex field. The structures extracted are displayed as spheres, using the lifetime to define color and size. Due to the finite time window, the lifetime is low at the beginning, grows and then drops off to the end.

After applying the lifetime filter, vortices are marked as important, but interesting saddles are also removed. This is a consequence of the fact that particles stay longer in the vicinity of centers than in the vicinity of saddles. The illuminated path line segments in Figure 5.9 (b) indicate the interval used for the integration. Path lines seeded in vortex-like features form long centerlines due to the strong rotation within the vortex. In contrast, path line segments seeded in saddle-like structures diverge. This is consistent with the observation that interesting saddles are removed.

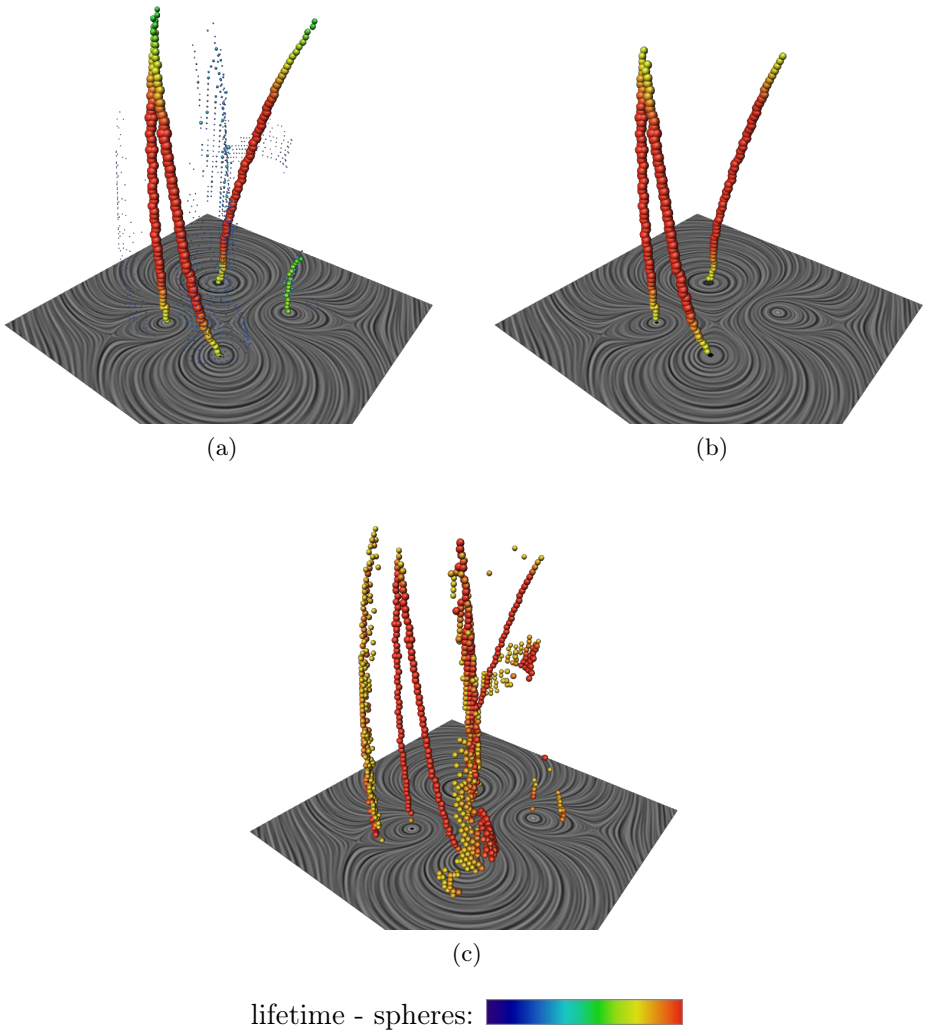

Figure 5.11 Motion of six Oseen vortices: (a) All features before filtering; (b) Applying the lifetime filter filters the short-living out. (c) Employing a shorter lifetime window also saddles are extracted.

Since vortex cores are extracted, Figure 5.10 shows a comparison with standard vortex indicators such as λ_2 and Q. The values of λ_2 and Q are color-coded in the LIC texture and in the spheres. The minima of λ_2 or the maxima of Q reveal nearly the same structures as our approach. With λ_2 or Q, however, separating structures such as saddles cannot be extracted.

The ability of the approach to filter out short-living features is illustrated in Figure 5.11. The chosen time window determines the maximal lifetime. All features with higher lifetime cannot be differentiated. Choosing a time window of length 1.0, only three long-living vortices remain.

Distinguishing between saddle and vortex regions by using the Jacobian leads to the results depicted in Figure 5.11 (c). In the example the lifetime for vortex-like regions is 0.6 and for saddle-like regions 0.1. With this differentiation all salient features including saddles are visible.

5.2.6 Discussion

The proposed method enables a Galilean invariant extraction of long-living structures, based on the concept of Lagrangian equilibrium points. It thereby consists of two properties: (i) the Lagrangian averaging that binds features to path lines; (ii) the life time that provides an importance measure for the features.

The method is still based upon two major thresholds $a_{threshold}$ and τ. While the first parameter determines whether a particle carries a feature, the second parameter represents a characteristic feature lifetime and depends on the scale of feature lifetimes in the given dataset. Both parameters are chosen heuristically. They should be eliminated.

5.3 The vortex merge graph

The approach introduced in the last section binds features to path lines by averaging the acceleration magnitude along the path lines. This introduces two major limitations: (i) it is not inherently clear that features are linked to path lines; especially in the case of as saddle point, it is obvious that particles only stay in the vicinity of the feature for a short time span; (ii) the averaging yields high computational costs for each time slice; while an efficient implementation is possible, still a lot of path lines have to be traced.

In this section, we propose an alternative point of view that considers features as spatiotemporal entities detached from single particles. The idea is also based on using the acceleration magnitude as a *local feature identifier* $\mathcal{F}(\mathbf{x}, t)$. Instead of averaging the scalar values along the path line, the acceleration magnitude field is examined for a fixed time step, i.e., by extracting the LEPs instantaneous. The temporal development of these features is no longer related to a particle trajectory and has to be tracked by other means. There are several concepts and algorithms available to solve similar tasks, e.g., Feature Flow Fields (FFF) [TS03, WTvGP10] or the tracking of vector field singularities [TWSH02, GTS04b].

For our approach, we will use the combinatorial tracking approach by Reininghaus et al. [RKWH12] as described in Section 2.2.2. The approach is chosen, since it deals with noisy data sets. We use the acceleration as a feature identifier that is based on derivatives of the velocity field. Typically, derivatives amplify the noise in the data. Thereby, the more complex the data set is, the more noise is a problem. Reininghaus et al. have shown that analytically defined tracking methods such as FFF cannot handle such data sets, but CFFF can. In addition, the paper proposes an importance measure for the tracked critical lines that combines persistence as a *spatial feature strength* with the idea of *feature lifetime* as introduced in the last section. It serves as an filter criterion to distinguish important from salient features.

We will use this new approach to extract vortices in time-dependent flows. It was already stated that a subset of the minima of the acceleration magnitude is related to vortex cores and this subset can be found using the Jacobian of the velocity field. We confirm this notion by analyzing the minima of the acceleration magnitude using different flow data sets in Section 5.3.1. Afterwards, the approach of Reininghaus et al. is adapted to the underlying physics. The original approach is not able to extract mergers and splits. In two-dimensional flows, mergers of vortices are common events. By interpreting the tracking fields introduced by CFFF as a graph, we determine an appropriate sub graph that represents the *vortex merge graph*, cf. Section 5.3.3. Afterwards, the results are shown in Section 5.3.4 and discussed in Section 5.3.5.

5.3.1 LEP as vortex cores

By the Euler equation, a subset of the LEPs is related to vortices. The Jacobian matrix thereby distinguishes rotational from saddle-like flow behavior. In the following, we examine the correlation of the rotational LEP to other vortex related criteria. Thereby, we will use vorticity $\omega = \text{curl}(\mathbf{v})$ as introduced in Section 2.1.2. The second quantity is the Okubo-Weiss parameter $Q = \|\mathbf{\Omega_v}\|^2 - \|\mathbf{S_v}\|^2$ [Oku70, Wei91]. It was also independently proposed by Hunt [Hun87]. This parameter employs the velocity Jacobian $\mathbf{J_v} = \nabla\mathbf{v}$ and compares the norm of the symmetric shear tensor $\mathbf{S_v} = \frac{1}{2}\left(\mathbf{J_v} + \mathbf{J_v}^T\right)$ with the norm of the anti-symmetric one $\mathbf{\Omega_v} = \frac{1}{2}\left(\mathbf{J_v} - \mathbf{J_v}^T\right)$. In the center of a radially symmetric vortex, $Q = \|\omega\|^2 > 0$, since $\|\mathbf{S_v}\|$ vanishes and $\|\mathbf{\Omega_v}\|$ becomes the norm of the vorticity $\|\omega\|$. At a saddle point $Q = -\|\mathbf{S_v}\|^2 < 0$. Hence, maxima of Q can be associated with vortex centers and minima with saddles. The third quantity is λ_2, which is the second eigenvalue of $\mathbf{S_v}^2 + \mathbf{\Omega_v}^2$ [JH95]. It is only related to vortices. Its minima are often used as vortex cores. Q and λ_2 are generally considered to provide synonymous information in the case of vortices. In two dimensions, it is easy to see that in areas of rotational flow behavior, $Q = -2 \cdot \lambda_2$. The last used flow quantity is the absolute value of the imaginary part of the Jacobian $\mathbf{J_v} = \nabla\mathbf{v}$. This quantity characterizes the angular frequency of revolution of a neighboring particles. Hence, its maxima also indicate vortex centers. The investigation is done using two data sets of free shear flows. First, a periodic vortex shedding behind a circular cylinder, cf. Appendix A.5, and the data set of a mixing layer, cf. Appendix A.7.

Cylinder. Figure 5.12 shows five vorticity related quantities of a cylinder wake snapshot. In each subfigure, we marked the features indicated by the quantity that are related to vortices by yellow balls. The vorticity field indicates the separating shear-layers rolling up in a staggered array of alternating vortices. The extrema reveal the known fact that the ratio between the transverse of vortex displacement and the wavelength slightly increases downstream with vortex diffusion. The second subfigure shows the Q-measure and the third subfigure λ_2. As already stated, they have similar characteristics. The fourth subfigure shows the imaginary part of the eigenvalues of the Jacobian. Finally, the magnitude of the material acceleration field is depicted. The minima, i.e., Lagrangian equilibrium points, mark vortex centers and saddles – we depicted both structures. It can be seen that the features coincide with the vortex cores identified by the other criteria. Note that the correct subset can thereby be determined by the Jacobian which corresponds to the field shown in the fourth image.

Mixing Layer. In contrast to the space- and time-periodic Stuart solution, cf. Appendix A.2, the mixing layer generally shows several vortex pairing events. In Figure 5.13, the distance between vortex LEPs (marked by balls)

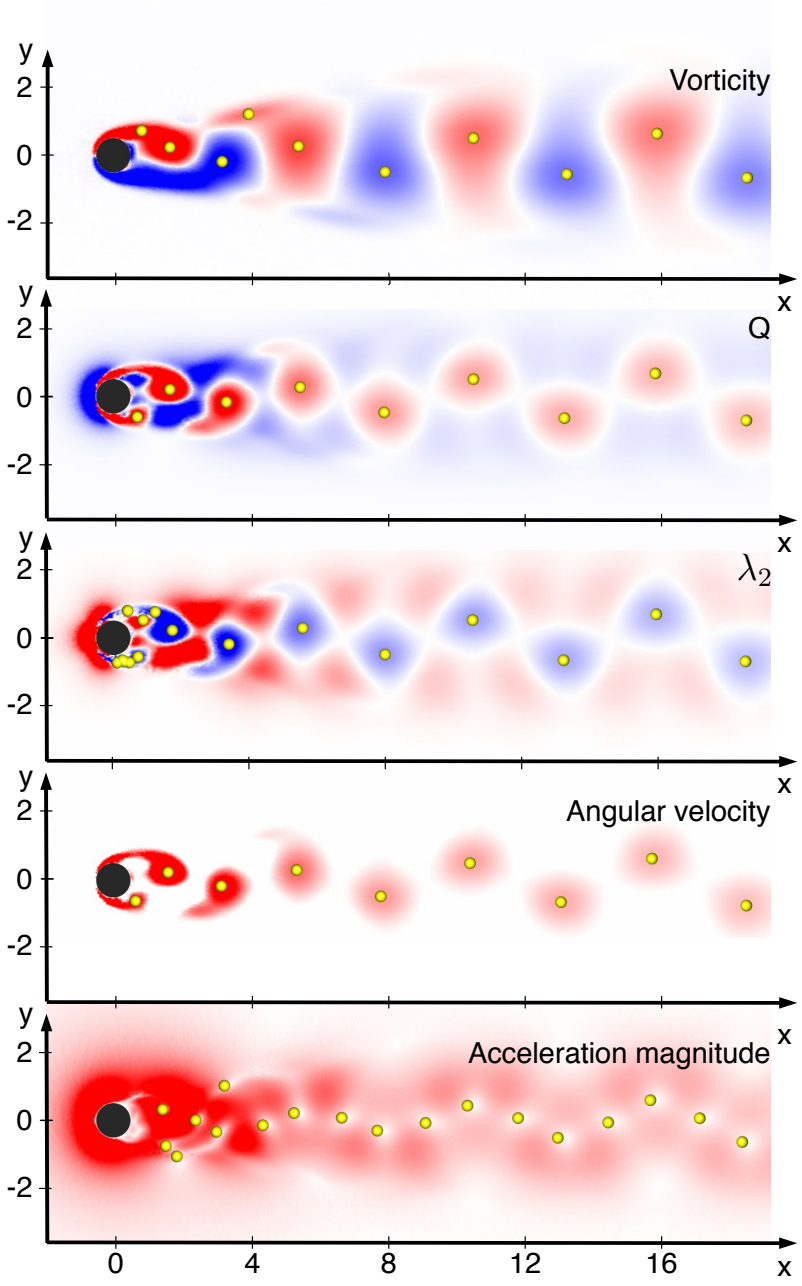

Figure 5.12 Visualization of a cylinder wake snapshot. Five vorticity-related quantities are depicted by color maps (red: positive values, blue: negative, gray: zero): (1) vorticity; (2) Okubo-Weiss parameter; (3) λ_2; (4) absolute value of the imaginary part of the eigenvalues of the velocity Jacobian – corresponds to the angular velocity; (5) material acceleration magnitude. The yellow spheres represent the extremal points typically used as features for the respective quantity.

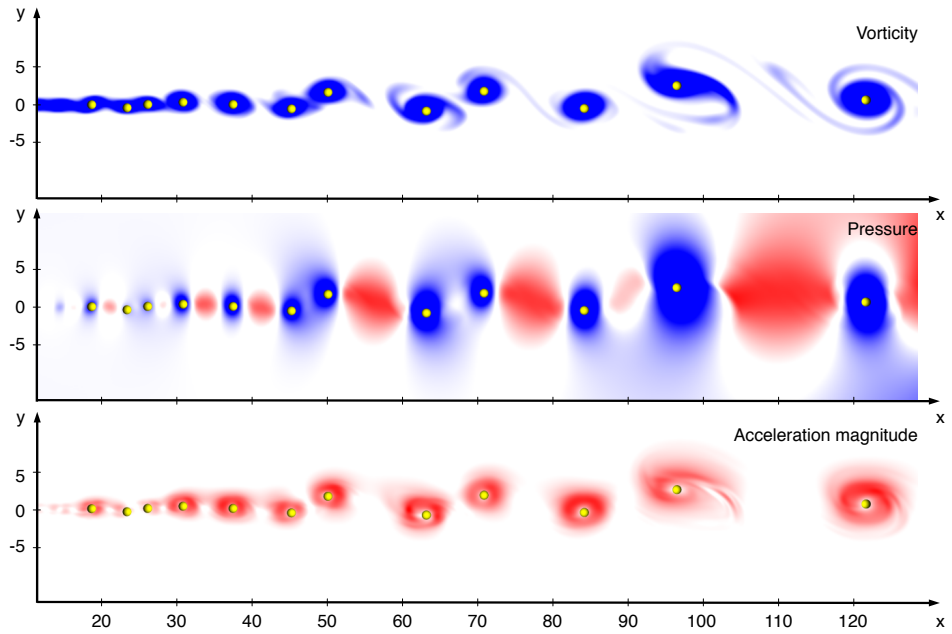

Figure 5.13 Visualization of a mixing layer snapshot. Comparison of vorticity (top), pressure (middle) and acceleration (bottom). The color scheme is blue (red) for negative (positive) values. The yellow spheres represent pronounced vortex LEPs.

are seen to increase in stream-wise direction as result of vortex merging. Furthermore, the locations of the LEPs (bottom) nicely correlate with the local maxima of the vorticity (top), and the local minima of the pressure (middle). For the acceleration magnitude, we just depict the minima that are related to rotational flow behavior.

In a nutshell, these two flow data sets have shown that there is a correlation between the LEP and vortex cores induced by other flow criteria. In the following, we will show how to robustly extract the points and their temporal evolution.

5.3.2 Persistence as a natural spatial importance measure

The first step to extract vortex core lines in time-dependent fluid flows is to determine the set of feature points in each time slice. Since we deal with complex data sets, noise is a problem of every quantity that is based on the derivatives of the flow fields – as the acceleration magnitude is such a quantity. In the combinatorial framework that is employed, homological persistence is used to filter out the LEPs that are not generated by noise. It has to be made sure that this cancellation of critical points does not discard LEPs that are related to the actual vortex cores. Fortunately, in the case of vortices,

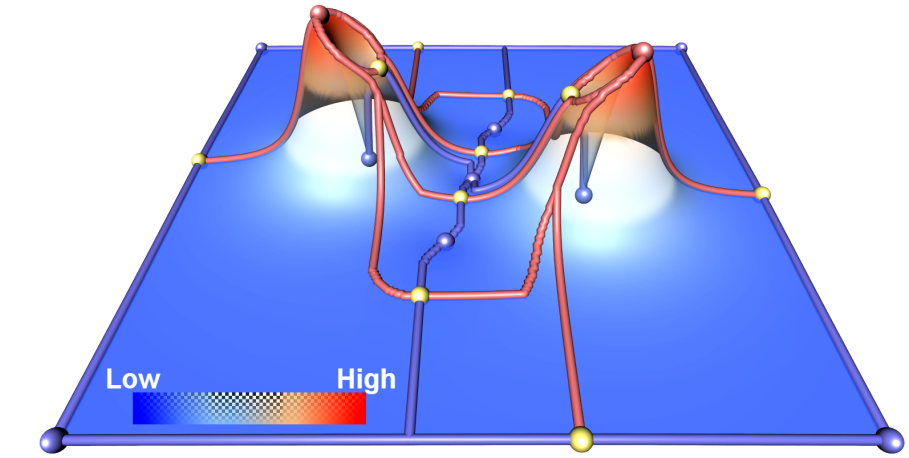

4

(a) Two co-rotating Oseen vortices

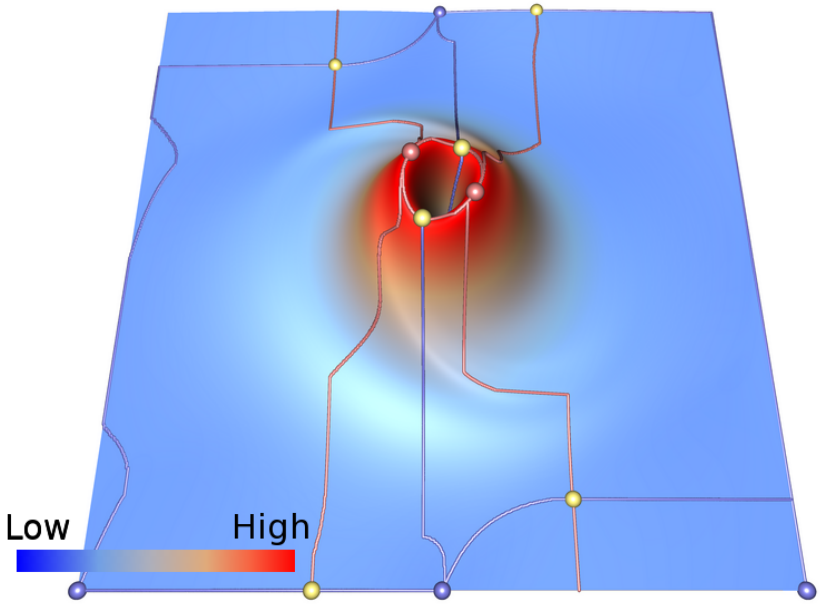

(b) Lundgren vortex: a non-circular vortex model

Figure 5.14 Acceleration magnitude for two vortex models displayed as colored height field over the flow domain. The topology of the acceleration magnitude is displayed by blue (minima), yellow (saddles), and red (maxima) spheres and the corresponding extremal lines; minima and maxima lines are shown as blue and red lines, respectively. In both cases the minima, representing the vortex core, are surrounded by clearly pronounced ridges.

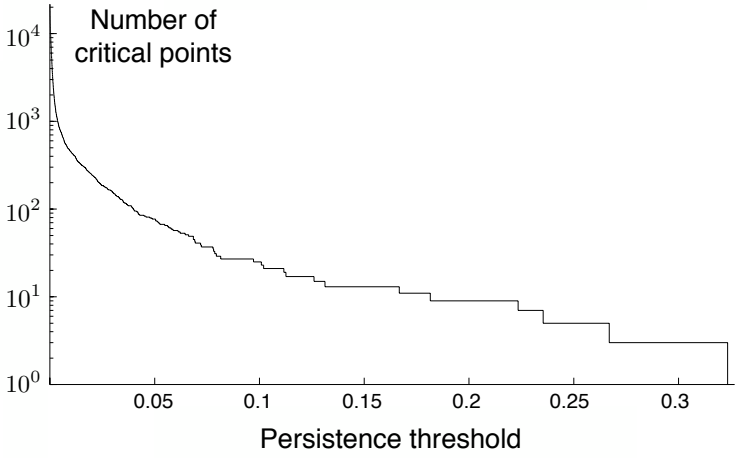

Figure 5.15 Persistence distribution of the data set in Figure 5.16. The number of critical points after persistence-based filtering is plotted against the persistence threshold level.

the LEPs are surrounded by a particular pronounced ridge. Two examples are shown in Figure 5.14 for the data set of two co-rotating Oseen vortices, cf. Appendix A.1, and the data set of a Lundgren vortex, cf. Appendix A.3. The persistence value of the minimum in this basin will be determined by the height difference to its associated ridge. This value is high compared to the persistence of the noise-related minima. Therefore, homological persistence is a sensible measure to filter out noisy topological structures in the acceleration magnitude. In Figure 5.16, the remaining minima at different persistence thresholds are shown for the data set of a jet, cf. Appendix A.9. It can be seen that at different persistence levels the minima related to vortices still stay untouched. The amount of remaining critical points compared to the employed persistence threshold is shown in Figure 5.15.

In addition to the noise cancellation, the height of the ridge is determined by the strength of the centripetal acceleration of the vortex. We assume that this is a good measure for the importance of the vortex. Thus, we can also use homological persistence as a spatial importance for vortices.

5.3.3 Extraction and implementation of the vortex merge graph

The focus of the original CFFF approach lies on noise resilient extraction of critical lines using homological persistence as spatial importance measure, cf. Section 2.2.1. Since the spatial importance of one of the critical points be-

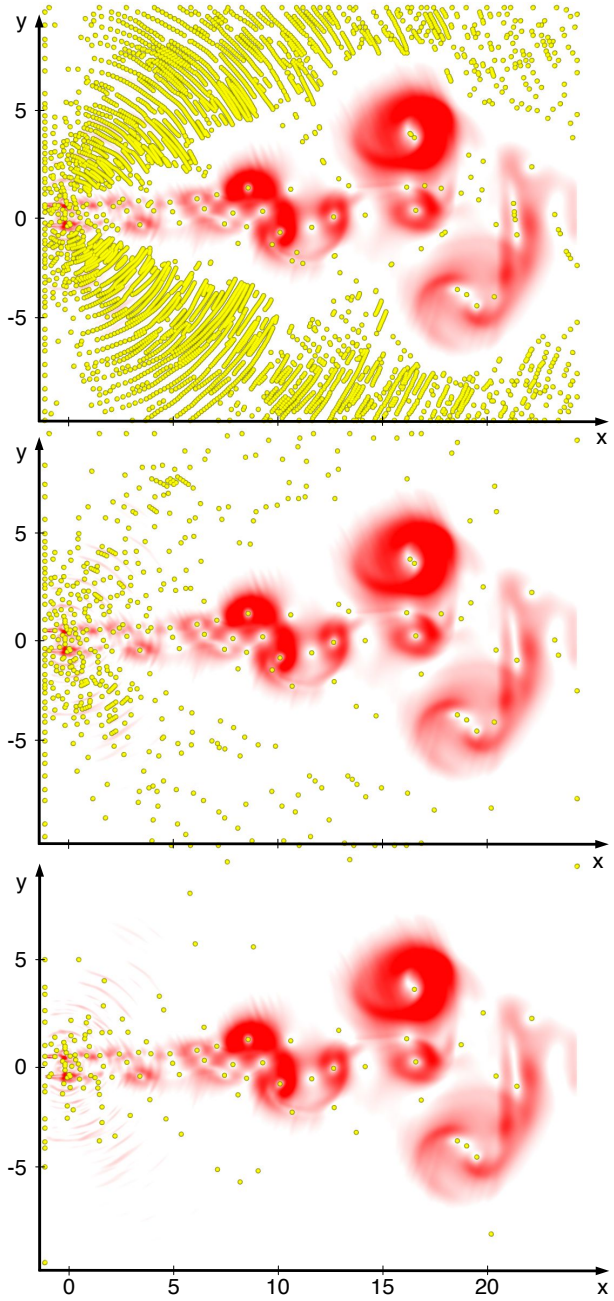

Figure 5.16 Persistence-based visualization of a jet snapshot. Visualization of the snapshot for persistence threshold levels of 0%, 0.5% and 2% of the maximum (from top to bottom). The color field represents the acceleration magnitude – with a color map that ranges from white (zero) to red (positive). The yellow balls represent LEPs filtered by their homological persistence with respect to the specified threshold levels.

comes arbitrarily small as they approach a merge or split point, CFFF, as originally proposed, cannot handle splits and merges of critical lines. In the following, a modification of the method of Reininghaus et al. is described that computes also the merge and split events, while maintaining its ability to handle noise. It considers only minima and maxima, i.e., neglects saddle points, which simplifies the integration of merge and split events. The modification is done to enable the extraction of vortex core lines, for which mergers are common events. The result is therefore called a *vortex merge graph*. Note that in principle the modified CFFF approach is also able to extract vortex core lines using arbitrary vortex related quantities. For example, if we would use vorticity as feature identifier, all minima and maxima could be tracked separately to built the graph.

For the case of minima or maxima, the basic idea of CFFF is to trace stream lines in two adjacent combinatorial gradient fields. Thereby, two minima or maxima are connected, if the stream lines in each others gradient field uniquely connect these points. Note that a stream line ends or starts at a minimum or maximum, respectively, if it starts in its basin. Therefore, another interpretation of the CFFF approach is that two minima or maxima of adjacent time slices are connected, if they fall in the topological basin of each other.

Computation. The basis of the tracking algorithm is the combinatorial gradient field simplified by homological persistence as described in Section 2.2.1. Let C_t be the set of critical points at time step t extracted from this field. The CFFF approach defines two functions: forward tracking $F_t : C_t \to C_{t+1}$ and backward tracking $B_t : C_t \to C_{t-1}$. They assign a critical point $c_1 \in C_t$ to another critical point c_2 in the next or previous time step, respectively, if c_1 falls into the basin of c_2. Two critical points c_1, c_2 of subsequent time steps are called *uniquely* tracked, if $F_t(c_1) = c_2$ and $B_{t+1}(c_2) = c_1$. CFFF considers only such unique tracking lines; the resulting set of lines therefore cannot contain mergers and splits. To allow for mergers, we drop the uniqueness tracking condition. Instead, we extract both the forward and backward tracking functions F and B for all time steps resulting in tracking graph.

For tracking of vortices in 2D flow fields, we are interested in minima of the acceleration magnitude field – the LEPs. A classification of the minima using the Jacobian of the velocity field is applied previous to the tracking. Thereby, we only track minima associated to rotational flow behavior. From the relevant set of extremal points, at first, the unique tracking graph is extracted resulting in core lines M. To compute the mergers, the following condition is tested for each end point of a line $e_t \in M$:

$$\exists T > 0 : F_{t+T}(...F_{t+1}(F_t(e_t))) \in M. \tag{5.10}$$

Loosely speaking, it is tested if the repeated evaluation of the forward tracking of the end point hits another tracked core line. If such a T is found, the line

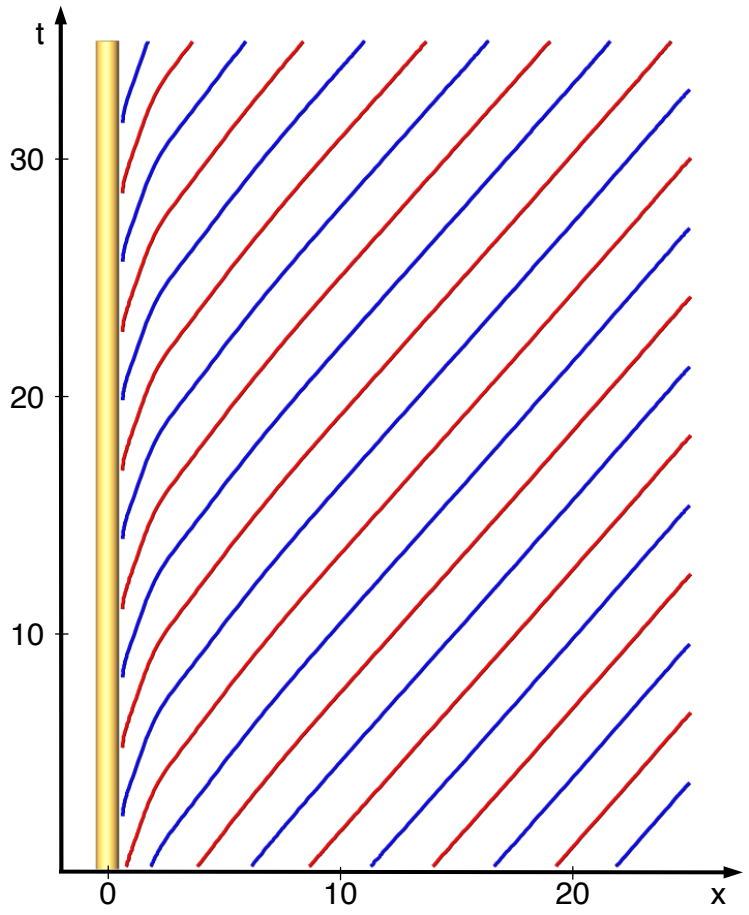

Figure 5.17 Tracked vortices of the cylinder wake in an x-t-view. Red (blue) marks positive (negative) rotation the vortices.

given by $F_{t+T}(...F_{t+1}(F_t(e_t)))$ is added to the result. To extract the split points, the above mentioned approach can be used by replacing end by start points and the forward by the backward tracking field. This is not needed for 2D flows, since split events do not occur in 2D flows in theory. The tracking graph is a merge tree.

Implementation of the tracking graph. Note that the forward and backward tracking represent discrete functions – they are given for each critical point in each time slice. Thus, the tracking functions for all time steps can be interpreted as a single directed graph containing both backward and forward tracking. This representation eases the implementation, since known efficient graph algorithms can be used for the evaluation.

To store the graph efficiently, the following requirements have been identi-

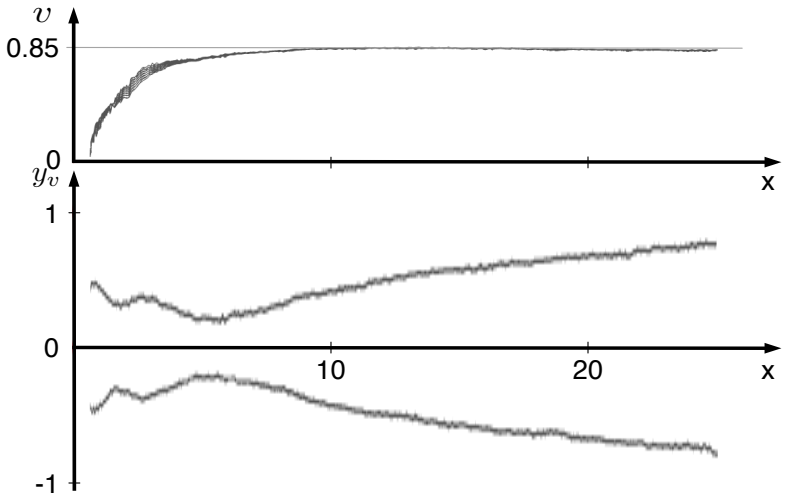

Figure 5.18 Plots of two quantities along the tracked vortices, namely their streamwise velocity component v (top) and their transverse displacement y_v (bottom). Note that each figure contains the history of many vortex evolutions from roll-up to convection out of the domain. Hence, several lines can be seen in each curve.

fied: (i) each critical point should be stored only once; (ii) the edges have to be stored including their direction; (iii) the implementation should allow a fast depth search in the graph to trace the connections between the unique vortex core lines; (iv) adding edges should be possible fast, but there is no need for a fast operation to remove them; (v) the coordinates and types of the critical points have to be stored. Note that each critical point can be identified by its time value and a unique identifier in the time slice – we call this a *global identifier of a critical point*.

Due to these requirements, we choose to assign each critical point a consecutive identifier in the tracking graph – two data structures map the global identifiers to the local ones and vice versa. Each edge is stored as a directed pair of node identifiers. For each node, the associated edges are stores distinguishing between ingoing and outgoing edges. In addition, the coordinates and types of the critical points are stored in two additional data structures.

Integrated persistence as a spatiotemporal importance measure. In Section 5.2, we introduced the concept of feature lifetime as an importance measure for critical points. While leading to much simpler results, this filter method is purely based on temporal measures. It ignores pronounced short-lived features, which can play a significant role for the flow. Therefore, the temporal importance measure as given by the feature lifetime should be

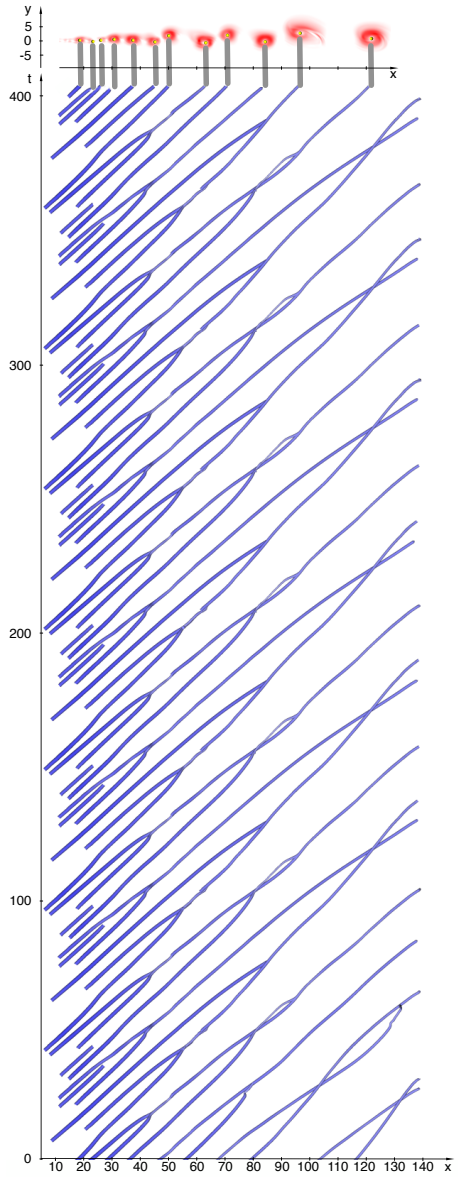

Figure 5.19 Spatiotemporal evolution of the mixing layer vortices. The top figure shows the acceleration magnitude field and LEPs at the final considered time. The bottom figure marks the tracked LEPs over approximately 5 downwash times. Numerous vortex merging events can be identified. The size and coloring of the vortex skeleton is determined by vorticity – more intense blue corresponds to lower vorticity. Note that the vorticity is negative everywhere.

combined with a spatial feature strength. The CFFF approach allows for a straightforward incorporation of homological persistence as a spatial importance measure for feature lines. In [RKWH12], the spatiotemporal importance measure is defined by integrating persistence along the feature line, i.e., by accumulating all persistence values on the line, cf. Section 2.2.2. Since the measure is not normalized, the lifetime of the feature is inherently represented by this measure – longer living features are more important if all structures have the same spatial strength. Using this importance measure, it is possible to filter out short-living weak features. Note that the importance measure is only defined on the unique vortex core lines. Thus, each vortex core is analyzed independently.

5.3.4 Results

As results of the above approach to extract vortex core lines, three free shear flows are investigated: the cylinder wake, the mixing layer, and the planar jet. These configurations represent different levels of spatiotemporal complexity from the periodic wake to the broadband dynamics and vortex pairing of the mixing layer and jet. The first two flows share a pronounced uniform far-wake convection velocity, while the jet structures move slower with stream-wise distance.

We investigate the LEPs for the wake, cf. Section 5.3.4, and analyze the vortex merging of the mixing layer, cf. Section 5.3.4, and employ the persistence-filter of LEPs for the jet, cf. Section 5.3.4.

Cylinder wake. Starting point is a periodic vortex shedding behind a circular cylinder, cf. Appendix A.5. This data set can be interpreted as benchmark problem – the occurring structures are well studied in the field fluid mechanics. Note that this data set contains no merge events.

Based on the tracked LEPs, Figure 5.17 shows the spatial-temporal vortex evolution. In the far-wake, a uniformly convecting von Kármán vortex street is observed. In the near-wake, the convection speed is significantly slower. This aspect is highlighted in Figure 5.18 (first subfigure). The stream-wise velocity of each vortex v (as part of $\mathbf{v} = (u, v)$), is a monotonically increasing function from 0.03 to about 0.85. The asymptote corresponds to the literature value [Wil96], which validates the extraction of the vortex core lines based on the acceleration magnitude. The transverse spreading of the vortex street, noted in Figure 5.12, is quantified in the following subfigure with the transverse location y_v.

It should be noted that tracked LEPs can be seen as markers of coherent structures. The LEP-based framework provides a convenient means for determining convection velocities and evolution of spatial extensions. The following investigations of the mixing layer and the jet flow emphasize this aspect.

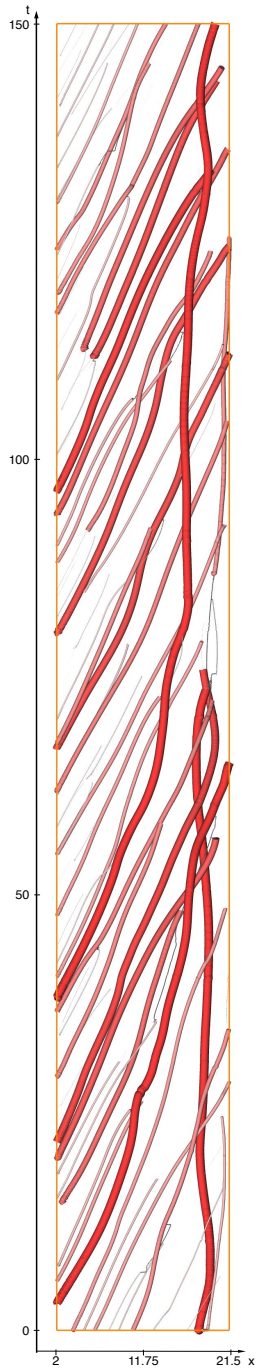

Figure 5.20 Spatiotemporal evolution of the vortex skeleton of the jet. The size and coloring of the vortex lines are determined by our spatiotemporal importance measure. The links between the individual vortices are shown as white gray lines.

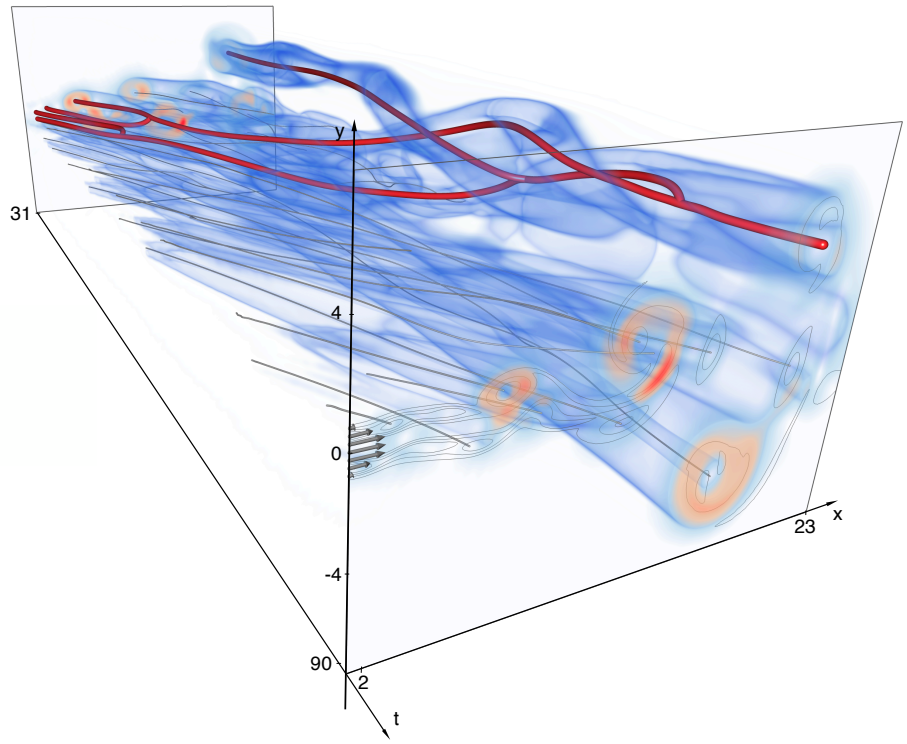

Figure 5.21 Close-up view of the vortex skeleton of the jet flow. The gray lines represent the extracted and filtered vortex cores. A few lines are visually highlighted by red coloring; they show a pronounced vortex merging event and the origin of the merged vortices. The acceleration is visualized by the blue volume rendering and the color coding in the front and back plane. For comparison, iso-lines of the vorticity are added to the front plane.

Mixing layer. The second investigated shear flow is a mixing layer, cf. Appendix A.7.

The vortex merging events are shown in Figure 5.19. Upstream, many vortices are formed. In stream-wise direction, numerous merging events can be identified, approximately 2 successive vortex mergers in the domain shown. Not all crossing of x,t-curves mark mergers since vortex pairs may rotate around their center before eventual merging. The figure strongly suggests a nearly constant stream-wise convection velocity, as expected from literature results and contrary to the cylinder wake dynamics.

Planar jet. Finally, the spatiotemporal evolution of the planar jet is investigated, cf. Appendix A.9.

The spatiotemporal evolution of the vortex skeleton of the jet is visualized

in Figure 5.20 in a similar manner as the wake, see Figure 5.17, and the mixing-layer, see Figure 5.19. Clearly, vortex merging events and a stream-wise decreasing convection velocity can be identified. In particular, some strong vortices remain for a long time near the exit. The importance of the vortices is indicated by the size of the lines. A three-dimensional close-up view is shown in Figure 5.21.

5.3.5 Discussion

In this section, a framework to robustly extract vortex merge graphs in two-dimensional time-dependent flow fields has been proposed. The extraction of the LEPs is resilient to noise due to the utilization of robust tools that employ homological persistence. The CFFF tracking approach was successfully adapted to extract merge events. The results emphasize the relevance of the LEPs as vortex cores. The core lines have been identified for three different data sets of growing complexity. Thereby, the extracted structures show the expected physical properties. In addition, the importance measure allows for a hierarchy of the vortex core lines. In Section 5.5, we will further investigate the extracted core lines and compare them with core lines extracted from other vortex-related quantities. Thereby, the same tracking frame work introduced in this section can be used.

5.4 Vortex regions

As stated in Section 5.1, analyzing the acceleration magnitude field, it can be observed that vortex-like minima are enclosed by pronounced ridges that bound the basins of the minima. In this section, such a basin is used to define the region of influence of a vortex, i.e., the vortex region. This provides a basis for a consistent treatment of vortices: While a vortex core is defined as a minimum, the corresponding basin, bounded by maximum lines, is interpreted as the associated vortex region, cf. Section 5.4.1.

In contrast to previous work, this novel definition of a vortex region combines the following three advantages:

1. It is Galilean invariant. The definition of the vortex regions is solely based on the acceleration, which is Galilean invariant. This is an essential property when dealing with time-dependent flows.

2. It allows for vortex regions of arbitrary shape. Using scalar field topology as the basis for the definition of vortex regions, the extraction algorithm is not restricted to star- or convex-shaped geometries.

3. It does not require any threshold or iso-value. This enables an unsupervised extraction of vortex regions in complex time-dependent datasets. This is important, e.g., for analyzing very large data sets.

The method is described in detail in Section 5.4.2 and Section 5.4.3. In Section 5.4.4, it is evaluated using model systems from computational fluid dynamics. The results are compared to other definitions of vortex regions and ridges of the finite time Lyapunov exponent (FTLE) field.

5.4.1 Motivation

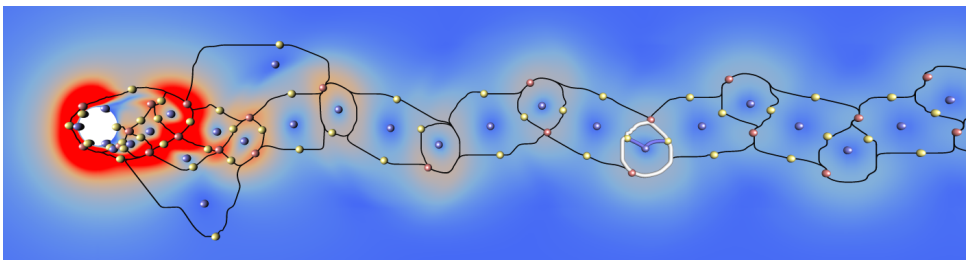

Figure 5.22 This image shows one time slice of the cylinder dataset. Color represents the acceleration magnitude overlaid by its critical points and maxima lines connecting maxima with saddles. The topological skeleton is used to extract vortex regions defined as the region containing a vortex-like minimum bounded by maxima lines. The minima lines (blue) connecting minima with saddles are only displayed for the highlighted region.

In this section we motivate our definition of vortex regions for two-dimensional flow fields.

In Figure 5.14, we observed for the Oseen as well as for the Lundgren vortex that the minima of the acceleration magnitude field corresponding to vortex cores are enclosed by pronounced ridges. This is a typical structure that can also be found in other flows, e.g., in the flow behind a circular cylinder, as shown in Figure 5.22. This observation leads to the new definition of a vortex region as the area containing a vortex-like minimum of the acceleration bounded by the corresponding ridge.

In terms of topology, the region is given by the basin of the minimum. It is bounded by the associated maxima lines, which separate the minimum from other minima in the field. This definition of the vortex region is parameter-free. Due to its topological foundation, the boundary of the regions can be arbitrarily shaped. Note that for each minimum in the topology one such region exists. Thus, it is important to restrict the definition to minima that were extracted using the already mentioned Jacobian filter criterion.

Note that the notion of vortex regions is inherently vague. For arbitrary vortices, the region of rotational flow behavior can be infinite, as in the example of the Oseen vortex. Thus, each definition of vortex regions has to settle on criteria which respect a certain perspective. Our definition of a vortex region is driven by the following conditions:

- being formulated in consistency with vortex cores;
- being independent from any threshold value;
- allowing vortex regions of arbitrary shape;
- being Galilean invariant;
- reflecting Lagrangian particle motion.

The latter two criteria are inferred from the definition of the LEP as the regions are based on the same quantity.

5.4.2 Algorithm

In this section, we describe how we can robustly extract the vortex regions proposed in Section 5.4.1. In the following, the algorithmic pipeline as shown in Figure 5.23 is briefly summarized.

The input of the method is of a two-dimensional, time-dependent vector field. The first step is to compute the magnitude of the acceleration of this field, from which minima are extracted. The Jacobian filter classifies the minima into vortex- and saddle-like. The remaining minima are then tracked as described in Section 5.3. For each time step, the vortex regions, i.e., the associated basins of the minima, are determined using the combinatorial algorithmic framework as for the minima extraction. Finally, a triangulated surface is generated, which connects the individual boundary lines using an advancing front scheme

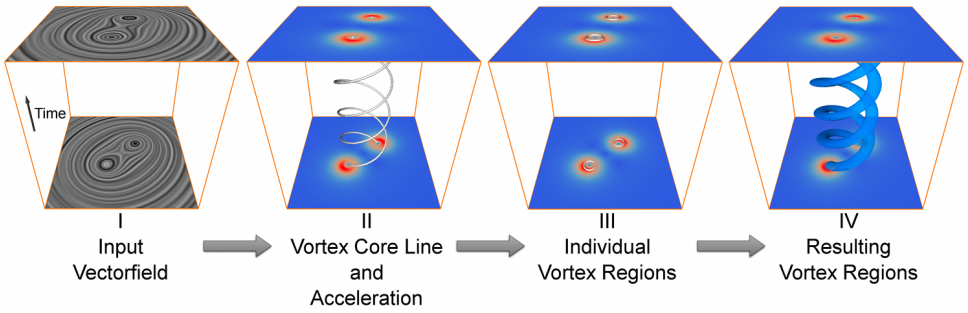

Figure 5.23 Overview of the vortex region extraction pipeline; (i) as input, a time-dependent vector field is used; (ii) The acceleration magnitude and its topology is computed using robust algorithms; the minima representing vortex cores are tracked over time; (iii) the individual vortex regions for each slice are computed; (iv) the tracking is used to connect the region boundaries.

in a post-processing step.

Note that the simplification using homological persistence is essential in our context, since a topological over-segmentation would not result in the correct vortex regions. In addition, in the vicinity of merge points, the topological basins depend more strongly on the persistence threshold than along other parts of the merge graph. There, their shape might change considerably from one time step to another. We therefore only extract vortex regions along the unique vortex core lines. Along these lines, the importance measure is given which can be transferred to the vortex regions.

Vortex region extraction. The vortex regions are defined as the associated basins to the acceleration minima and as such are also part of the scalar field topology. Thus, they can be extracted using the same framework as for the minima computation as presented in Section 2.2. The topological skeleton, i.e., the critical points and separatrices, contains all necessary information to extract the basins.

Given the vortex cores represented by minima and the topological skeletons in each time step, Algorithm 5.1 illustrates the general approach. For each point of each time-dependent vortex core line (Lines 1,2), we fetch the associated topological skeleton (Line 3). We then determine the boundary of its associated basin (Line 4) and append these lines to the vortex core line (Line 5). Finally, we build a surface from the vortex region lines using a simple advancing front approach that is not further described here (Line 6).

The main step, the extraction of the boundary of the basin, is given in Algorithm 5.2. The essential parts of the topological skeleton needed are the saddles connected to the current minimum (line 1) and the maximum lines starting in these saddles (line 2,3). This fact is illustrated in Figure 5.22.

Algorithm 5.1: Main vortex region algorithm

Input: Vortex core lines C, Topological skeletons T
Output: VortexRegions R
R = getVortexRegions(C,T)

```
1: for all L ∈ C do
2:    for all P ∈ L do
3:       S ← getSkeleton(P, T)
4:       B ← getBasinBoundary(P, S)
5:       L.append(B)
6:    L.VortexRegions ← TriangulateRegions(L)
```

Algorithm 5.2: Find basin boundary for a single minimum

Input: Minimum P, Topological skeleton T
Output: Basin boundary of minimum B
B = getBasinBoundary(P, S)

```
1: connSaddles ← getConnectedSaddle(P, T)
2: for all saddle ∈ connSaddles do
3:    maxLines ← getMaxLinesOfSaddle(saddle,T)
```

There, one basin boundary is highlighted as white line. Note that the minima lines (blue) connecting the minima with the saddles are only displayed for the highlighted region.

5.4.3 Implementation details

To achieve a good reproducibility of the results, this section presents three implementation aspects.

We employ the combinatorial framework described Section 2.2.1. In this framework, the extraction of the saddles connected to the minima is quite simple. The maxima lines are then extracted by integrating a combinatorial streamline, cf. Algorithm 2.1.

Note that the maxima lines in a combinatorial gradient vector field can share edges in the simplicial graph, or cell graph, respectively. To get the boundary without these artifacts, we need to discard these parts of the maxima lines. Therefore, we remove the points of the lines that are present twice in one vortex region.

As the combinatorial streamlines can only follow the edges of the given cell graph, the resulting vortex regions are not smooth enough for an efficient visual perception of the generated surfaces. Therefore, we apply a smoothing step to the resulting boundary lines before we construct the surface. For a depiction of this post processing step, we refer to Figure 5.24.

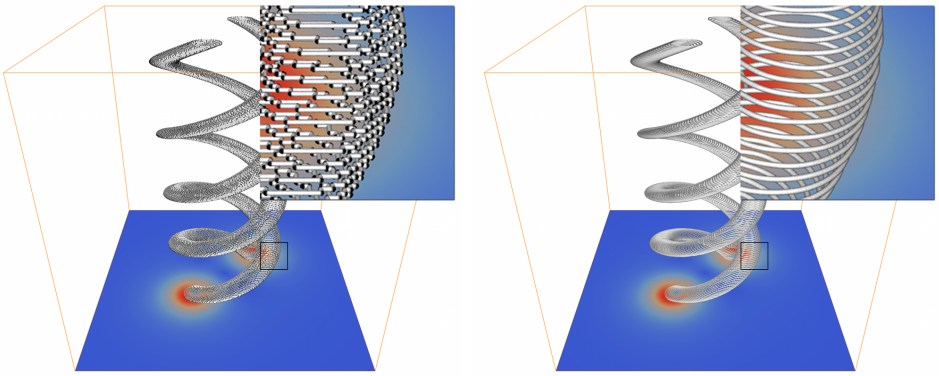

Figure 5.24 Individual vortex region boundaries for the dataset of two co-rotating Oseen vortices. Due to the combinatorial approach for the region extraction, a post-processing of the extracted vortex region boundary is necessary to achieve a good visual quality.

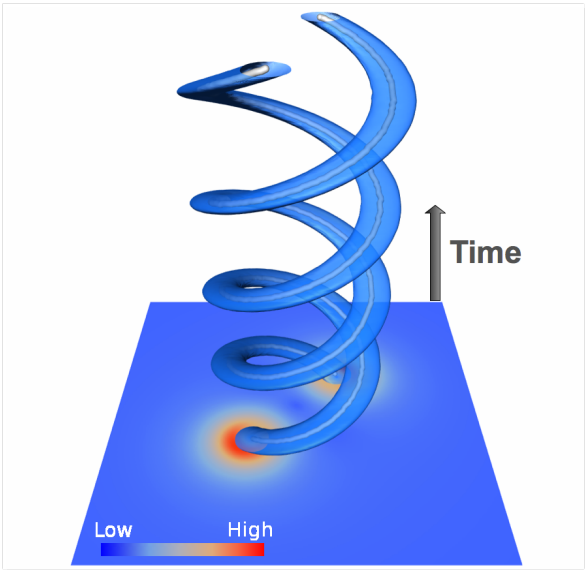

Figure 5.25 Tracked vortex regions of the Oseen dataset. At the bottom, the acceleration is shown. The vortices are indicated by their cores (white lines) and the boundary of the regions (blue).

5.4.4 Results

We apply our algorithm for extracting vortex regions to three different datasets. Since all flows considered in this section are planar and non-stationary, we depict time as third dimension.

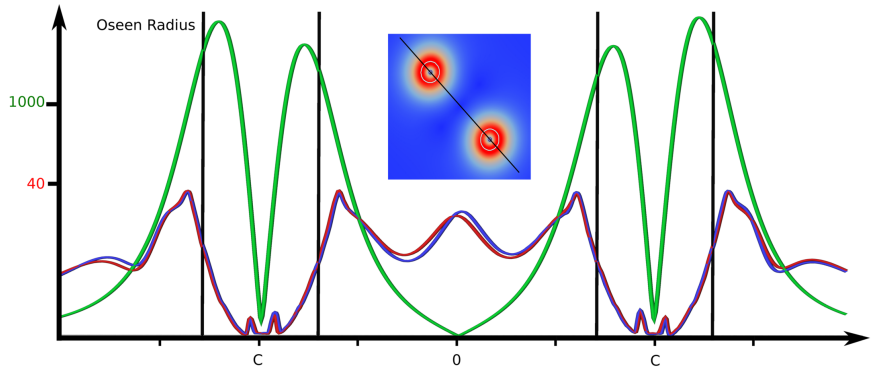

Figure 5.26 Plot of the forward (red) and backward (blue) FTLE and the acceleration magnitude (green) for a cut in the domain of the Oseen dataset as shown in the image. The values are sampled on the line shown in the center image. The parameter r_c of the Oseen vortex is also shown (black lines).

Co-rotating Oseen vortices. In Figure 5.25, the first data set is shown – a model example of two co-rotating Oseen vortices, cf. Appendix A.1. At the bottom, the acceleration magnitude is encoded in color. Thereby, red indicates high and blue low acceleration. There are two blue pipes emanating from the bottom slice that show the evolution of the circular region. Within the transparent pipes, the tracked vortex core lines can be seen. The regions are correctly tracked over the complete time the core lines exist.

To analyze the relation of the parameter r_c in the definition of two co-rotating Oseen vortices, cf. Appendix A.1, with the size of our vortex regions, we plotted the acceleration magnitude (green) along a cut on one slice of the dataset, see Figure 5.26. Additionally, the forward (red) and backward (blue) FTLE values along this line are shown. FTLE is computed for one sixth of a period of the dataset. While the maxima of the acceleration are closer to the vortex center c than the parameter r_c, the maxima of the FTLE are further away.

Cylinder dataset. The next dataset analyzed is the cylinder data set, cf. Appendix A.4. In Figure 5.27, the vortex regions are depicted for nine shedding periods. The extracted surfaces are colored by the acceleration magnitude. Time is again chosen as third dimension. Red coloring represents high values and blue low values of the acceleration magnitude. The vortices detach from the cylinder as weak features. Their spatial importance is growing quickly and attenuates in the flow. As can be seen, the regions do not represent a single value of the acceleration. Thus, iso-surface extraction cannot be used to determine the region boundaries.

In Figure 5.28, a comparison of different definitions of vortex regions is

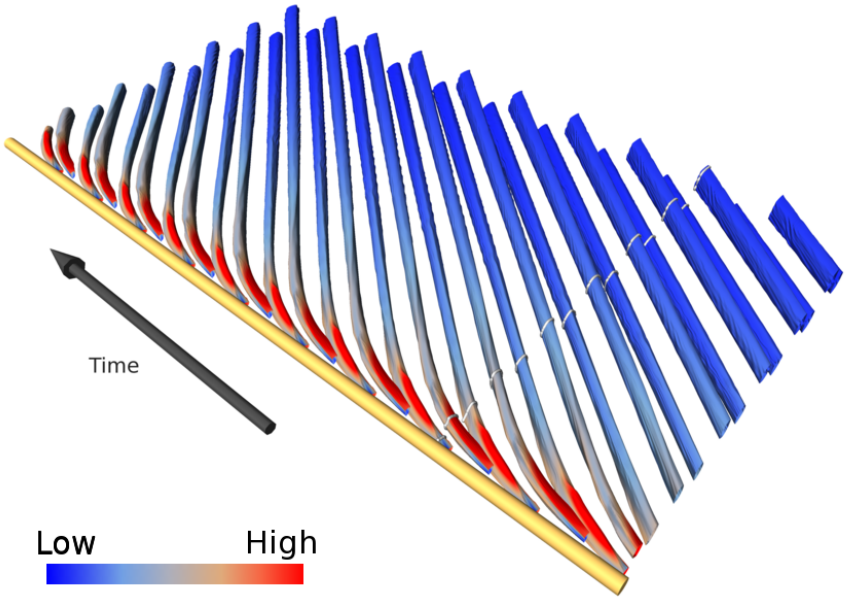

Figure 5.27 Tracked vortex regions of the cylinder dataset colored by the acceleration magnitude. Red coloring represents high values and blue low values. Due to the different scalar values on the surface, these regions cannot be determined by iso-surface extraction. The white rings enclosing the vortex regions refer to the time slice shown in Figure 5.28 (a) and Figure 5.30 (c).

shown. The minima of the acceleration magnitude (red) and the critical points of vector field topology (green) are depicted in each image. To extract the critical points, an appropriate frame of reference was chosen that reveals the typical pattern of the von-Kármán vortex street. Note that directly behind the cylinder the locations of the critical points and the vortex cores differ very much. The revealing frame of reference is not correctly chosen for these points. It depends on the velocity of the vortices, which are slower directly behind the cylinder. Figure 5.28 (a) shows the result of our method. The coloring of the slice is determined by the acceleration magnitude. It can be seen that the region boundary cannot be determined by an iso-value. Furthermore, the regions get larger with growing distance to the cylinder. Figure 5.28 (b) and (c) show iso-values of different scalar quantities that are used to identify vortices. All these quantities are Galilean invariant. First, vorticity is shown. While the size of the outer regions stays nearly constant, the inner regions shrink with growing distance to the cylinder. Directly behind the cylinder, regions of different vortices merge. The second quantity used to identify vortex-like behavior is λ_2. The third quantity is vortex strength as introduced by Bauer et al. [BPSS02]. This is magnitude of the imaginary part of the complex eigenvalues of the Jacobian matrix. As stated in Section 5.1, this quantity

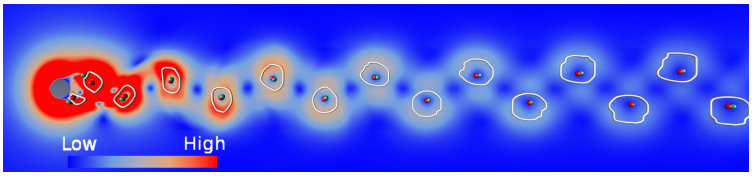

(a) Our Method

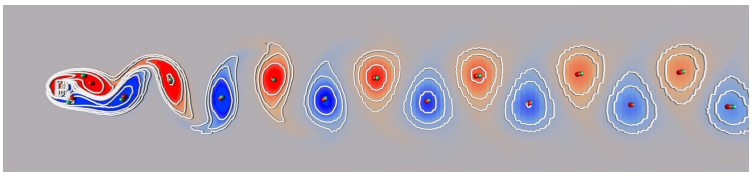

(b) Vorticity Iso-lines

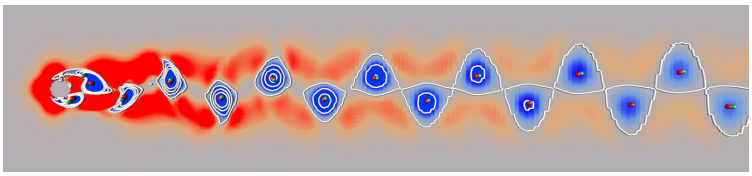

(c) λ_2 Iso-lines [SRE05]

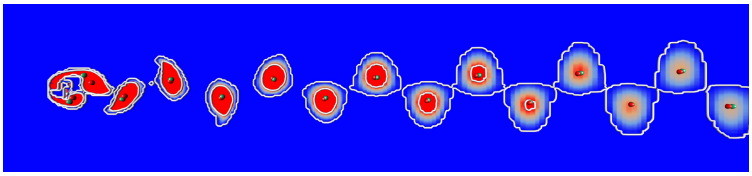

(d) Angular Velocity [BPSS02]

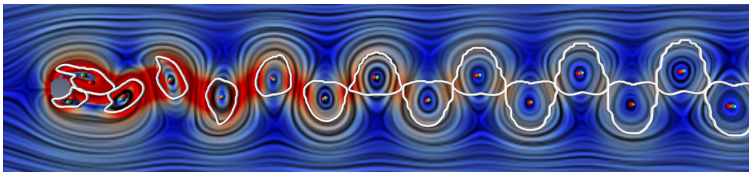

(e) Tangential Velocity Maximum [GTS$^+$04a]

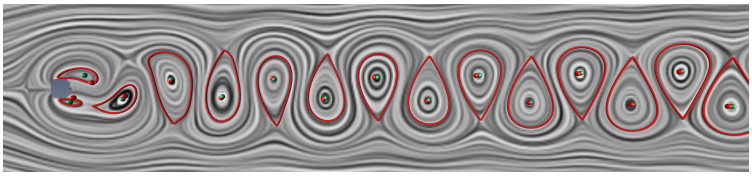

(f) Streamline-based [PKPH09]

Figure 5.28 Comparison of different definitions of vortex regions, computed for the cylinder dataset. The coloring of the slices is determined by the quantity the regions are based on. In all figures, the critical points (green) of vector field topology are depicted. The red points are the minima of the acceleration magnitude representing vortex cores.

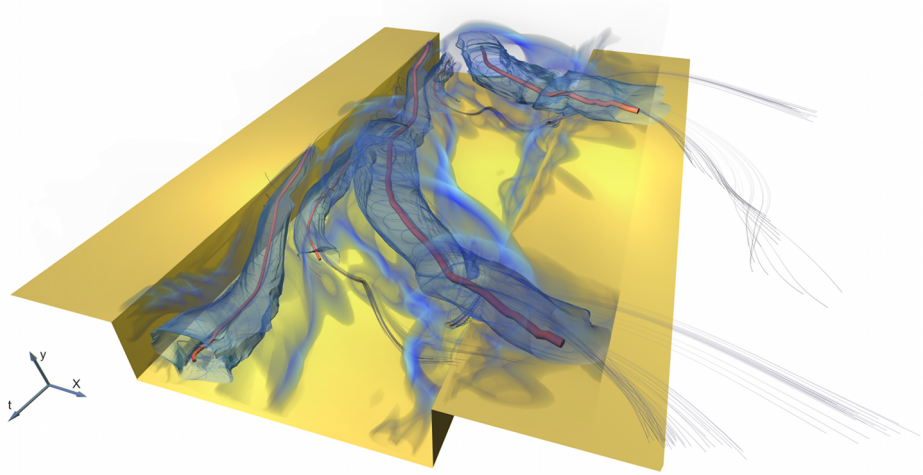

Figure 5.29 Time-dependent vortex core lines (red) and their associated vortex regions (blue) extracted for the dataset of a cavity. The acceleration is depicted as volume rendering. Additionally, two kinds of path lines are depicted: the first ones are seeded directly at the extracted vortex core lines and the other are seeded in the vicinity.

corresponds to the angular velocity. Both quantities, λ_2 and vortex strength, show comparable results in size and shape. The size of the outer regions stays constant when moving down the flow and the inner regions shrink. Thus the impression of the development of the vortices strongly depends on the chosen iso-value.

In contrast to the first four definitions, the regions in Figure 5.28 (e) and (f) depend on the chosen frame of reference as well as on the critical points of the vector field topology. The first method searches for the maximum tangential velocity on a fan of rays send out from a critical point. The resulting regions are therefore restricted to star-shaped geometries. Surprisingly, the regions have nearly the same shape and size as the outer regions in Figure 5.28 (e) and (d). In Figure 5.28 (f), the regions are determined by searching closed streamlines in rotated versions of the vector field. The image shows the largest boundaries that can be found beginning at the critical points. The shape of these regions differs most from the other results. Their size stays constant after some initial growth.

Flow over a cavity. A more complex model is the flow over a cavity, cf. Appendix A.6. In Figure 5.29, the flow over the cavity (yellow) moves from left to right and time is represented by the third dimension pointing from back to front. This is again a periodic data set of which one period is shown. The acceleration magnitude field is displayed by volume rendering (blue). Path

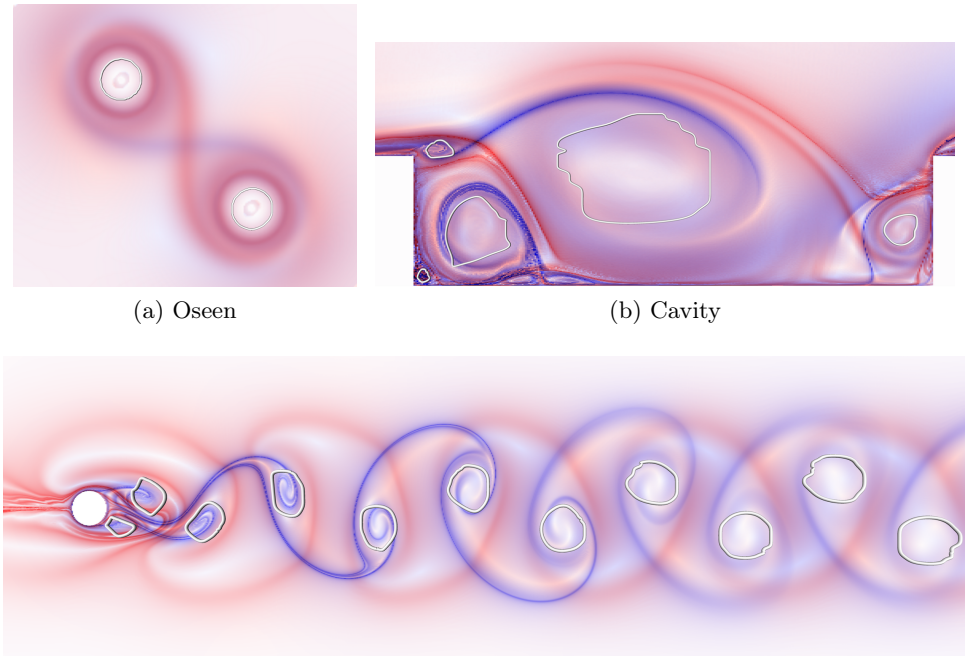

(a) Oseen (b) Cavity

(c) Cylinder

Figure 5.30 Forward (red) and backward (blue) FTLE for the Oseen (a), Cavity (b), and Cylinder (c) datasets. For the Oseen vortex pair, the FTLE was computed for the sixth part of a period; the FTLE was calculated for the fifth part of a period for the cavity; and for the cylinder the FTLE was computed for two shedding periods. The vortex regions for these datasets are depicted additionally. A correlation especially between the ridges of the backward FTLE and the vortex regions can be seen.

lines, seeded in the vicinity of the extracted vortex core lines (red), exhibit typical vortex behavior, swirling around the tracked minima of the acceleration. The thickness of the core lines encodes their spatiotemporal importance, i.e., the integrated persistence, cf. Section 5.3.3. For a good visual perception, we focused on the three most important vortex core lines. The blue surfaces indicates the boundaries of the vortex regions extracted with our method. It can been observed that the region of the central vortex core line is growing as the vortex detaches from the leading edge and moves through the cavity over the trailing edge.

Comparison to FTLE. In Figure 5.30, the computed localized finite-time Lyapunov exponent (L-FTLE) for the different datasets is shown, cf. Section 4.2. In the image, the blue coloring shows backward FTLE that corresponds to convergence of particles and the red coloring depicts forward FTLE that corresponds to separation. The vortex regions extracted from the acceleration magnitude of this slice are added to the image. In Figure 5.30 (a), the ridges of both forward and backward FTLE of the co-rotating Oseen vor-

tices enclose the vortex region. While the shape of the extracted vortex region boundary is similar, the size is smaller. This can also be seen in the plot shown in Figure 5.26. The same observation can be made for the cavity in Figure 5.30 (b). Here, especially the backward FTLE ridges (blue) correspond to the shape of the extracted vortex regions. In Figure 5.30 (c), the ridges of the backward FTLE (blue) are similar to the shape as well as the size of the regions.

Performance. Note that, given the vortex core lines and the individual combinatorial gradient vector fields, the running time for the extraction of the vortex regions is insignificant. The time to compute the results shown in this paper is therefore given by the time of the vortex core line extraction. For a detailed running time analysis of the combinatorial feature flow field method, we refer to [RKWH12].

5.4.5 Discussion

In this section, a novel vortex region definition based on the extremal structures of the magnitude of the acceleration is proposed.

From a theoretical perspective, this definition has three important properties. First, it is independent from the chosen frame of reference of the underlying vector field, since it is based on the acceleration. Furthermore, the vortex regions are not restricted to star- or convex-shaped geometries. Finally, it does not depend on a user specified parameter such as a threshold or an iso-value.

From a practical perspective, the proposed definition allows for an efficient and robust algorithmic treatment as was demonstrated in Section 5.4.4. Even if the acceleration magnitude contains a lot of spurious structures as in the dataset shown in Figure 5.29, we are able to reliably extract the vortex cores and corresponding vortex regions.

The definition of vortex regions based on the topological skeleton of the acceleration magnitude can in principle be transferred to three dimensions – analogue to the definition of the vortex cores.

5.5 Statistical analysis

After using the acceleration as an identifier for vortex core lines in Section 5.3 and their regions of influence in Section 5.4, we now want to analyze the behavior of other vortex related quantities along the vortex merge graph and within the vortex regions. We will therefore reuse the quantities of Section 5.3.1 that are related to vortices such as pressure, Q, vorticity ω, or λ_2.

Exemplary, we will extract vortex core lines using vorticity and λ_2 with the same tools as described in Section 5.3 and compare these graphs to the one coming from the acceleration magnitude. The extracted vortex core lines based on these quantities are similar but not identical. The differences are becoming more pronounced for strongly unsteady fields. This is mainly a consequence of the fact, that the acceleration considers the temporal change of the flow while the others are purely based on one time-step.

The goal of the analysis is to understand their relations and differences also concerning merge events and their point in time. Our employed framework consists of different parts. We provide tools to select substructures in the vortex skeleton. An abstract representation of the graph helps to focus on the quantities detached from its the geometric embedding. Scatter plots and parallel coordinates support the exploration of different flow quantities along the vortex core lines. Box plots are used express their distribution in the vortex regions of a connected vortex substructure.

5.5.1 Explorative tools

The various definitions of vortex cores and vortex regions motivate a thorough analysis of the differences and similarities of the resulting structures. The availability of explicit merge and split graphs for different measures provides a good basis for this. The following analysis considers scalar feature identifiers along extracted core lines and for vortex regions.

Analysis of Vortex Core lines. The analysis of the vortex core lines consists of two components: First, different quantities sampled along these lines are visualized. Second, subsets of the merge graph are interactively selected for further inspection. The approach also supports the brush-and-link concept.

Visualization – We provide two options to explore quantities along the merge graph. Parallel coordinates provide a first insight into the correlation of different scalar measures of interest. The quantities are sampled along the merge graph. Due to the high temporal resolution it suffices to display the information for every n-th point on the graph. This reduces visual clutter and removes redundant information. To provide a better visual perception, areas of high line density are darkened by rendering the lines of the parallel coordinates as *glow lines*. This is done by rendering each line l_i as a stripe with width d and

decaying opacity from the centerline to its boundary in a subtractive color model. In detail, let p be the current pixel, $O_{l_i,p}$ be the opacity of line l_i at pixel p, $C_{l_i,p}$ be the color of line l_i at pixel p, and C_B be the background color, which is white in our case. The color C_p of pixel p is then:

$$C_p = C_B - \sum_{i=1}^{N} C_{l_i,p} \cdot O_{l_i,p} \tag{5.11}$$

Note that only lines with a maximum distance d to p have to be considered. The rendering of the glow lines as stripes is done using the approach of Merhof et al. [MSE+06]. The use of glow lines results in smooth parallel coordinates by composing the individual lines. An example is depicted in Figure 5.31.

The second exploration technique reveals correlations between quantities by use of scatter plots.

Selection – In both of these plots, the user can select interesting structures. The selection is highlighted in the spatial representation of the graph. In addition, the user can select vortex structures by picking a point on the vortex merge tree. All substructures that belong to the selected tree are extracted from the graph and segmented into individual vortices. The subgraph is therefore split into segments that contain no merge event. For each selected substructure, the above mentioned visualization tools can be applied. An abstract representation of the tree additionally provides a good basis for comparison of vortex graphs based on different feature identifiers.

Analysis of Vortex Vicinity. For the vortex regions associated to the selected subgraphs or the whole vortex merge graph, we provide the following analysis tools: First, the different flow quantities are visualized on the circular area enclosing the vortex regions. This gives the user a first impression of their behavior. To indicate their correlation along the vortex regions, we make use of the parallel coordinates and scatter plots mentioned above. It is thereby possible to represent the quantities for a set of regions sampled along the selected graph or an individual region.

To get an idea of the distribution of the scalar values in regions along a selected subgraph a further statistical analysis is of interest. For this purpose a more complex tool is provided. Its interface, depicted in Figure 5.37, consists of three parts: At the top, an abstract representation of the vortex graph is given. Time is thereby represented by the x-direction. Each segment of the vortex merge graph is a toggle to select this structure in the plots. An optional coloring of the buttons links the segments to their spatial representation and the corresponding plots. In the second part, different plots of the quantities can be shown. Again, the x-axis represents the time and the y-axis the values of a single quantity. Mean, median, minimum and maximum values and percentiles are visualized by lines and box plots. The third part of the user interface

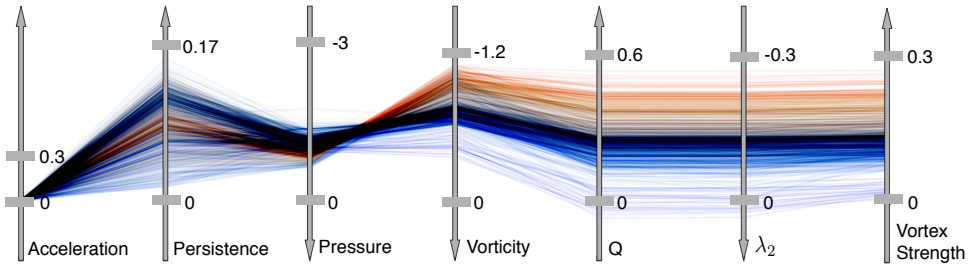

(a) Vortex skeleton of the Mixing Layer

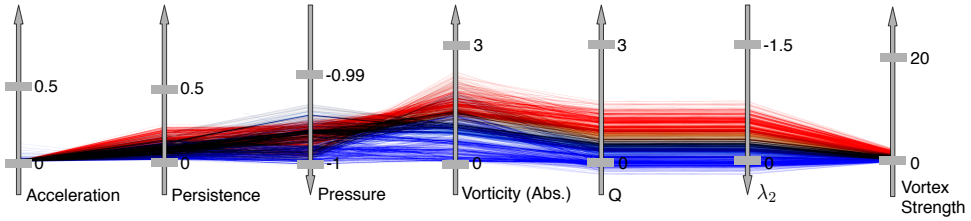

(b) Vortex skeleton of the jet

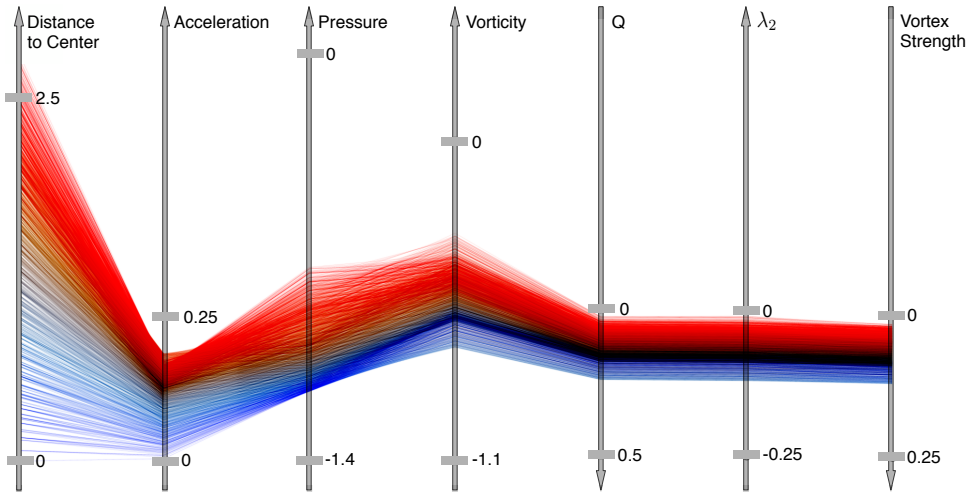

(c) Single region of the mixing layer

Figure 5.31 Parallel coordinate plot of a set of sample points on the vortex skeleton of the mixing layer (a), and the jet (b), and a single representative region of the mixing layer (c). The color of the lines is chosen by the vortex strength measure (a,b), or the distance to the vortex core the region is associated to (c). For a better visual perception the quantities are scaled, shifted and mirrored – as indicated by the gray bars. For all plots, vorticity, λ_2, Q and the vortex strength measure show very similar behavior and, thus, contain redundant information.

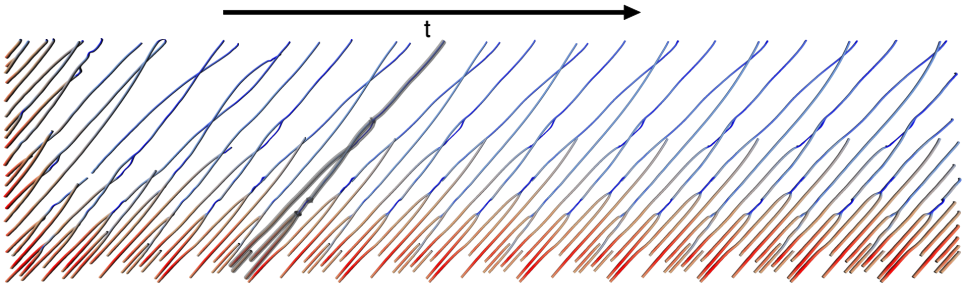

Figure 5.32 Vortex merge graph of the mixing layer dataset extracted from the acceleration magnitude. The time goes from left to right and the flow from bottom to top. Both, radius and color of the depicted vortex cores depend on the vorticity magnitude: low and high vorticity correspond to blue/thin and red/thick, respectively.

optionally shows the area of the associated vortex region. This helps to identify correspondence between the development of a quantity and the size of the vortex region.

5.5.2 Results

The data set that is considered for our analysis is a two-dimensional mixing layer, cf. Appendix A.7.

Figure 5.32 shows the vortex merge graph of this data set that is extracted using the acceleration magnitude as a feature identifier. The tracking result is the same as in Figure 5.19. In this figure, a selected subgraph is depicted that serves as a reference for the further analysis.

To investigate the behavior of other flow quantities on the merge graph, these quantities are sampled along the complete vortex skeleton and plotted as parallel coordinates in Figure 5.31 (a). The coloring of the lines is determined by the vortex strength measure. The coordinate axes were scaled to provide a good visual perception of the correspondences. The acceleration magnitude is zero along the vortex core lines. As expected, vorticity, Q, λ_2, and the vortex strength measure exhibit very similar behavior on the lines. In Figure 5.31 (b), we validated this correspondence with the data set of a jet, cf. Appendix A.9. The merge graph for this data set was already shown in Figure 5.21. Due to the strong correlation of theses quantities, we restrict the further analysis to vorticity, pressure, λ_2 and the acceleration magnitude.

To investigate the expected merge behavior, we analyzed more quantities on a circular disk before, during and after a merge event. Since Q and the vortex strength measure correlate with λ_2 in two-dimensional flows, we omitted these quantities. Together with the relative velocity and the pressure, the results are shown in Table 5.1. We added the vortex regions identified by the

	Pre-merged	Just merged	Merged
Acc.	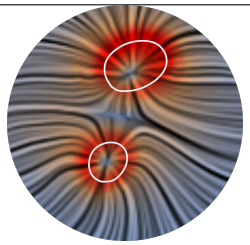	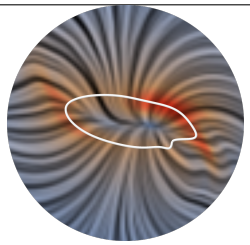	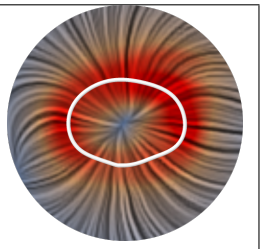
Rel. Velo.	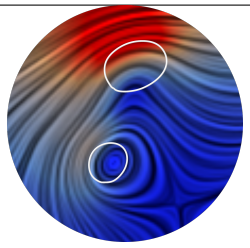	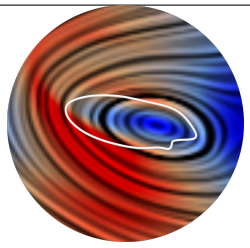	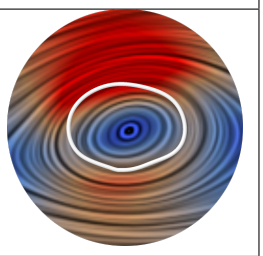
Vort.	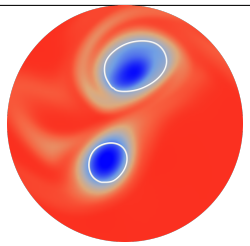	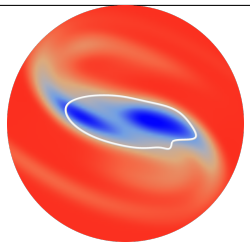	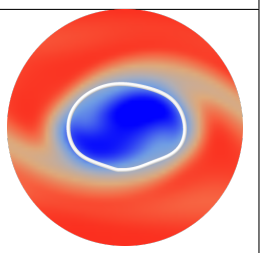
λ_2	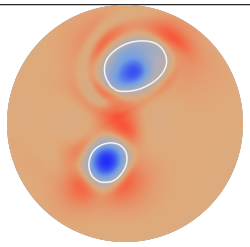	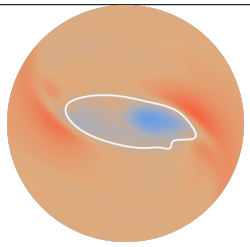	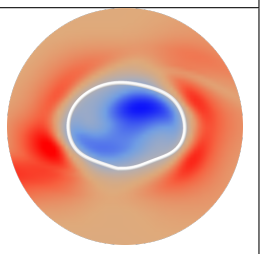
Press.	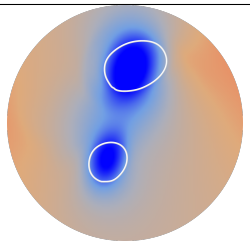	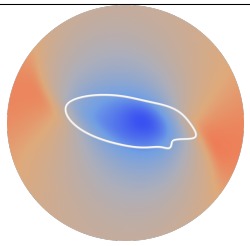	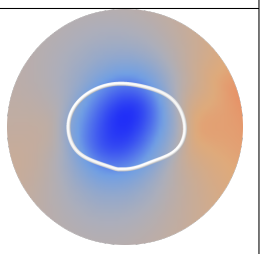

Table 5.1 Comparison of different quantities at different stages of a merge event. Note that for the relative velocity, the correct frame of reference is only indicated for one vortex.

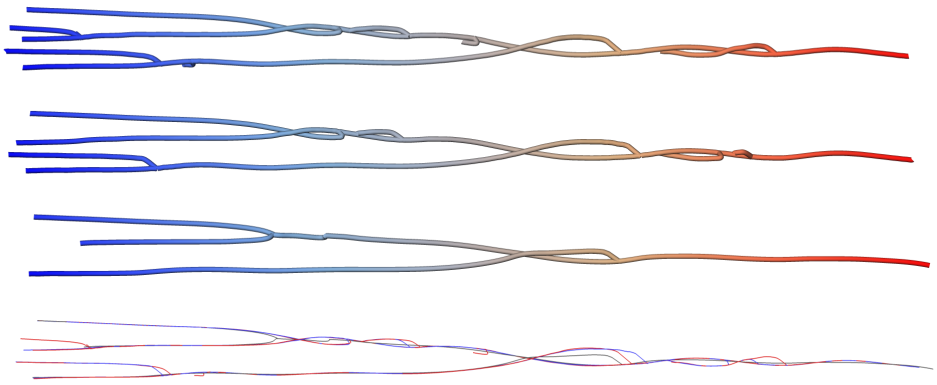

Figure 5.33 Vortex cores extracted from different feature identifiers: λ_2 (first, bottom red), vorticity (second, bottom blue) and acceleration magnitude (third, bottom grey). The location of these vortex cores is depicted in Figure 5.32. The color of the top vortex graphs depends on the time. The merge points in time differ significantly between acceleration and the other two quantities. Vorticity and λ_2 coincide most of the time.

acceleration as white lines. It can be seen that vorticity and λ_2 still reveal two clearly distinguishable extremal values, while the pressure and the acceleration magnitude just show a single vortex. The time of the merge events of the vortices is different for these quantities. This seems to be a typical difference of these two feature identifiers – we checked this behavior for other merge events and data sets. Note that there is no common frame of reference for the two merging vortices as indicated by the relative velocity.

In a next step, we compare vortex cores resulting from different scalar measures. From the set of merging vortex cores, we picked one vortex at the end of the data set and computed all connected vortices that merge onto this vortex. The results based on acceleration minima, λ_2, and vorticity are shown in Figure 5.33. Three interesting observations can be made: First, it is confirmed that in the acceleration magnitude the vortex core lines merge earlier than in the other two quantities. The core lines differ significantly between these two types of quantities. Second, outside the merge windows, all three vortex core lines coincide completely. While this behavior is expected for vorticity and λ_2, we did not await this for the acceleration magnitude. Third, at the merge windows, the vortex core lines of vorticity and λ_2 coincide until the actual merge event. There, the core lines differ slightly. This could be an effect of the persistence simplification. Note that it is not possible to use the same persistence threshold for different quantities. Thus, due to these different thresholds, the extremal points that represent the vortex core line are cancelled earlier in the one quantity than in the other. Thus, the merge is detected earlier. In

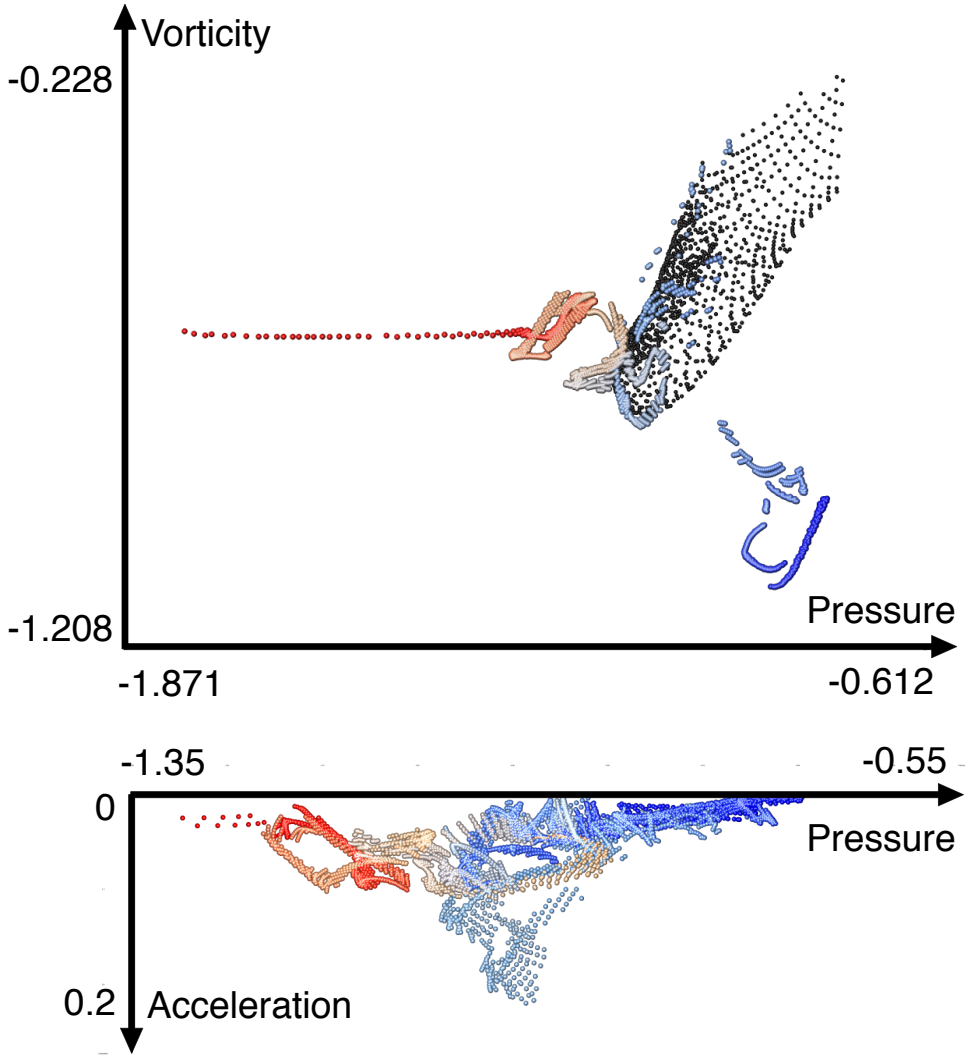

Figure 5.34 Scatter plot of the pressure compared to the vorticity (top) and the acceleration (bottom) sampled along the vortex merge graph extracted from the acceleration magnitude (top) and the vorticity (bottom). The coloring indicates time.

addition, for vorticity and λ_2 split after the merge event in contrast to the core lines extracted from the acceleration magnitude, which is represented by the L-shaped core lines.

To compare the vorticity with the acceleration magnitude, we plotted the different quantities along the selected vortex cores of Figure 5.33 as scatter plots against the pressure in Figure 5.34. The coloring of the points is determined by the time. To the top image, we added a scatter plot of the same quantities on a vortex region in the middle of the graph. While in both images

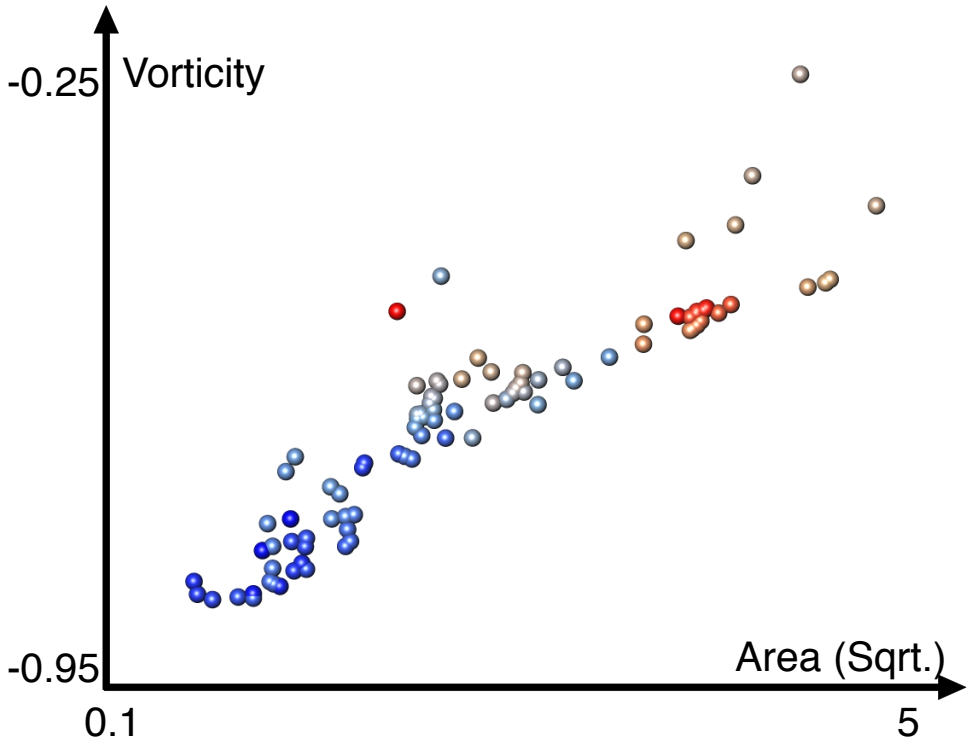

Figure 5.35 Scatter plot of the mean of the vorticity in a vortex region compared to its size. The measures are sampled along the merge graph identified by the acceleration magnitude. The coloring indicates the time.

the pressure decreases with time, the other quantities show different behavior. In the top image, the vorticity increases with time and is nearly constant after the last vortex merge. During the merge events, there is a chaotic behavior of the vorticity. The black dots indicating the behavior on a representative vortex region reveal that the vorticity and the pressure are significantly higher within the region than at the vortex core. Note that vorticity is negative here.

As a next step, we analyze the behavior of vorticity in the vortex region. We plotted the mean value of the vorticity against the square root of the area of the associated vortex region along the vortex merge graph identified by the acceleration magnitude as selected in Figure 5.33. The resulting scatter plot, see Figure 5.35, suggests a linear correspondence between these measures.

Finally, we used our analysis tools with the two selected merge graphs. Figure 5.36 shows the plot of a sampling of the acceleration magnitude on a circular disk along the vorticity graph. We removed the L-shaped vortex cores from the vorticity graph for these images, since they would result in an confusing segmentation. Figure 5.37 shows the plot of the sampling of the vorticity on the vortex regions along the acceleration graph. Comparing

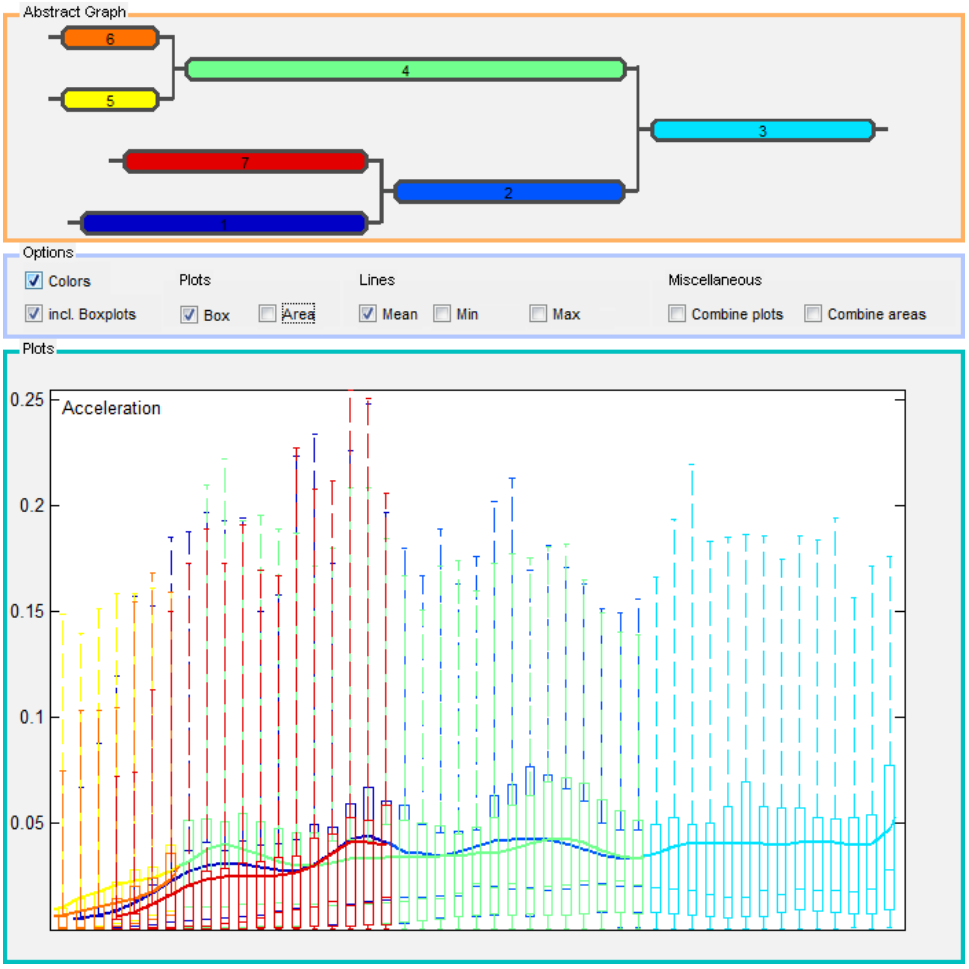

Figure 5.36 Analysis of the vortex merge graph indicated by the vorticity. The acceleration magnitude in a circular region of size 17 is sampled along the graph and indicated by box plots at the bottom. In addition, the mean value of the acceleration is shown as a thick line. The coloring at the bottom corresponds to the color of the segments of the merge graph at the top.

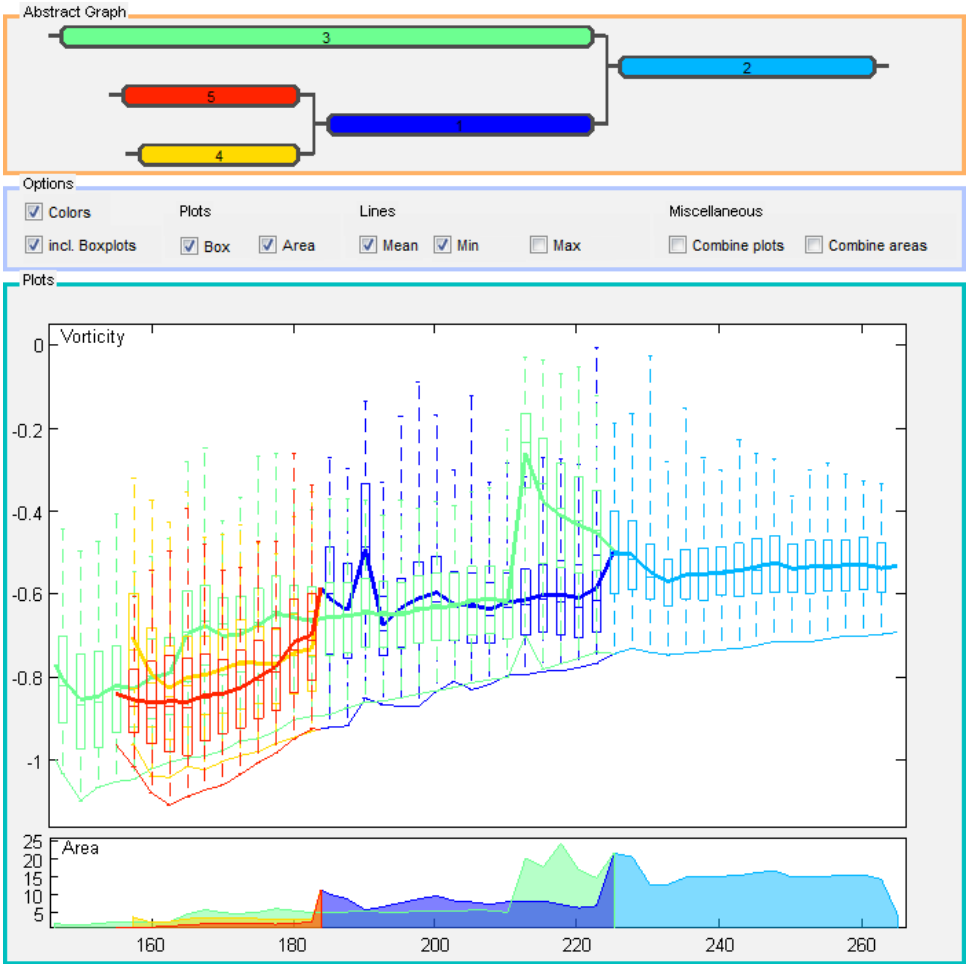

Figure 5.37 Analysis of the vortex merge graph indicated by the acceleration magnitude. The vorticity is sampled in the vortex regions along the graph and indicated by box plots in the center. In addition, the mean value of the voriticity is shown as a thick line. The coloring at the bottom corresponds to the color of the segments of the merge graph at the top. The area of the vortex regions is plotted at the bottom.

the abstract merge graphs in the top of both images, the different temporal merge points can be seen again. Outside the influence of a vortex merge, the mean of the vorticity and the area of the vortex region stay relatively constant along the acceleration graph. The minimal values of the vorticity increase a bit. Within the merge window, both the mean of the vorticity and the area increase drastically. Along the vorticity merge graph, the mean of the acceleration constantly grows, but stays nearly constant after the last merge. The minimum value is always zero.

5.5.3 Discussion

In this section, we compared the vortex merge graphs extracted from the acceleration magnitude with the ones extracted form vorticity and λ_2. We selected appropriate statistical tools that revealed interesting properties: First, the exact moment in time of a merge event depends on the type of the vortex identifier. Second, outside the vortex merge window, the vortex cores of the different quantities typically coincide. Third, there are vortex cores that merge in the one quantity, but not in the other. Fourth, some of the feature identifiers show very similar behavior along vortices.

Regarding the usability of the acceleration magnitude as a vortex identifier, we found that it typically corresponds to other identifiers. However, at the merge points, the behavior is significantly different to vorticity and λ_2. There, the acceleration magnitude correlates more with pressure. The regions extracted using acceleration again correspond well with different vortex identifiers. Even for vorticity and λ_2 in a merge window, the shape of the vortex region is similar to the shape of the iso contours of these quantities.

Chapter 6

Conclusion and outlook

In this thesis, we have described methods to analyze two-dimensional time-dependent flow fields. In this setting, the search for Lagrangian coherent structures (LCSs) plays a fundamental role. Thereby, LCSs are typically related to vortices on the one hand, or distinguished manifolds of particle divergence and convergence on the other hand. We have contributed concepts and algorithms for both of these structures. Ridges of FTLE fields are typically used to identify LCS. We have provided a new computation method and analyzed the applicability of FTLE to complex flow fields. In the case of vortices, we have introduced robust algorithms to extract them and their regions of influence based on the acceleration magnitude. These approaches also include a hierarchy for the resulting structures. Thus, with the tools that are provided in this thesis, we are able to extract LCSs by either FTLE or LEPs. Using the acceleration magnitude to define vortex regions, we have also encountered an interesting connection between the vortex regions and the FTLE ridges.

Another focus of recent work in the field of flow visualization is the transfer of velocity field topology to time-dependent flow fields. While ridges of the FTLE field are interpreted as time-dependent counterparts of the separatrices, we have introduced the concept of Lagrangian equilibrium points (LEPs), which serve as time-dependent counterparts of the critical points. Again, both main parts of this thesis, i.e., FTLE and LEPs, contribute to this topic. In addition, with the localized FTLE and the concept of long-living features, we have based both concepts on local feature identifiers, which unifies the extraction of a time-dependent version of the topology.

With the presented concepts and algorithms, we have contributed to the field of scientific visualization as well as to the field of fluid mechanics. The algorithmic aspects include the fast implementation of L-FTLE, the extraction of the vortex merge graph and the vortex regions. The tools enable an efficient analysis of time-dependent flow fields. The physical aspects of this thesis entail the analysis of FTLE, the concept of LEPs, their spatiotemporal hierarchy, and their statistical analysis. They build the basis for a sensible extraction of flow

features.

In the following, we will summarize the individual contributions in detail and characterize open problems.

Finite-time Lyapunov exponent. We began the investigation of LCSs with an introduction to this topic. We have seen that the concept of LCSs is elusive. It is hard to find a commonly accepted definition. With FTLE, Haller gave a well-defined framework to detect LCSs in time-dependent flow fields. We have introduced a new computation method for the FTLE field. In contrast to the flow map approach, which also highlights separation due to far away effects that are not linked to the trajectory of a particle, the new local approach based on the Jacobian focusses on the separation along the trajectory of a single particle. In addition to the new computation method for FTLE, a fast algorithm has been presented that is based on the idea of reusing path line segments. While we have only dealt with two-dimensional flows in this thesis, the localized FTLE method can be transferred to three-dimensional flows in a straightforward way. Recently, Kuhn et al. [KRWT12] proposed benchmark examples for analyzing different FTLE methods. In their results, they stated that our new approach yields better results than the classical version, in particular for long integration times and high resolutions of the FTLE field. In the analysis of Section 4.3, we have seen that FTLE still has problems with the analysis of complex flow fields. While the FTLE can be considered as a good realization of LCSs, the amount of structures often complicates a proper analysis of the underlying flow.

While we have achieved forthcomings in the analysis of time-dependent fields using the FTLE, there are still open and challenging questions. Regarding the methods presented in this thesis, we identified the following.

- The localized FTLE method relies on the Jacobian of the vector field. While we did not experience any problems using derivatives based on finite differences, a higher order interpolation could improve the calculation accuracy.

- The performance of the L-FTLE approach might be improved by using adaptive grids. The FTLE only has to be computed there, where large values occur. Thereby approaches of Sadlo et al. [SP07] or Garth et al. [GGTH07] can be transferred. Since the computation of L-FTLE is based on tracing a single path line, the implementation is less difficult.

- The L-FTLE approach samples the Jacobian along a path line in discrete steps with distance Δt. This parameter should be chosen as large as possible while still showing accurate results. An adaptive choice in combination with the adaptive integration of the path line could improve the performance.

- The FTLE does not discriminate between separation that occurs due to actual path line divergence or due to shear. Pobitzer et al. [PPF+11] investigated an approach to differentiate between these effects when using the flow map to compute the FTLE. They therefore analyzed the shear behavior along the trajectory of the particle the FTLE is computed for. Since L-FTLE is based on the computation of a single path line per value, we think that a combination of both approaches yields a more consistent method.

- We have seen that the FTLE is hard to interpret for complex data sets, since it results a lot of in-differentiable structures. A hierarchy for FTLE ridges might help to handle the large amount of detected features. As a first step, separatrix persistence as proposed by Weinkauf and Günther [WG09] has been applied to a data set of a cylinder [KWP+10]. It should be investigated if this concept can be combined with a feature lifetime similar to the concept of integrated persistence used as a hierarchy for vortex core lines.

Acceleration. A new set of features has been defined as minima of the acceleration magnitude. Besides incorporating a Lagrangian viewpoint, they exhibit a certain kind of equilibrium for particles. We therefore call this concept Lagrangian equilibrium points. Independently, Goto and Vassilicos [GV06] proposed to use zeros points of the acceleration vector field (ZAPs). In addition to defining these points in a vector field context, which complicates a robust extraction, the minima of the acceleration entail a wider range of features. Elaborate methods of scalar field topology can be applied. The concept is easily transferable to three-dimensional flows. There, it is not clear if zeros of the acceleration either occur or represent a set of interesting features.

We were able to show that the LEPs can be used as time-dependent counterparts of the critical points – representing centers as well as saddles. Note that ridges of the FTLE field are often used as time-dependent counterparts of separatrices of velocity field topology, e.g., cf. Sadlo et al. [SW10]. Therefore, these concepts complement each other and they can be interpreted a first building block of a finite time version of velocity field topology.

A subset of the LEPs corresponds to vortex cores. Their regions of influence can be extracted in the same topological context. We have employed robust methods to extract the vortex core lines and vortex regions in time-dependent flow fields. A statistical analysis has revealed that the acceleration is a good observable to extract vortices, but also some differences to known quantities were disclosed.

Note that there is no commonly accepted mathematical definition of a vortex and not even a set of axioms such a definition should obey. Hence, which of the vortex indicators is *correct* cannot be said. Due to the large variety

of applications and research questions in engineering and fluid flow research, a single definition might be unwanted. The algorithmic and analysis tools presented in this thesis can also be applied to other quantities. They allow to analyze the different outcomes due to different vortex indicators and, maybe, help to select the appropriate one depending on the application.

As future work, there are some ideas that could be investigated to improve the methods presented in this thesis. These entail conceptual as well as algorithmic questions:

- For the classification of the LEPs, we have been using the Jacobian in analogy to the classification of the critical points of velocity field topology. However, we have seen that Lagrangian quantities such as acceleration show different behavior than pure spatial quantities, e.g., λ_2 as based on the Jacobian. Thus, a classification that incorporates the temporal domain might result in a more consistent extraction.

- We have focussed on a subset of the LEPs that represent vortices. Similar approaches could be developed for saddle points.

- The definition of the vortex core lines and their associated regions based on the topological skeleton of the acceleration magnitude can in principle be transferred to three dimensions. It seems sensible that in three dimensions vortex core lines are described by the minima lines of the acceleration magnitude and the vortex cores regions are given by the associated basins of the minima. Anyhow, the topological framework to track these structures in three dimensional flows has to be investigated in the context of CFFF.

- We have defined an importance measure for the unique vortex core lines. This makes it possible to differentiate between individual vortex core lines. Spatially important and long-living features can be distilled. At the merge windows, no importance measure is defined. A single measure for all connected components of a vortex may be interesting.

- Currently, one limitation of the CFFF approach is that the persistence threshold has to be chosen before the actual tracking. This makes persistence a potentially problematic parameter. If the persistence threshold of the vortex merge graph could be chosen after the tracking, this would improve an interactive analysis of the vortex structures.

- The persistence threshold has a deep impact on the shape of the regions at the vortex merge windows. A further investigation of the vortex regions is needed at these points.

- As stated by Reininghaus et al. [Rei12], the geometrical embedding of the combinatorial stream lines does not always follow the actual analytically

defined stream lines of a given data set. For combinatorial scalar field topology, the stream lines are alright, if the ridge is well pronounced, which is the case for the boundaries of the vortex regions described in Section 5.4. Therefore, this limitation is not that problematic. However, an improvement of the geometrical embedding would improve the shape of the vortex regions – especially for data sets given on regular grids.

- In Section 5.4, we have seen that the vortex regions based on the acceleration magnitude correspond quite well to ridges of the backward FTLE field. An investigation of this correlation could improve the understanding of both quantities.

Appendix A

Data sets

Several flow data sets are used to evaluate the different feature definitions and algorithms proposed in this thesis. An overview of the data sets and their generation is given in the following.

A.1 Oseen vortices

The *Oseen vortex* models a free vortex, i.e., the tangential velocity behaves inverse to the distance from the center. It decays due to viscosity. The velocity V_Θ in the circumferential direction θ is given by

$$V_\Theta(r) = \frac{\Gamma}{2\pi} \frac{1 - e^{-(\frac{r}{r_c})^2}}{r}, \tag{A.1}$$

where r is the spatial coordinate with origin in the center of the vortex, r_c is a parameter determining the core radius and the parameter Γ the circulation contained in the vortex. For further information we refer to Rom-Kedar et al. [RKLW90] or Noack et al. [NMTB04].

We used two data sets based on a mixing of Oseen vortices. Note that the velocity of the individual vortices is induced by the other vortices in the flow. This corresponds to the law of Biot-Savart.

Two co-rotating Oseen vortices

The first data set is a pair of two co-rotating Oseen vortices. In this data set, r_c is typically chosen as 0.5 and Γ as 2π. They rotate around the origin at constant distance $R = 1/\sqrt{2}$ with uniform angular velocity Ω. Let $\mathbf{x}_i = (x_i, y_i)$, $i = 1, 2$ be the centers of the two vortices. Then,

$$\begin{aligned} x_1 &= \quad R\,\cos\Omega t, \qquad y_1 = R\,\sin\Omega t, \\ x_2 &= -R\,\cos\Omega t, \qquad y_2 = -R\,\sin\Omega t. \end{aligned} \tag{A.2}$$

The velocity of each vortex corresponds to the induced velocity, cf. Equation (A.1), i.e. $R\Omega = u_\theta(2R)$.

Mixing of six Oseen vortices

This data set is described by an random mixing of six Oseen vortices. Their core radius is chosen in that way that they interact with each other.

A.2 Stuart vortices

The analytic *Stuart vortex model* represents a two-dimensional time-dependent flow with elliptical convecting vortices moving from left to right with the medium velocity of the flow field. The model can be interpreted as a simple streamwise periodic version of a shear layer, i.e. the velocity is lower in the upper half than in the lower half [Stu67]. The flow is analytically defined as

$$\begin{aligned} u(\mathbf{x},t) &= \frac{\sinh(2\,x_2)}{\cosh(2\,x_2) - 0.25 \cdot \cos(2(x_1 - t))} + u_c \\ v(\mathbf{x},t) &= -\frac{0.25\ \cdot\ \sin(2(x_1 - t))}{\cosh(2\,x_2) - 0.25 \cdot \cos(2(x_1 - t))}, \end{aligned} \tag{A.3}$$

where u_c represents the convection velocity. If not stated otherwise, it is set to $u_c = 1$. It is a periodic flow with a temporal period of $T = \pi$.

A.3 Lundgren vortex

The *Lundgren vortex model* [Lun82] is an example for a non-circular basic vortex. It also is a solution of the Navier-Stokes equations. Lundgren has shown that solutions of the two-dimensional Navier-Stokes equations can be lifted to three dimensions using the Lundgren transformation. In his publication, he used this vortex as an example. I thank Oliver Kamps (University of Münster) for providing this data set

A.4 Cylinder I

The first *cylinder data set* is a time-dependent two-dimensional CFD simulation of the von-Kármán vortex street [NSA+08, Wil96], the flow behind a cylinder with $Re = 100$. This is well above the critical value for vortex shedding at 47 [Zeb87, Jac87] and well below the critical value for transition-related instabilities around 180 [ZFN+95, Wil96]. The data set consists of 32 time steps. The flow is periodic, allowing a temporal unbounded evaluation of the field.

A.5 Cylinder II

The second *cylinder data set* is also a time-dependent two-dimensional CFD data set showing the von-Kármán vortex street. This flow is simulated with a finite-element method solver with third-order accuracy in space and time, like in [NAM+03]. The rectangular computational domain $(x, y) \in [-10, 30] \times [-15, 15]$ without the disk $K_{1/2}(0)$ for the cylinder is discretized by 277,576 triangular elements. The resolution of this data set is much finer than the above one. The numerical time step is 0.1, which also corresponds to the sampling frequency for the snapshots.

A.6 Cavity

The *cavity data set* is a time-dependent simulation of the flow over a two-dimensional cavity [CSD03] using the compressible Navier-Stokes equations. It consists of 1000 time steps and is nearly periodic.

A.7 Mixing layer

The *mixing layer* data set represents a shear flow with a velocity ratio between upper and lower stream of 3:1 [CSB98, NPT+04, NPM05]. The inflow is described by a tanh profile with a stochastic perturbation. The Reynolds number based on maximum velocity and vorticity thickness is 500. The flow is computed with a compact finite-difference scheme of 6th order accuracy in space and 3rd oder accuracy in time. The computational domain $(x, y) \in [0, 140] \times [-28, 28]$ is discretized on a 960×384 grid. The sampling time for the employed snapshots is $\Delta t = 0.05$ corresponding $1/10$ of the computational time step.

A.8 Jet I

This data set represents a turbulent, non-periodic flow [LMC05, CDB+98]. It is generated from a three-dimensional time dependent large eddy simulation of a *jet*. It consists of about 6000 time steps.

A.9 Jet II

The second *jet* data set is a two-dimensional time-dependent flow. It shows a number of vortex mergers leading to a reduction of the characteristic fre-

quency. The convection velocity of these vortices is not constant but decreases in streamwise direction.

All quantities are normalized with the jet width D_j and maximum jet velocity U_j. The flow is a weakly compressible isothermal 2D jet with a Mach number of $Ma_j = 0.1$ and a Reynolds number of $Re_j = D_j U_j / \nu_\infty = 500$. The inflow velocity profile is given by a hyperbolic tangent profile like in [Fre01]:

$$u(r) = U_\infty + \frac{(U_j - U_\infty)}{2}\left[1 - \tanh\left[b\left(\frac{r}{r_0} - \frac{r_0}{r}\right)\right]\right]. \tag{A.4}$$

Here, a uniform 1% co-flow $U_\infty = 0.01 U_j$ is added to avoid vortices with arbitrarily long residence time in the computational domain. The slope of the tanh profile is characterized by $b = r_o/4\delta_\theta$ and the momentum thickness of the shear layer is $\delta_\theta = 0.05 r_o$. The initial mean temperature was calculated with the Crocco-Busemann relation, and the mean initial pressure was constant.

The natural transition to unsteadiness is promoted by adding disturbances in a region in the early jet development near the inflow boundary $x_o = -0.5$:

$$v(x,y) = v(x,y) + \alpha U_c e^{-\frac{(x-x_o)^2}{\lambda_x^2}}(f_1(y) + f_2(y)) \tag{A.5}$$

Here,

$$f_1(y) = \epsilon_1 e^{-\frac{(y-y_1)^2}{\lambda_y^2}}, \qquad f_2(y) = \epsilon_2 e^{-\frac{(y-y_2)^2}{\lambda_y^2}}, \tag{A.6}$$

where $U_c = 0.5$, $\alpha = 0.008$, $y_1 = 0.5$, $y_2 = -0.5$, $\lambda_x = 0.1$, $\lambda_y = 0.1$ and $-1 \leq \epsilon_1, \epsilon_2 \leq 1$ are random numbers.

The flow is defined in a rectangular domain $(x, y) \in [0, 20] \times [-7, 7]$. The adjacent sponge zone extends to $[-1.5, 25] \times [-10, 10]$. The whole domain is discretized on a non-uniform Cartesian with 2 449 points in x-direction and 598 points in y-direction. The compressible Navier-Stokes equation is solved by mean of a (2,4) conservative finite-difference scheme based on MacCormack's predictor-corrector method [GT76] with block-decomposition and MPI parallelization. The system may be closed by the thermodynamic relations for an ideal gas. Details of the equations, boundary conditions and solver can be inferred from [CDC+11].

A.10 Acknowledgement

I want to thank Oliver Kamps for providing the Lundgren data set, Gerd Mutschke for providing the first cylinder data set, Marek Morzyński for providing the second cylinder data set, Mo Samimy for providing the cavity data set, Pierre Comte for providing the first jet and the mixing layer data set, and Guillaume Daviller and Pierre Comte for providing the second jet data set.

Appendix B

Gallery of fluid motion

The *Gallery of fluid motion* is an annual contest organized by the Division of Fluid Dynamics (DFD) of the American Physical Society (APS). There, researchers exhibit outstanding visualizations and photographs of computational and experimental data sets. Every year, a few of these submission are awarded.

During the development of the work presented in this thesis, three prominent visualizations were submitted to this contest. By this means, we were able to arouse interest in our work in the community of fluid mechanics. In the following, the three submissions are depicted.

B.1 Lagrangian feature extraction of the cylinder wake

Awarded

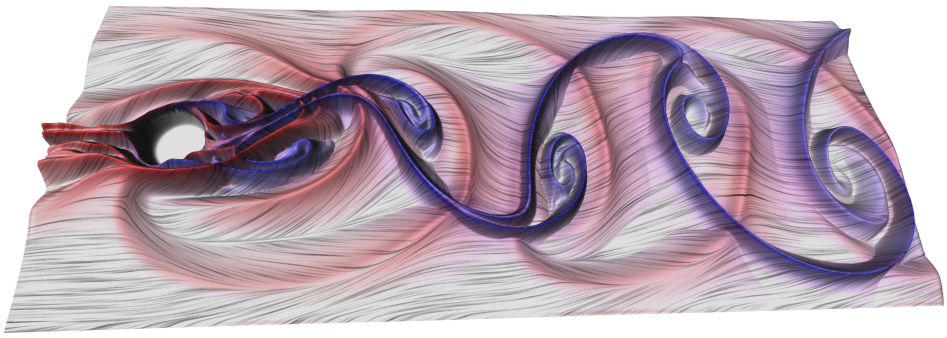

We extract Lagrangian features of the 2-D von Kármán vortex street behind a circular cylinder. The temporal convergence and separation of particles is monitored over two shedding periods. This behavior is quantified by the distance of nearby particles during this time window. The Finite Time Lyapunov Exponent (FTLE) [Hal01b] measures the logarithm of the maximum distance of these nearby particles. We compute the FTLE based on the first variational form [KPH+09], i.e., integrating a locally linear flow.

In the image, red coloring indicates regions of particle divergence in forward time. Blue regions show convergence (divergence in backward time). The height of the grey surface represents the maximum of both corresponding FTLE values. The direction of the flow field is indicated by lines on the surface.

The intersections of both curves mark high separation on the one side and high convergence on the other side. These points are interpreted as a Lagrangian version of saddle points from topology [Hal01a]. Furthermore, the ridges of the FTLE build attractive and separating invariant manifold "arms" that mark domains of particle attraction and separation. Thus, the mixing of the von Kármán vortex street is characterized by the Lagrangian saddle points and the corresponding domains.

B.2 Flow over a cavity – evolution of the vortex skeleton

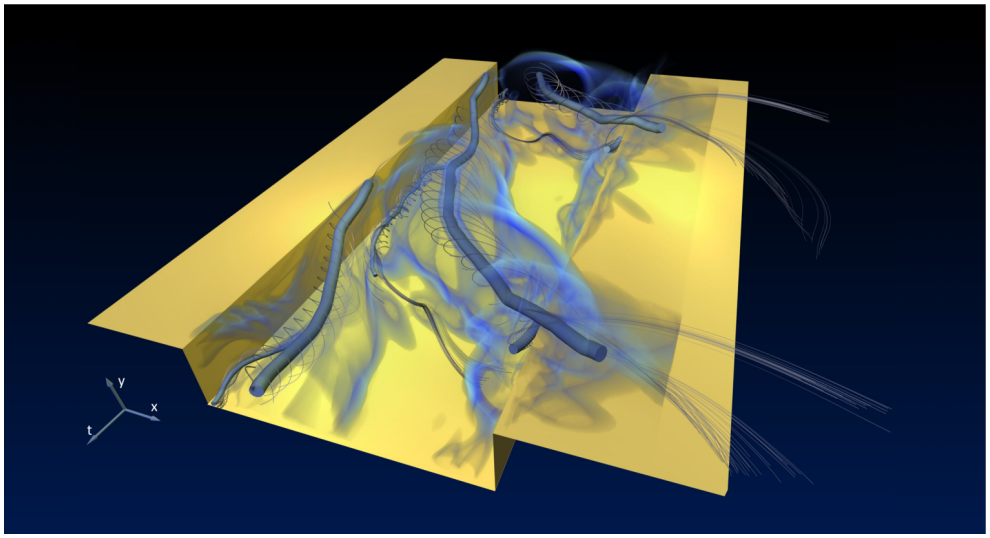

We consider a numerical simulation of a weakly compressible 2D flow over a cavity at $Ma = 0.36$ (courtesy: M. Samimy). The flow over the cavity (yellow) is from left to right, the time is represented by the third dimension. Focus is placed on the temporal evolution of the vortices. These vortices (blue vortex cores) are identified as minima of the acceleration magnitude following feature extraction concept of finite-time topology [KHNH11]. The spiraling curves represent fluid particle paths in the vortical regions. The volumetric smoke-like regions indicate a range of large acceleration magnitudes. The vortices originate at the leading edge and move through the cavity over the trailing edge. The halo of each vortex consists of spiraling particles with large acceleration values.

B.3 Incompressible jet – temporal evolution of the vortex skeleton

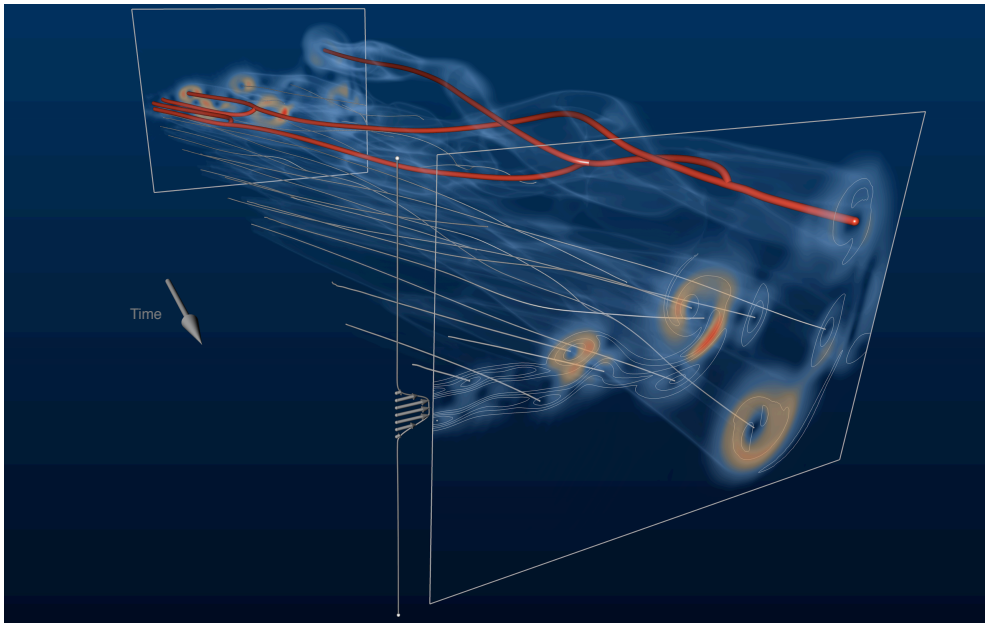

A viscous two-dimensional jet flow is visualized employing a direct numerical simulation at Reynolds number 500 and $Ma = 0.1$. The flow direction is from left to right. The time is represented by the third dimension pointing towards the viewer. Our focus is the extraction of the vortex skeleton including vortex mergers in time. The evolution of the vortex skeleton is depicted by gray lines. A successive merger of three vortices is emphasized by the thick red curves. The vortex cores are identified by local minima of the material acceleration magnitude and positive Q-values [KHNH11]. Regions of significant particle acceleration are indicated by the blue smoke. In the front plane, this acceleration magnitude is color-coded, red regions denoting higher values than blue ones. In addition, vorticity iso-levels are added, demonstrating that vorticity maxima and acceleration minima effectively coincide.

Bibliography

[BM10] A. Bracco and J. C. McWilliams. Reynolds-number dependency in homogeneous, stationary two-dimensional turbulence. *Journal of Fluid Mechanics*, 646:517–526, 2010.

[BPSS02] D. Bauer, R. Peikert, M. Sato, and M. Sick. A case study in selective visualization of unsteady 3D flow. In *Proceedings IEEE Visualization 2002*, pages 525–528, 2002.

[BR74] G. L. Brown and A. Roshko. On density effects and large structures in turbulent mixing layers. *Journal of Fluid Mechanics*, 64(4):775 – 816, 1974.

[BS95] David C. Banks and Bart A. Singer. A predictor-corrector technique for visualizing unsteady flow. *IEEE Transactions on Visualization and Computer Graphics*, 1(2):151–163, 1995.

[BSS02] C. Bajaj, A. Shamir, and B.-S. Sohn. Progressive tracking of isosurfaces in time-varying scalar fields. Technical Report TR-02-4, Department of Computer Sciences & TICAM, University of Texas Austin, 2002.

[BWP+10] P.-T. Bremer, G. H. Weber, V. Pascucci, M. Day, and J. B. Bell. Analyzing and tracking burning structures in lean premixed hydrogen flames. *IEEE Transactions on Visualization and Computer Graphics*, 16(2):248–260, 2010.

[CDB+98] P. Comte, Y. Dubief, C. Bruni, M. Meinke, C. Schultz, and T. Rister. Simulation of spatially developing plane and round jets. *Notes on Numerical Fluid Mechanics*, 66:301 – 319, 1998.

[CDC+11] A. V. G. Cavalieri, G. Daviller, P. Comte, P. Jordan, G. Tadmor, and Y. Gervais. Using large eddy simulation to explore sound-source mechanisms in jets. *Journal of Sound and Vibration*, 330(17):4098–4113, 2011.

[CJR07] J. Caban, A. Joshi, and P. Rheingans. Texture-based feature tracking for effective time-varying data visualizations.

IEEE Transactions on Visualization and Computer Graphics, 13(6):1472–1479, 2007.

[CKL10] M. Chertkov, I. Kolokolov, and V. Lebedev. Universal velocity profile for coherent vortices in two-dimensional turbulence. *Physical Review E*, 81(1):015302, 2010.

[CL84] E. A. Coddington and N. Levinson. *Theory of Ordinary Differential Equations*. McGraw Hill, 1984.

[CL93] B. Cabral and L. C. Leedom. Imaging vector fields using line integral convolution. In *Proceedings ACM SIGGRAPH 1993*, pages 263–270, 1993.

[CM93] A. Chorin and J. E. Marsden. *A Mathematical Introduction to Fluid Mechanics*. Springer Verlag, 3 edition, 1993.

[CSB98] P. Comte, J. H. Silvestrini, and P. Bégou. Streamwise vortices in large eddy simulations of mixing layer. *European Journal of Mechanics B*, 17:615–637, 1998.

[CSD03] E. Caraballo, M. Samimy, and J. DeBonis. Low dimensional modeling of flow for closed-loop flow control. In *Proceedings AIAA Meeting 2003*, volume 59, 2003.

[DLL+10] T. K. Dey, K. Li, C. Luo, P. Ranjan, I. Safa, and Y. Wang. Persistent heat signature for pose-oblivious matching of incomplete models. *Computer Graphics Forum*, 29(5):1545–1554, 2010.

[dLvL01] W. de Leeuw and R. van Liere. Chromatin decondensation: A case study of tracking features in confocal data. In *Proceedings IEEE Visualization 2001*, pages 441–444, 2001.

[Ebe96] David Eberly. *Ridges in Image and Data Analysis*. Springer Verlag, 1996.

[EH04] H. Edelsbrunner and J. Harer. Jacobi sets of multiple Morse functions. In *Foundations of Computational Mathematics*, pages 37–57. Cambridge University Press, 2004.

[EH08] H. Edelsbrunner and J. Harer. Persistent homology — a survey. *Surveys on Discrete and Computational Geometry: Twenty Years Later*, 458:257–282, 2008.

[EHM+08] H. Edelsbrunner, J. Harer, A. Mascarenhas, J. Snoeyink, and V. Pascucci. Time-varying Reeb graphs for continuous space-time data. *Computation Geometry: Theory and Applications*, 41(3):149–166, 2008.

[EHZ01] H. Edelsbrunner, J. Harer, and A. Zomorodian. Hierarchical morse complexes for piecewise linear 2-manifolds. In *Proceedings Symposium on Computational Geometry 2001*, pages 70–79, 2001.

[FCS04] J. M. Foucaut, J. Carlier, and M. Stanislas. PIV optimization for the study of turbulent flow using spectral analysis. *Measurement Science and Technology*, 15(6):1046, 2004.

[FKS+10] R. Fuchs, J. Kemmler, B. Schindler, J. Waser, F. Sadlo, H. Hauser, and R. Peikert. Toward a Lagrangian vector field topology. *Computer Graphics Forum*, 29(3):1163–1172, 2010.

[For98a] R. Forman. Combinatorial vector fields and dynamical systems. *Mathematische Zeitschrift*, 228(4):629–681, 1998.

[For98b] R. Forman. Morse theory for cell complexes. *Advances in Mathematics*, 134:90–145, 1998.

[For01] R. Forman. A user's guide to discrete Morse theory. In *Proceedings International Conference on Formal Power Series and Algebraic Combinatorics 2001*, 2001.

[FPH+08] R. Fuchs, R. Peikert, H. Hauser, F. Sadlo, and P. Muigg. Parallel vectors criteria for unsteady flow vortices. *IEEE Transactions on Visualization and Computer Graphics*, 14(3):615–626, 2008.

[FPS+08] R. Fuchs, R. Peikert, F. Sadlo, B. Alsallakh, and E. Gröller. Delocalized unsteady vortex region detectors. In *Proceedings Vision, Modeling and Visualization 2008*, pages 81–90, 2008.

[Fre01] J. B. Freund. Noise sources in a low Reynolds number turbulent jet at Mach 0.9. *Journal of Fluid Mechanics*, 438:277–305, 2001.

[FSK98] M. Farge, K. Schneider, and N. K.-R. Kevlahan. Coherent structure eduction in wavelet-forced two-dimensional turbulent flows. In *Proceedings IUTAM Symposium on Dynamics of Slender Vortices 1998*, 1998.

[FSP12] R. Fuchs, B. Schindler, and R. Peikert. Scale-space approaches to ftle ridges. In *Topological Methods in Data Analysis and Visualization II*, pages 283–296. Springer, 2012.

[GBHP08] A. Gyulassy, P.-T. Bremer, B. Hamann, and V. Pascucci. A practical approach to Morse-Smale complex computation: scalability and generality. *IEEE Transactions on Visualization and Computer Graphics*, 14:1619–1626, 2008.

[GBPH11] A. Gyulassy, P.-T. Bremer, V. Pascucci, and B. Hamann. Practical considerations in Morse-Smale complex computation. In *Topological Methods in Data Analysis and Visualization*, pages 67–78. Springer, 2011.

[GGTH07] C. Garth, F. Gerhardt, X. Tricoche, and H. Hagen. Efficient computation and visualization of coherent structures in fluid flow applications. *IEEE Transactions on Visualization and Computer Graphics*, 13(6):1464–1471, 2007.

[GLT+07] C. Garth, G.-S. Li, X. Tricoche, C. D. Hansen, and H. Hagen. Visualization of coherent structures in transient 2D flows. In *Topology-Based Methods in Visualization II*, pages 1–13. Springer, 2007.

[GNP+06] A. Gyulassy, V. Natarajan, V. Pascucci, P.-T. Bremer, and B. Hamann. A topological approach to simplification of three-dimensional scalar functions. *IEEE Transactions on Visualization and Computer Graphics*, 12(4):474–484, 2006.

[GNPH07] A. Gyulassy, V. Natarajan, V. Pascucci, and B. Hamann. Efficient computation of Morse-Smale complexes for three-dimensional scalar functions. *IEEE Transactions on Visualization and Computer Graphics*, 13:1440–1447, 2007.

[GOPT11] T. Germer, M. Otto, R. Peikert, and H. Theisel. Lagrangian coherent structures with guaranteed material separation. *Computer Graphics Forum*, 30(3):761–770, 2011.

[GRH07] M. A. Green, C. W. Rowley, and G. Haller. Detection of Lagrangian coherent structures in 3d turbulence. *Journal of Fluid Mechanics*, 572:111–12, 2007.

[GT76] D. Gottlieb and E. Turkel. Dissipative two-four method for time dependent problems. *Mathematics of Computation*, 30(136):703–723, 1976.

[GTS+04a] C. Garth, X. Tricoche, T. Salzbrunn, T. Bobach, and G. Scheuermann. Surface techniques for vortex visualization. In *Proceedings Joint EG - IEEE TVCG Symposium on Visualization 2004*, pages 155–164, 2004.

[GTS04b] C. Garth, X. Tricoche, and G. Scheuermann. Tracking of vector field singularities in unstructured 3D time-dependent datasets. In *Proceedings IEEE Visualization 2004*, pages 329–336, 2004.

[GV06] S. Goto and J. C. Vassilicos. Self-similar clustering of inertial particles and zero-acceleration points in fully developed two-dimensional turbulence. *Physics of Fluids*, 18(11):115103–1..10, 2006.

[Gyu08] A. Gyulassy. *Combinatorial Construction of Morse-Smale Complexes for Data Analysis and Visualization.* PhD thesis, University of California, Davis, 2008.

[Hal00] G. Haller. Finding finite-time invariant manifolds in two-dimensional velocity fields. *Chaos*, 10:99–108, 2000.

[Hal01a] G. Haller. Distinguished material surfaces and coherent structures in three-dimensional fluid flows. *Physica D*, 149:248–277, 2001.

[Hal01b] G. Haller. Lagrangian structures and the rate of strain in a partition of two-dimensional turbulence. *Physics of Fluids*, 13(11):3365–3385, 2001.

[Hal02] G. Haller. Lagrangian coherent structures from approximate velocity data. *Physics of Fluids*, 14:1851–1861, 2002.

[Hal05] G. Haller. An objective definition of a vortex. *Journal of Fluid Mechanics*, 525:1–26, 2005.

[Hat02] A. Hatcher. *Algebraic Topology.* Cambridge University Press, 2002.

[HH89] J. Helman and L. Hesselink. Representation and display of vector field topology in fluid flow data sets. *IEEE Computer*, 22(8):27–36, 1989.

[HH91] J. L. Helman and L. Hesselink. Visualizing vector field topology in fluid flows. *IEEE Computer Graphics and Applications*, 11(3):36–46, 1991.

[HKH11] H.-C. Hege, J. Kasten, and I. Hotz. Distillation and visualization of spatiotemporal structures in turbulent flow fields. In *Proceedings European Turbulence Conference (ETC13) 2011*, 2011.

[HLD02] H. Hauser, R. S. Laramee, and H. Doleisch. State of the art report 2002 in flow visualization, 2002.

[Hun87] J. C. R. Hunt. Vorticity and vortex dynamics in complex turbulent flows. *Transactions of the Canadian Society of Mechnical Engineering*, 11:21–35, 1987.

[Hus83] A. K. M. F. Hussain. Coherent structure – reality and myth. *Physics of Fluids*, 26(10):2816–2850, 1983.

[Hus86] A. K. M. F. Hussain. Coherent structures and turbulence. *Journal of Fluid Mechanics*, 173:303 – 356, 1986.

[Jac87] C. P. Jackson. A finite-element study of the onset of vortex shedding in flow past variously shaped bodies. *Journal of Fluid Mechanics*, 182:23–45, 1987.

[JH95] J. Jeong and A. K. M. F. Hussain. On the identification of a vortex. *Journal of Fluid Mechanics*, 285:69–94, 1995.

[Ji06] G. Ji. *Feature tracking and viewing for time-varying data sets*. PhD thesis, Ohio State University, 2006.

[JKJTM06] M. Jankun-Kelly, M. Jiang, D. Thompson, and R. Machiraju. Vortex visualization for practical engineering applications. *IEEE Transactions on Visualization and Computer Graphics*, 12(5):957–964, 2006.

[JSW03] G. Ji, H.-W. Shen, and R. Wenger. Volume tracking using higher dimensional isosurfacing. In *Proceedings IEEE Visualization 2003*, pages 209–216, 2003.

[KHH11] J. Kasten, I. Hotz, and H.-C. Hege. On the elusive concept of Lagrangian coherent structures. In *Topological Methods in Data Analysis and Visualization II*, pages 207 – 220. Springer, 2011.

[KHNH11] J. Kasten, I. Hotz, B.R. Noack, and H.-C. Hege. On the extraction of long-living features in unsteady fluid flows. In *Topological Methods in Data Analysis and Visualization*, pages 115–126. Springer, 2011.

[KHNH12] J. Kasten, I. Hotz, B. R. Noack, and H.-C. Hege. Vortex merge graphs in two-dimensional unsteady flow fields. In *Proceedings Joint EG - IEEE TVCG Symposium on Visualization – submitted*, 2012.

[KKM05] H. King, K. Knudson, and N. Mramor. Generating discrete Morse functions from point data. *Experimental Mathematics*, 14(4):435–444, 2005.

[KKM08] H. King, K. Knudson, and N. Mramor. Birth and death in discrete morse theoryorse theory. *arXiv:0808.0051v1*, 2008.

[KPH+09] J. Kasten, C. Petz, I. Hotz, B.R. Noack, and H.-C. Hege. Localized finite-time lyapunov exponent for unsteady flow analysis. In *Proceedings Vision, Modeling and Visualization 2008*, pages 265–274, 2009.

[KPH+10] J. Kasten, C. Petz, I. Hotz, H.-C. Hege, B.R. Noack, and G. Tadmor. Lagrangian feature extraction of the cylinder wake. *Physics of Fluids*, 22(9):091108 – 1, 2010.

[KRHH11] J. Kasten, J. Reininghaus, I. Hotz, and H.-C. Hege. Two-dimensional time-dependent vortex regions based on the acceleration magnitude. *IEEE Transactions on Visualization and Computer Graphics*, 17:2080–2087, 2011.

[KRWT12] A. Kuhn, C. Rössl, T. Weinkauf, and H. Theisel. A benchmark for evaluating FTLE computations. In *Proceedings IEEE Pacific Visualization 2012*, pages 121–128, 2012.

[KWP+10] J. Kasten, T. Weinkauf, C. Petz, I. Hotz, B. R. Noack, and H.-C. Hege. Extraction of coherent structures from natural and actuated flows. In *Active Flow Control II*, pages 373 – 387. Springer, 2010.

[LBM+06] D. Laney, P.-T. Bremer, A. Mascarenhas, P. Miller, and V. Pascucci. Understanding the structure of the turbulent mixing layer in hydrodynamic instabilities. *IEEE Transactions on Visualization and Computer Graphics*, 12(5):1053–1060, 2006.

[Lew05] T. Lewiner. *Geometric discrete Morse complexes*. PhD thesis, Department of Mathematics, PUC-Rio, 2005.

[LHD+04] R. S. Laramee, H. Hauser, H. Doleisch, B. Vrolijk, F. H. Post, and D. Weiskopf. The state of the art in flow visualization: Dense and texture-based techniques. *Computer Graphics Forum*, 23(2):203–221, 2004.

[LHZP07] R. S. Laramee, H. Hauser, L. Zhao, and F. H. Post. Topology-based flow visualization, the state of the art. In *Topology-Based Methods in Visualization*, pages 1–19. Springer, 2007.

[LMC05] M. Lesieur, O. Metais, and P. Comte. *Large-Eddy Simulations of Turbulence*. Cambridge University Press, 2005.

[Lun82] T. S. Lundgren. Strained spiral vortex model for turbulent fine structure. *Physics of Fluids*, 25(12):2193–2203, 1982.

[McD87] J. M. McDonough. *Lectures in Elementary Fluid Dynamics*. University of Kentucky, Lexington, 1987.

[Mil63] J. Milnor. *Morse Theory*. Princeton University Press, 1963.

[MLP+10] T. McLoughlin, R. S. Laramee, R. Peikert, F. H. Post, and M. Chen. Over Two Decades of Integration-Based, Geometric Flow Visualization. *Computer Graphics Forum*, 29(6):1807–1829, 2010.

[MPSS05] O. Mallo, R. Peikert, C. Sigg, and F. Sadlo. Illuminated lines revisited. In *Proceedings IEEE Visualization 2005*, pages 19–26, 2005.

[MSE+06] D. Merhof, M. Sonntag, F. Enders, C. Nimsky, P. Hastreiter, and G. Greiner. Hybrid visualization for white matter tracts using triangle strips and point sprites. *IEEE Transactions on Visualization and Computer Graphics*, 12:1181–1188, 2006.

[MT03] J. E. Marsden and A. J. Thromba. *Vector Calculus*. W. H. Freeman, 5 edition, 2003.

[NAM+03] B. R. Noack, K. Afanasiev, M. Morzyński, G. Tadmor, and F. Thiele. A hierarchy of low-dimensional models for the transient and post-transient cylinder wake. *Journal of Fluid Mechanics*, 497:335–363, 2003.

[Nes89] J. M. Nese. Quantifying local predictability in phase space. *Physica D*, 35:237–250, 1989.

[NMTB04] B. R. Noack, I. Mezić, G. Tadmor, and A. Banaszuk. Optimal mixing in recirculation zones. *Physics of Fluids*, 16(4):867–888, 2004.

[NPM05] B. R. Noack, P. Papas, and P. A. Monkewitz. The need for a pressure-term representation in empirical Galerkin models of incompressible shear flows. *Journal of Fluid Mechanics*, 523:339–365, 2005.

[NPT+04] B. R. Noack, I. Pelivan, G. Tadmor, M. Morzyński, and P. Comte. Robust low-dimensional Galerkin models of natural and actuated flows. In *Proceedings Fourth Aeroacoustics Workshop 2004*, 2004.

[NSA+08] B. R. Noack, M. Schlegel, B. Ahlborn, G. Mutschke, M. Morzyński, P. Comte, and G. Tadmor. A finite-time thermodynamics of unsteady fluid flows. *Journal of Non-Equilibrium Thermodynamics*, 33(2):103–148, 2008.

[Oku70] Akira Okubo. Horizontal dispersion of floatable particles in the vicinity of velocity singularities such as convergences. *Deep Sea Research and Oceanographic Abstracts*, 17(3):445 – 454, 1970.

[Pan05] R. L. Panton. *Incompressible Flow*. Wiley & Sons, 2005.

[PD10] T. Peacock and J. Dabiri. Introduction to focus issue: Lagrangian coherent structures. *Chaos*, 20(1):017501, 2010.

[PKPH09] C. Petz, J. Kasten, S. Prohaska, and H.-C. Hege. Hierarchical vortex regions in swirling flow. *Computer Graphics Forum*, 28(3):863 – 870, 2009.

[Pos03] F. H. Post. The state of the art in flow visualization: Feature extraction and tracking. *Computer Graphics Forum*, 22(4):775–792, 2003.

[PPF+10] A. Pobitzer, R. Peikert, R. Fuchs, B. Schindler, A. Kuhn, H. Theisel, K. Matkovic, and H. Hauser. On the way towards topology-based visualization of unsteady flow - the state of the art. In *Proceedings Eurographics 2010*, pages 137–154, 2010.

[PPF+11] A. Pobitzer, R. Peikert, R. Fuchs, H. Theisel, and H. Hauser. Filtering of FTLE for visualizing spatial separation in unsteady 3d flow. In *Topological Methods in Data Analysis and Visualization II*. Springer, 2011.

[PR00] R. Peikert and M. Roth. The parallel vectors operator - a vector field visualization primitive. In *Proceedings IEEE Visualization 2000*, pages 263–270, 2000.

[Rei12] J. Reininghaus. *Computational discrete Morse theory*. PhD thesis, Freie Universität Berlin, 2012.

[RGH+10] J. Reininghaus, D. Günther, I. Hotz, S. Prohaska, and H.-C. Hege. TADD: A computational framework for data analysis using discrete Morse theory. In *Proceedings International Congress on Mathematical Software 2010*, pages 198–208, 2010.

[RKLW90] V. Rom-Kedar, A. Leonard, and S. Wiggins. An analytical study of transport, mixing and chaos in an unsteady vortical flow. *Journal of Fluid Mechanics*, 214:347–394, 1990.

[RKWH12] J. Reininghaus, J. Kasten, T. Weinkauf, and I. Hotz. Efficient computation of combinatorial feature flow fields. *IEEE Transactions on Visualization and Computer Graphics – in press*, 99, 2012.

[RPP+09] O. Rosanwo, C. Petz, S. Prohaska, I. Hotz, and H.-C. Hege. Dual streamline seeding. In *Proceedings IEEE Pacific Visualization 2009*, pages 9–16, 2009.

[RPS99] F. Reinders, F. H. Post, and H. J. W. Spoelder. Attribute-based feature tracking. In *Proceedings Joint EG - IEEE TCVG Symposium on Visualization 1999*, pages 63–72, 1999.

[RSVP02] F. Reinders, I.A. Sadarjoen, B. Vrolijk, and F.H. Post. Vortex tracking and visualisation in a flow past a tapered cylinder. *Computer Graphics Forum*, 21(4):675–682, 2002.

[RWS11] V. Robins, P. Wood, and A. Sheppard. Theory and algorithms for constructing discrete Morse complexes from grayscale digital images. *IEEE Transactions on Pattern Analysis and Machine Intelligence*, 33(8):1646–1658, 2011.

[SB06] B.-S. Sohn and C. Bajaj. Time-varying contour topology. *IEEE Transactions on Visualization and Computer Graphics*, 12(1):14–25, 2006.

[SBV+11] T. Schafhitzel, K. Baysal, M. Vaaraniemi, U. Rist, and D. Weiskopf. Visualizing the evolution and interaction of vortices and shear layers in time-dependent 3D flow. *IEEE Transactions on Visualization and Computer Graphics*, 17(4):412–425, 2011.

[Sch79] H. Schlichting. *Boundary-Layer Theory*. McGraw Hill, 1979.

[Sch99] Gerik Scheuermann. *Topological vector field visualization with Clifford algebra*. PhD thesis, Universität Kaiserslautern, 1999.

[SGSM08] T. Salzbrunn, C. Garth, G. Scheuermann, and J. Meyer. Pathline predicates and unsteady flow structures. *The Visual Computer*, 24(12):1039–1051, 2008.

[SH95] D. Stalling and H.-C. Hege. Fast and resolution independent line integral convolution. In *Proceedings ACM SIGGRAPH 1995*, pages 249–256, 1995.

[Sha06] S. C. Shadden. *A Dynamical Systems Approach to Unsteady Systems*. PhD thesis, California Institute of Technology Pasadena, 2006.

[SHJK00] G. Scheuermann, B. Hamann, K. I. Joy, and W. Kollmann. Visualizing local vector field topology. *SPIE Journal of Electronic Imaging*, 9:367, 2000.

[SJWS08] T. Salzbrunn, H. Jänicke, T. Wischgoll, and G. Scheuermann. The state of the art in flow visualization: Partition-based techniques. In *Proceedings Simulation and Visualization 2008*, pages 75–92, 2008.

[SLM05] S.C. Shadden, F. Lekien, and J. E. Marsden. Definition and properties of Lagrangian coherent structures from finite-time Lyapunov exponents in two-dimensional aperiodic flows. *Physica D*, 212(3-4):271–304, 2005.

[Sma61] S. Smale. On gradient dynamical systems. *The Annals of Mathematics*, 74:199–206, 1961.

[Soi99] P. Soille. *Morphological image analysis*. Springer Verlag, 1999.

[SP99] I. A. Sadarjoen and F. H. Post. Geometric methods for vortex extraction. In *Proceedings Joint EG - IEEE TVCG Symposium on Visualization 1999*, pages 53–62, 1999.

[SP00] I. A. Sadarjoen and F. H. Post. Detection, quantification, and tracking of vortices using streamline geometry. *Computers and Graphics*, 24(3):333–341, 2000.

[SP07] F. Sadlo and R. Peikert. Efficient visualization of Lagrangian coherent structures by filtered AMR ridge extraction. *IEEE Transactions on Visualization and Computer Graphics*, 13(6):1456–1463, 2007.

[SRE05] S. Stegmaier, U. Rist, and T. Ertl. Opening the can of worms: An exploration tool for vortical flows. In *Proceedings IEEE Visualization 2005*, pages 463–470, 2005.

[SRP11] F. Sadlo, A. Rigazzi, and R. Peikert. Time-dependent visualization of Lagrangian coherent structures by grid advection. In *Topological Methods in Data Analysis and Visualization*, pages 151–165. Springer, 2011.

[SSZC94] R. Samtaney, D. Silver, N. Zabusky, and J. Cao. Visualizing features and tracking their evolution. *IEEE Computer*, 27(7):20–27, 1994.

[Stu67] J. T. Stuart. On finite amplitude oscillations in laminar mixing layers. *Journal of Fluid Mechanics*, 29:417–440, 1967.

[STW+08] K. Shi, H. Theisel, T. Weinkauf, H.-C. Hege, and H.-P. Seidel. Finite-time transport structures of flow fields. In *Proceedings IEEE Pacific Visualization 2008*, pages 63–70, 2008.

[SW97] D. Silver and X. Wang. Tracking and visualizing turbulent 3D features. *IEEE Transactions on Visualization and Computer Graphics*, 3(2):129–141, 1997.

[SW10] F. Sadlo and D. Weiskopf. Time-dependent 2d vector field topology: An approach inspired by Lagrangian coherent structures‘. *Computer Graphics Forum*, 29(1):88–100, 2010.

[SWC+08] D. Schneider, A. Wiebel, H. Carr, M. Hlawitschka, and G. Scheuermann. Interactive comparison of scalar fields based on largest contours with applications to flow visualization. *IEEE Transactions on Visualization and Computer Graphics*, 14(6):1475–1482, 2008.

[SWTH07] J. Sahner, T. Weinkauf, N. Teuber, and H.-C. Hege. Vortex and strain skeletons in eulerian and Lagrangian frames. *IEEE Transactions on Visualization and Computer Graphics*, 13(5):980–990, 2007.

[Tab02] P. Tabeling. Two-dimensional turbulence: a physicist approach. *Physics Reports*, 362(1):1 – 62, 2002.

[Tay38] G. I. Taylor. The spectrum of turbulence. *Proceedings of the Royal Society of London. Series A-Mathematical and Physical Sciences*, 164(919):476–490, 1938.

[TCM10] A. Tikhonova, C. D. Correa, and K.-L. Ma. An exploratory technique for coherent visualization of time-varying volume data. *Computer Graphics Forum*, 29(3):783–792, 2010.

[TP82] M. Tobak and D. Peake. Topology of three-dimensional separated flows. *Annual Review of Fluid Mechanics*, 14:61–85, 1982.

[Tri02] Xavier Tricoche. *Vector and tensor topology simplification, tracking, and visualization.* PhD thesis, Universität Kaiserslautern, 2002.

[TS03] H. Theisel and H.-P. Seidel. Feature flow fields. In *Proceedings Joint EG - IEEE TCVG Symposium on Visualization 2003*, pages 141–148, 2003.

[TSW+05] H. Theisel, J. Sahner, T. Weinkauf, H.-C. Hege, and H.-P. Seidel. Extraction of parallel vector surfaces in 3D time-dependent fields and application to vortex core line tracking. In *Proceedings IEEE Visualization 2005*, pages 631–638, 2005.

[TWHS05] H. Theisel, T. Weinkauf, H.-C. Hege, and H.-P. Seidel. Topological methods for 2D time-dependent vector fields based on stream lines and pathlines. *IEEE Transactions on Visualization and Computer Graphics*, 11(4):383–394, 2005.

[TWSH02] X. Tricoche, T. Wischgoll, G. Scheuermann, and H. Hagen. Topology tracking for the visualization of time-dependent two-dimensional flows. *Computer and Graphics*, 26:249–257, 2002.

[VKP00] V. Verma, D. Kao, and A. Pang. A flow-guided streamline seeding strategy. In *Proceedings IEEE Visualization 2000*, pages 163–170, 2000.

[WB98] C. Weigle and D. C. Banks. Extracting iso-valued features in 4-dimensional scalar fields. In *Proceedings IEEE Symposium on Volume Visualization 1998*, pages 103–110, 1998.

[WBD+11] G. H. Weber, P.-T. Bremer, M. S. Day, J. B. Bell, and V. Pascucci. Feature tracking using Reeb graphs. In *Topological Methods in Data Analysis and Visualization*, pages 241–253. Springer, 2011.

[Wei91] J. Weiss. The dynamics of enstrophy transfer in two-dimensional hydrodynamics. *Physica D: Nonlinear Phenomena*, 48:273–294, 1991.

[Wei08] T. Weinkauf. *Extraction of Topological Structures in 2D and 3D Vector Fields*. PhD thesis, University Magdeburg, 2008.

[WG09] T. Weinkauf and D. Günther. Separatrix persistence: Extraction of salient edges on surfaces using topological methods. *Computer Graphics Forum*, 28(5):1519–1528, 2009.

[Wil96] C. H. K. Williamson. Vortex dynamics in the cylinder wake. *Annual Review of Fluid Mechanics*, 28:477–539, 1996.

[WSTH07] T. Weinkauf, J. Sahner, H. Theisel, and H.-C. Hege. Cores of swirling particle motion in unsteady flows. *IEEE Transactions on Visualization and Computer Graphics*, 13(6):1759–1766, 2007.

[WT10] T. Weinkauf and H. Theisel. Streak lines as tangent curves of a derived vector field. *IEEE Transactions on Visualization and Computer Graphics*, 16(6):1225–1234, 2010.

[WTH12] T. Weinkauf, H. Theisel, and H.-C. Hege. Advected tangent curves: a general scheme for characteristic curves of flow fields. *Computer Graphics Forum*, 31(2):825–834, 2012.

[WTvGP10] T. Weinkauf, H. Theisel, A. van Gelder, and A. Pang. Stable feature flow fields. *IEEE Transactions on Visualization and Computer Graphics*, 17(6):770–780, 2010.

[YJS06] A. Yilmaz, O. Javed, and M. Shah. Object tracking: A survey. *ACM Computing Surveys*, 38(4):1–45, 2006.

[Yul81] A. J. Yule. Investigations of eddy coherence in jet flows. In *The Role of Coherent Structures in Modelling Turbulence and Mixing*, volume 136, pages 188–207, 1981.

[Zeb87] A. Zebib. Stability of viscous flow past a circular cylinder. *Journal of Engineering Mathematics*, 21:155–165, 1987.

[ZFN+95] H.-Q. Zhang, U. Fey, B. R. Noack, M. König, and H. Eckelmann. On the transition of the cylinder wake. *Physics of Fluids*, 7(4):779–795, 1995.

[ZSH96] M. Zöckler, D. Stalling, and H.-C. Hege. Interactive visualization of 3D-vector fields using illuminated stream lines. In *Proceedings IEEE Visualization 1996*, pages 107–113, 1996.

List of Figures

List of Tables

Index

Selbstständigkeitserklärung

Ich erkläre hiermit, dass ich die vorliegende Arbeit ohne unzulässige Hilfe Dritter und ohne Benutzung anderer als der angegebenen Hilfsmittel angefertigt habe; die aus fremden Quellen direkt oder indirekt übernommenen Gedanken sind als solche kenntlich gemacht.

Insbesondere habe ich nicht die Hilfe eines kommerziellen Promotionsberaters in Anspruch genommen. Dritte haben von mir weder unmittelbar noch mittelbar geldwerte Leistungen für Arbeiten erhalten, die im Zusammenhang mit dem Inhalt der vorgelegten Dissertation stehen.

Die Arbeit wurde bisher weder im Inland noch im Ausland in gleicher oder ähnlicher Form als Dissertation eingereicht und ist als Ganzes auch noch nicht veröffentlicht.

Jens Kasten